Small-scale statistics in turbulent Rayleigh-Bénard convection

Dissertation

zur Erlangung des akademischen Grades

**Doktoringenieur
(Dr.-Ing.)**

vorgelegt der

Fakultät für Maschinenbau der
Technischen Universität Ilmenau

von Herrn
M.Sc. Mohammad S. Emran
geboren am 01.01.1976 in Feni/Bangladesch

Acknowledgment

Zusammenfassung

Anhand direkter numerischer Simulationen (DNS) werden detaillierte Untersuchungen in turbulenter Rayleigh-Bénard Konvektion in einer zylindrischen Zelle mit isothermen oberen und unteren Platten und adiabatischen Seitenwänden durchgeführt. Die Schwerpunkte der Untersuchungen sind die Statistiken der Temperatur T, ihrer Fluktuationen θ, und ihrer Gradienten; die Statistik der thermischen Dissipationsrate ϵ_T und ihre Skalierung mit der Rayleigh-Zahl Ra; die Abhängigkeit des Wärmetransports vom Seitenverhältnis der Zelle Γ und damit zusammenhängende Änderungen in der großskaligen Zirkulation (GSZ) sowie die Lagrangesche Teilchendynamik in Konvektion. Die Simulationsparameter sind $Ra = 10^7 - 10^9$, $\Gamma = 0.5 - 12$ und die Prandtl-Zahl $Pr = 0.7$.

Die Wahrscheinlichkeitsdichtefunktionen (WDF) von T und θ weichen in allen Regionen der Zelle vom Gaußschen Fall ab. Anhand der Schiefe von $\partial_z\theta$ konnte die Rückkehr der kleinskaligen Turbulenz zur lokalen Isotropie mit zunehmender Ra im Innern der Zelle festgestellt werden. Ähnlich wie beim skalaren Mischen, weicht die WDF der thermischen Dissipationsrate der Temperaturfluktuationen, ϵ_θ, von der Log-Normalform ab. Die WDFs sind stets gestreckte exponentielle Verteitungen, deren Schweife mit wachsender Ra auf Grund zunehmender kleinskaliger Intermittenz weiter werden. Der Grad der Intermittenz ist stärker sowohl in der thermischen Grenzschicht (TGS) als auch im Volumen. Er ist stets stärker im Seitenwandbereich als im Innern der Zelle. Darüber hinaus liefert ϵ_θ nicht nur im Volumen den dominanten Beitrag zur Gesamtdissipation, sondern trägt auch in der TGS signifikant bei. Das Potenzgesetz $\langle\epsilon_T\rangle \sim Ra^\zeta$ ergibt immer einen negativen Exponenten ζ, sowohl im Volumen als auch in von Plumes beherrschten Gebieten und im turbulenten Hintergrund. Das steht im Gegensatz zur Skalentheorie des Wärmetransports, stimmt aber gut mit Experimenten überein.

Die Nusselt-Zahl, Nu, folgt dem Gesetz $Nu = A(\Gamma) \times Ra^{\beta(\Gamma)}$, mit einer Potenzgesetz-Abhängigkeit der Parameter A und β. Das Minimum der Kurve $Nu(\Gamma)$ liegt genau dort wo die GSZ einen Übergang von einer großen Rolle zu zwei hat. $Nu(\Gamma)$ variiert zwischen 3%–11% und wird geometrieunabhängig für $\Gamma \gtrsim 8$. Die Muster im vollen turbulenten Regime haben Ähnlichkeit mit Strukturen im schwach nichtlinearen Regime. Fünfeckige bzw. sechseckige im Rollen werden beobachtet, wenn $\Gamma \geq 8$.

Die Lagrangesche Teilchendispersion in Konvektion zeigt einen Übergang vom ballistischen Regime zum Richardson-Regime, jedoch kein Taylor-Regime auf Grund die Endlichkeit der Konvektionszelle. Die Existenz des Richardsonregimes hängt sensitiv vom Anfangsabstand der Teilchen im Paar ab, ähnlich wie in homogen isotroper Turbulenz. Unser Interpolationsschema gibt die Nusseltzahlen im Lagrangeschen Bezugssystem richtig wieder. Die Statisitik der Komponenten des Beschleunigungsvektors ist sehr intermittent ähnlich zu isotroper Turbulenz. Alle drei Verteilungen fallen im Gegensatz zur Konvektion in einer unendlich ausgedehnten Strömgungsschicht zusammen.

Abstract

We conduct detailed investigations in turbulent Rayleigh-Bénard convection in a cylindrical cell with isothermal top and bottom plates and adiabatic sidewalls by means of three-dimensional direct numerical simulation (DNS). Our analyses focused on the following areas: the statistics of the temperature T, its fluctuations θ, and gradients; the statistics of the thermal dissipation rate ϵ_T, and its scaling with the Rayleigh number Ra; the dependence of the heat transfer on the aspect ratio Γ, and the corresponding changes in the large-scale circulation (LSC) patterns; and the Lagrangian particle dispersion in convection. The simulation parameters are $Ra = 10^7 - 10^9$, $\Gamma = 0.5 - 12$ and the Prandtl number $Pr = 0.7$.

The probability density functions (PDFs) of T and θ are found to be always non-Gaussian in all regions of the convection cell. The skewness of $\partial_z \theta$ shows a return-to-isotropy trend in the bulk with increasing Ra. Similar to passive scalar mixing, the PDFs of the thermal dissipation rate due to the temperature fluctuations, ϵ_θ, deviate from the log-normality. The PDFs are stretched exponential shape and the tails are more extended with increasing Ra, due to increasing degree of small-scale intermittency. The degree of intermittency is much stronger in the thermal boundary layer (BL) than in the bulk, and stronger in the sidewall region than in the inner zone. Furthermore, ϵ_θ not only dominates in the bulk but also contributes significantly to ϵ_T in the BL. The scaling law $\langle \epsilon_T \rangle \sim Ra^\zeta$ always gives a negative exponent, ζ, in the bulk or plume and background dominated regions. This is in contrast to the scaling theories, but in agreement with measurements.

The Nusselt number, Nu, follows the scaling law $Nu = A(\Gamma) \times Ra^{\beta(\Gamma)}$, in which a power law dependence of the fit parameters A and β on Γ is detected. The minimum of $Nu(\Gamma)$ is found at $\Gamma \approx 2.5$ and $\Gamma \approx 2.25$ for $Ra = 10^7$ and $Ra = 10^8$, respectively. At this point, the LSC undergoes a transition from a single-roll to a double-roll pattern. $Nu(\Gamma)$ varies between 3%–11% and becomes independent of geometry for $\Gamma \gtrsim 8$. The LSC patterns in fully turbulent flow are strikingly similar to those in the weakly nonlinear regime. Patterns similar to pentagon or hexagon are observed preferentially in turbulent convection, if $\Gamma \geq 8$. The LSC is reorganised from roll to pentagonal or hexagonal shapes with increasing Ra and Γ.

The Lagrangian pair dispersion, $R^2(t)$, in turbulent convection undergoes a transition from the ballistic regime to the Richardson-like one. No Taylor regime is observed due to the finite size of the cell. Moreover, $R^2(t)$ is sensitive to the initial separation. Our interpolation scheme reproduces accurately Nu in the Lagrangian frame. The convergence of $Nu(t)$ is sensitive with respect to the number of particles and the kind of seeding (uniform or nonuniform). The acceleration components, a_i, are highly intermittent with symmetric and stretched exponential distributions and have non-Gaussian flatness ($F(a_i) \gg 3$). All three distributions collapse, in contrast to studies in a laterally unbounded fluid layer.

Contents

1 Introduction

1.1 Rayleigh-Bénard Convection

Rayleigh-Bénard Convection is a natural phenomenon that occurs due to the instability of a fluid layer confined between two horizontal plates with different temperatures. Let us consider a convection cell filled with a fluid of density ρ, viscosity μ and thermal conductivity κ. Initially, the fluid is at rest with no convection. The cell is heated from below and cooled from above. If the temperature difference ΔT between the hot and cold plates is strong enough, the hot plumes rise and cold plumes descend as shown in Figure 1.1, which triggers convective motion inside the cell. Natural convection occurs as the buoyancy force causes an unstable temperature gradient (Figures 1.2b,c). For different forcing and boundary conditions, patterns like parallel rolls, square or hexagons are identifiable (Koschmieder 1993). Bénard (1900) was the pioneer, who conducted systematic investigations of convection in a thin fluid layer heated from below and later, Rayleigh (1916) established the theoretical foundation of Bénard's work. For convection to take place, the buoyancy force due to gravity must overcome the viscous forces due to thermal and momentum diffusions.
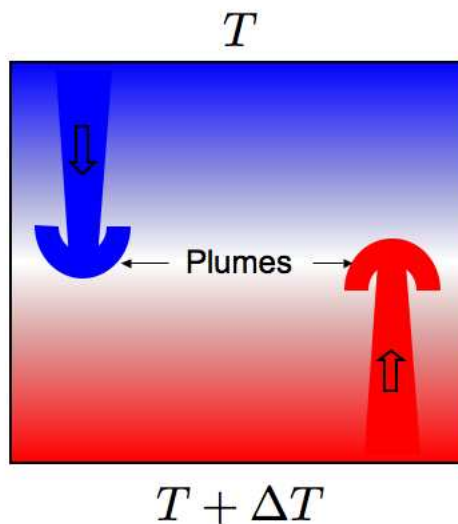
Figure 1.1: Sketch of the thermal convection process in a rectangular cell.
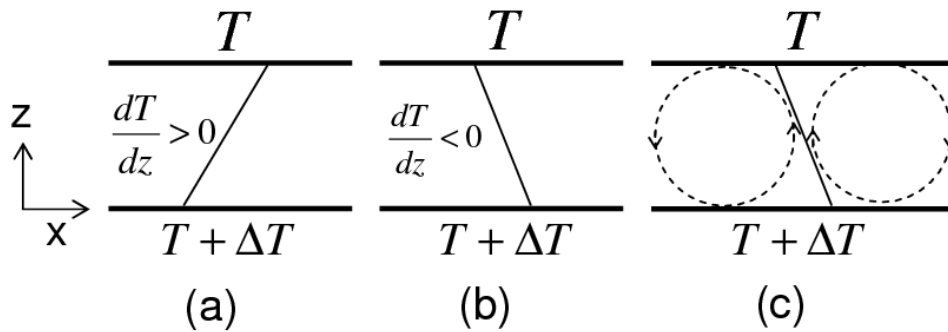
Figure 1.2: Fluid layer with: (a) stable temperature gradient ($\frac{dT}{dz} > 0$) and (b) unstable temperature gradient ($\frac{dT}{dz} < 0$). The unstable gradient in (b) leads to convection with roll pattern as shown in (c) .

The Rayleigh number Ra, which is a measure of the dimensionless temperature difference in the cell, is defined as

$$Ra = \frac{\alpha g \Delta T H^3}{\nu \kappa} \,. \tag{1.1}$$

The symbol α is the coefficient of volume expansion, g – the gravitational acceleration, H – the height of the convection cell and $\nu = \frac{\mu}{\rho}$ – the kinematic viscosity. Other control parameters involved in convection are the Prandtl number $Pr = \frac{\nu}{\kappa}$, which defines the characteristics of a given fluid, and the aspect ratio Γ, which is a measure of flatness or slenderness of a cell. Most of the investigations in Rayleigh-Bénard convection are aimed to establish a precise relation between the heat transfer and control parameters, such as

$$Nu = f(Ra, Pr, \Gamma) \,. \tag{1.2}$$

The Nusselt number Nu is the ratio of the convective to conductive heat transfer.

1.1.1 Boussinesq approximation

The convection process in a system can be described by the Boussinesq (1903) equations, which are the simplifications of the Navier-Stokes equations. In the Boussinesq approximation, the density variation due to the temperature difference is neglected everywhere except in the buoyancy term. For a small temperature difference, the density is a linear function of the temperature, which is given by

$$\rho = \rho_0 \left\{ 1 - \alpha \left(T - T_0 \right) \right\} \,, \tag{1.3}$$

where ρ_0 is the density of fluid at reference temperature T_0. The equations of motion follow the conservation of mass, momentum and energy, which can be written in

the form of

$$\frac{\partial \boldsymbol{U}}{\partial t} + (\boldsymbol{U} \cdot \boldsymbol{\nabla}) \boldsymbol{U} \;=\; -\boldsymbol{\nabla} P + \nu \boldsymbol{\nabla}^2 \boldsymbol{U} - \alpha g (T_0 - T) \boldsymbol{e}_z \,, \qquad (1.4)$$

$$\frac{\partial T}{\partial t} + (\boldsymbol{U} \cdot \boldsymbol{\nabla}) T \;=\; \kappa \boldsymbol{\nabla}^2 T \,, \qquad (1.5)$$

$$\boldsymbol{\nabla} \cdot \boldsymbol{U} \;=\; 0 \,. \qquad (1.6)$$

Here $\boldsymbol{U}(\boldsymbol{x}, t) = (u_x, u_y, u_z)^T$ is the velocity at position $\boldsymbol{x} = (x, y, z)^T$ and time t, $T(\boldsymbol{x}, t)$ – the total temperature and $P(\boldsymbol{x}, t) = \bar{p}/\rho_0 + \Phi$, with $\bar{p}$ being the isotropic pressure, Φ the gravitational potential and $\boldsymbol{e}_z$ the identity vector opposite to the direction of gravity.

Eqns. (1.4)–(1.6) are made dimensionless with respect to the free-fall velocity $U_f = \sqrt{\alpha g \Delta T H}$, the cell height H and the temperature difference $\Delta T = T_h - T_c$, with T_h and T_c being the temperatures at the hot and cold plates, respectively. Following Verzicco & Camussi (2003), the resulting dimensionless system is

$$\frac{\partial \boldsymbol{u}}{\partial t} + (\boldsymbol{u} \cdot \boldsymbol{\nabla}) \boldsymbol{u} \;=\; -\boldsymbol{\nabla} p + \sqrt{\frac{Pr}{Ra}} \boldsymbol{\nabla}^2 \boldsymbol{u} + \tilde{T} \boldsymbol{e}_z \,, \qquad (1.7)$$

$$\frac{\partial \tilde{T}}{\partial t} + (\boldsymbol{u} \cdot \boldsymbol{\nabla}) \tilde{T} \;=\; \frac{1}{\sqrt{RaPr}} \boldsymbol{\nabla}^2 \tilde{T} \,, \qquad (1.8)$$

$$\boldsymbol{\nabla} \cdot \boldsymbol{u} \;=\; 0 \,. \qquad (1.9)$$

The symbol $\mathbf{u}$ denotes the dimensionless velocity, p is the dimensionless pressure (separated from the hydrostatic contribution) and $\tilde{T} = (T - T_c)/\Delta T$ is the dimensionless temperature. $\tilde{T}$ has the value 1 at the hot plate and 0 at the cold plate.

Due to the imposed temperature gradient on the system, there is a net heat flux in the vertical direction. For adiabatic sidewalls, averaging Eqn. (1.5) in the horizontal plane results in a constant Nusselt number, which is independent of z. Following Shraiman & Siggia (1990) and Grossmann & Lohse (2000), we write the vertical heat flux as

$$Nu(z) = \frac{\langle u_z T \rangle_{A,t} - \kappa \partial_z \langle T \rangle_{A,t}}{\kappa \Delta T H^{-1}} = \text{const} \,. \qquad (1.10)$$

Here $\langle \cdot \rangle_{A,t}$ denotes an averaging over the horizontal plane and an ensemble of statistically independent snapshots.

1.1.2 Linear stability and onset of convection motion

Linear stability analysis is a very useful tool in understanding the pattern formation at the onset of convection. In linear stability analysis of the Rayleigh-Bénard system, a small perturbation around a uniform base flow results in a linear system of equations, whose solution is aimed at identifying the critical values of the control parameters for which the flow becomes unstable. Let us consider a horizontal fluid

layer with reference solutions $\boldsymbol{u}_0(z)$ and $\tilde{T}_0(z)$. The solutions of the system in terms of the base flow and perturbations are

$$\boldsymbol{u}(\boldsymbol{x},t) = \boldsymbol{u}_0(z) + \boldsymbol{u}'(\boldsymbol{x},t)\,, \tag{1.11}$$
$$\tilde{T}(\boldsymbol{x},t) = \tilde{T}_0(z) + \theta(\boldsymbol{x},t)\,, \tag{1.12}$$

where $\boldsymbol{u}'$ and θ are the fluctuations from the base state in the velocity and temperature fields, respectively. With the help of incompressibility of fluid, it is possible to eliminate the pressure, temperature and horizontal components of the velocity from Eqns. (1.7)–(1.9) (see Drazin 2002 for details). The resulting ordinary differential equation (ODE) system depends only on u'_z, which is solved with the so-called normal mode ansatz for infinitesimal disturbances as

$$u'_z(\boldsymbol{x},t) = u_{z,0}(z)\,e^{i(k_x x + k_y y)}\,e^{st}\,, \tag{1.13}$$
$$\theta(\boldsymbol{x},t) = \tilde{T}_0(z)\,e^{i(k_x x + k_y y)}\,e^{st}\,. \tag{1.14}$$

The term e^{st} represents the temporal growth rate of perturbations for the complex amplitude s, and k_x and k_y are the horizontal wave numbers, with $q^2 = k_x^2 + k_y^2$.
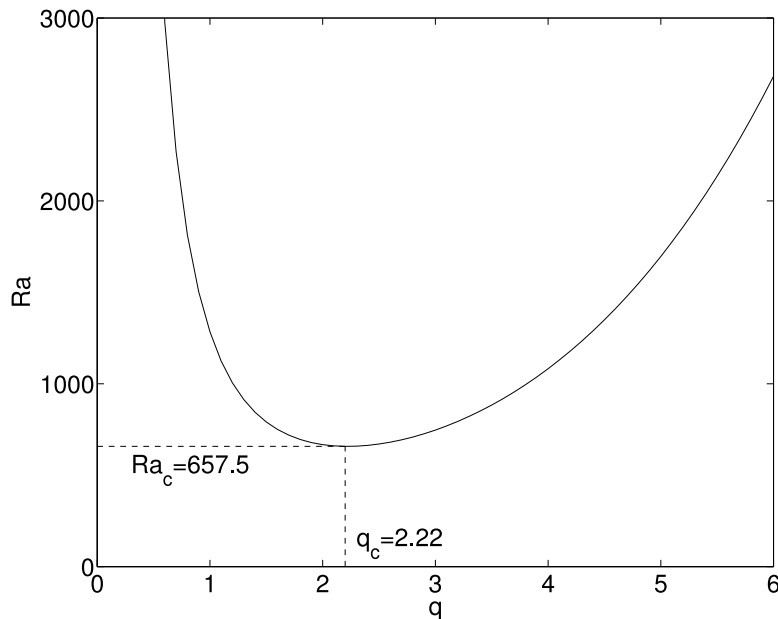
Figure 1.3: Neutral stability curve in the $Ra - q$ plane for Rayleigh-Bénard convection in a laterally unbounded fluid layer with free-slip top and bottom boundaries.

The stability conditions are

$$\mathrm{Re}(s) \leq 0 \Rightarrow \text{stable}\,, \tag{1.15}$$
$$\mathrm{Re}(s) > 0 \Rightarrow \text{unstable}\,. \tag{1.16}$$

For the free-slip boundaries ($\theta = u'_z = \frac{\partial^2 u'_z}{\partial z^2} = 0$ at $z = 0, 1$), the eigenvalues corresponding to the marginal stability, $\text{Re}(s) = 0$, are

$$Ra(q, n) = \frac{(n^2 \pi^2 + q^2)^3}{q^2} \,, \tag{1.17}$$

and the smallest eigenvalue ($n = 1$) is

$$Ra(q) = \frac{(\pi^2 + q^2)^3}{q^2} \,. \tag{1.18}$$

Minimizing $Ra(q)$ with respect to the horizontal wave number q gives the critical Rayleigh number $Ra_c = 27\pi^4/4 = 657.5$, with the corresponding critical wave number $q_c = \pi/\sqrt{2}$ (Figure 1.3). For rigid boundaries, the critical values are $Ra_c = 1708$ and $q_c = 3.11$.
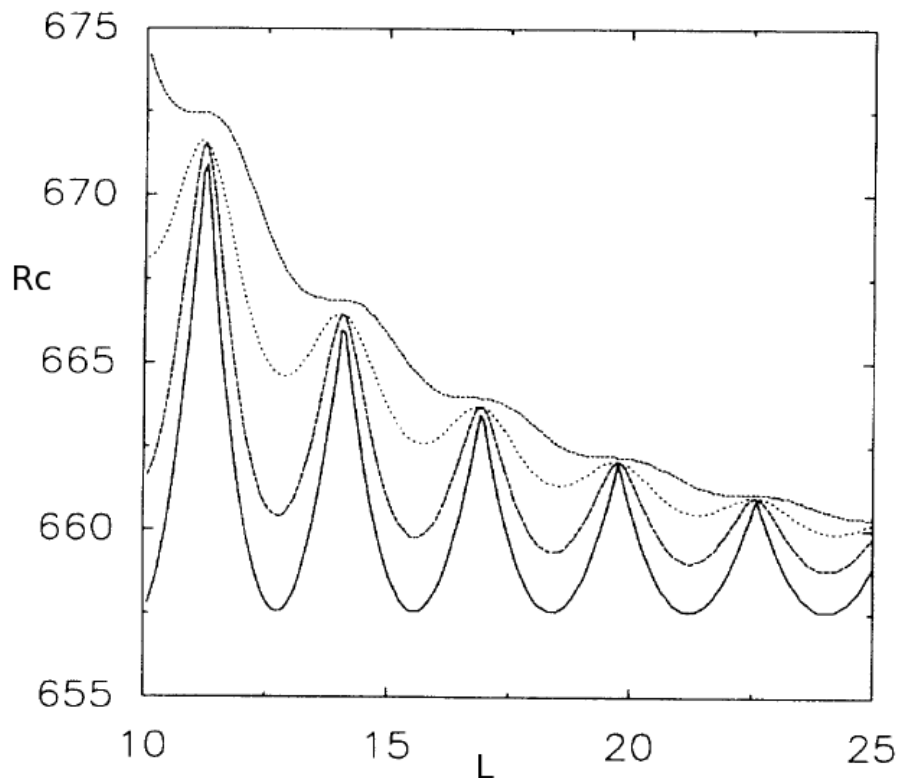
Figure 1.4: Critical Rayleigh number as a function of the dimensionless cell size L in a 2D free-slip box. For a non-negative constant $\alpha = r k_w \tau \pi^2$, with k_w – thermal diffusivity of the side wall, τ – sidewall thickness ($\tau \ll 1$), the sidewall parameters are (from bottom to top curves) $\alpha = 0$, 0.2, 1 and 100, respectively. Here $\alpha = 0$ corresponds to the free-slip case and $\alpha = \infty$ for the no-slip case. (Taken from Chen 1992).

The sidewalls act as obstacles in the flow field through viscous effects and change the threshold value of the marginal stability parameter Ra_c as given in Figure 1.4 (Chen 1992). In this figure, the sidewall boundary conditions vary with respect to a non-negative constant $\alpha = rk_w\tau\pi^2$, with r is the ratio of the volume specific heat capacity of the sidewall and the fluid layer, k_w – the dimensionless thermal diffusivity of the sidewall, τ – the sidewall thickness ($\tau \ll 1$). The sidewall parameters are (from bottom to top curves) $\alpha = 0$, 0.2, 1 and 100, respectively, with $\alpha = 0$ corresponds to the free-slip case and $\alpha = \infty$ for the no-slip case. In case of no-slip boundaries (top curve), the critical Rayleigh number Ra_c at the onset of convection is higher for a slender cell than that of a flat cell.
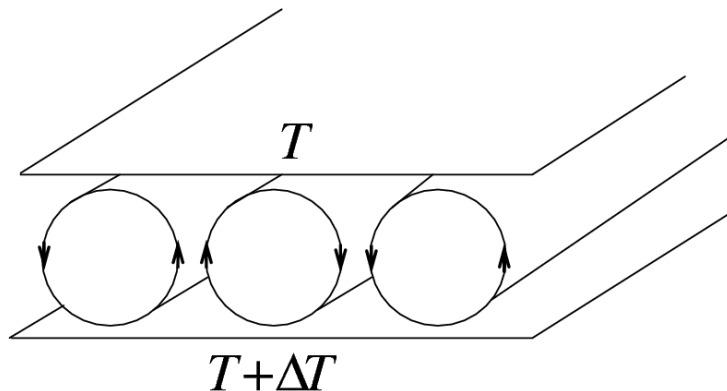
Figure 1.5: Two-dimensional parallel rolls in a rectangular domain.

Now let us consider the function

$$f = e^{i(k_x x + k_y y)}\,. \tag{1.19}$$

Taking the gradients of f twice in the $x - y$ plane gives

$$\Delta f + q^2 f = 0\,, \tag{1.20}$$

which is the 2D-wave equation, whose solution results in infinite numbers of wave vectors $\boldsymbol{k} = (k_x, k_y)^T$ in the horizontal plane of a laterally unbounded domain. The simplest solution is in the form of parallel rolls, for example, in a rectangular domain as shown in Figure 1.5. In the sub-critical regime ($Ra < Ra_c$), no pattern exist, however, in the super-critical (moderately non-linear) zone ($Ra > Ra_c$), bifurcation causes the formation of stable patterns in the vicinity of the onset of convection (Schlüter *et al.* 1965). Examples of such steady patterns are rolls which are made of a single pair of wave vectors $\pm k\hat{\boldsymbol{x}}$ with $\hat{\boldsymbol{x}}$ the unit vector in the horizontal plane oriented opposite to each other, squares which consist of two pairs of wave vectors at right angles and hexagons which are formed due to the superposition of three pairs oriented at 120° (Chandrasekhar 1961). Figure 1.6 shows a two

dimensional envelope, which is a section of the so-called Busse balloon (Busse 1978) at constant Prandtl number. Two-dimensional stable patterns exist within this envelope and beyond that perturbations of three-dimensional waves on the weakly-nonlinear patterns cause various instabilities, e.g. cross-rolls, zig-zag instability and the Eckhaus instability, which are also called the secondary instabilities.
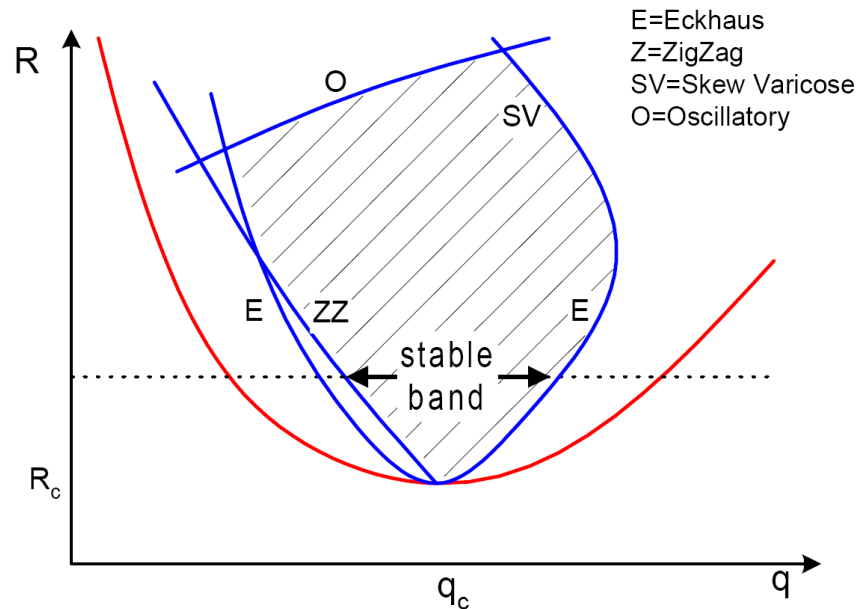
Figure 1.6: Section of the Busse balloon at constant Prandtl number. (Taken from Cross 2003).

1.1.3 Transition to turbulence

The transition to turbulence state is reached after a series of bifurcations in the form the primary, secondary, tertiary and time-dependent instabilities as described in Figure 1.7 in the $Ra-Pr$ parameter space by Krishnamurti (1970). The turbulent state is characterized by complex three-dimensional time-dependent random chaotic motions with a wide range of temporal and spatial scales. According to Castaing *et al.* (1989), convective turbulence is classified into *soft turbulence* ($2 \times 10^5 < Ra < 4 \times 10^7$) and *hard turbulence* ($4 \times 10^7 < Ra < 6 \times 10^{12}$) regimes. Their rationalization is based on the fact that the probability distribution of the temperature exhibits Gaussian shape in the soft regime and exponential shape in the hard regime. There may exist an *ultimate regime* ($Ra > 10^{16}$) according to Kraichnan (1962), in which the boundary layers become unstable and most of the temperature drop is localized within the thermal boundary layers. As a result of this instability, the heat transfer is significantly enhanced with a corresponding scaling $Nu \sim Ra^{1/2}$, which is much
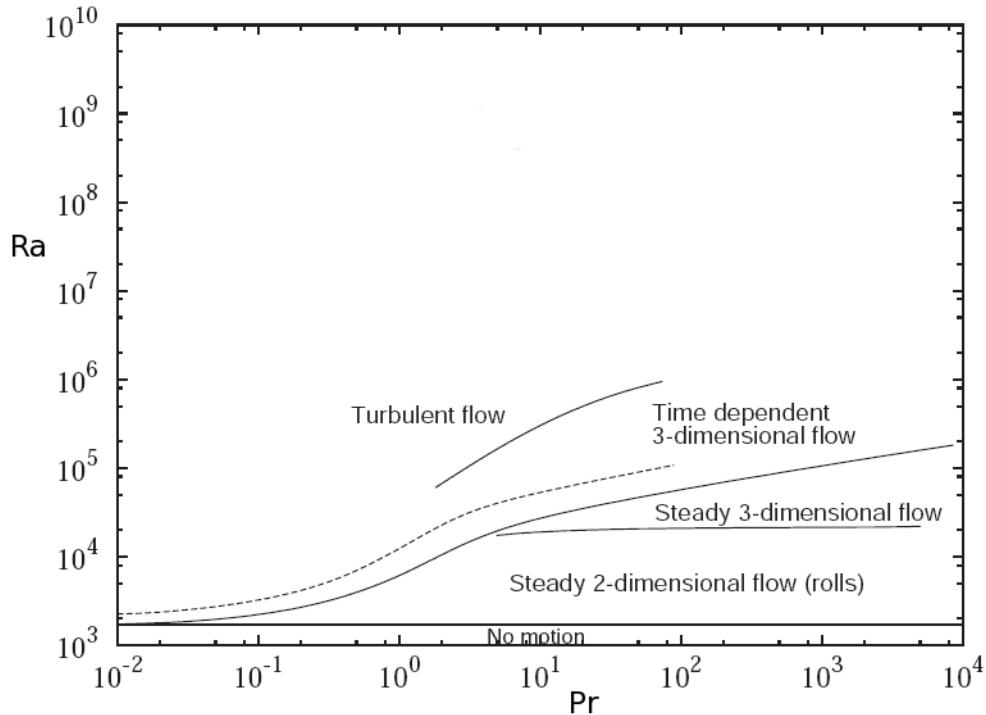
Figure 1.7: Transition to turbulence in the $Ra - Pr$ plane as described by Krishnamurti (1970).

higher compared to that in the hard turbulence regime ($Nu \sim Ra^{2/7-1/3}$).

1.2 Motivation for the present work

Study of Rayleigh-Bénard convection has gained tremendous importance as convection phenomena occur in many physical and industrial processes such as in geophysics, astro-physics, indoor ventilation, industrial heating and cooling (Kadanoff 2001). Following the pioneering works of Bénard (1900) and Rayleigh (1916), numerous theoretical (Malkus & Veronis 1958; Kraichnan 1962; Schlüter *et al.* 1965; Busse & Whitehead 1971; Grossmann & Lohse 2000), experimental (Krishnamurti & Howard 1981; Castaing *et al.* 1989; Niemela *et al.* 2000; Brown & Ahlers 2006; He *et al.* 2007) and numerical (Kerr 1996; Verzicco & Camussi 2003; Schumacher *et al.* 2005; Hartlep *et al.* 2005; Shishkina & Wagner 2006) studies have been conducted in the past. The main focus of thermal convection studies has been on the precise quantification of the global turbulent heat transport through the cell, which is measured by the dimensionless parameter, the Nusselt number Nu, as a function of the applied outer temperature difference, the properties of the working fluid and the geometry (Niemela & Sreenivasan 2003; Funfschilling *et al.* 2005). Three dimensionless control parameters – the Rayleigh number Ra, the Prandtl

number Pr and the aspect ratio Γ– represent the temperature difference in the cell, fluid properties and the geometry, respectively.

Experimental studies have been able to explore a large range of Rayleigh numbers in the so-called hard turbulence regime from $Ra \sim 10^7$ up to $Ra \sim 10^{17}$ in the case of liquid helium (Niemela *et al.* 2000). However, most experiments can provide pointwise measurements of time series of the turbulent fields only (du Puits *et al.* 2007). Only recently, two-dimensional cuts through the flow field have been analyzed by combining particle image velocimetry and shadowgraph techniques (Xi *et al.* 2004).

In contrast, direct numerical simulations (DNS) could not be conducted for flow configurations with very high Rayleigh numbers and large aspect ratios due to the limitation of current computer capacity. So far Amati *et al.* (2005) have reached $Ra \sim 10^{14}$ in a cell with aspect ratio $\Gamma = 0.5$. The advantage of DNS over the experiment is, however, a fully resolved spatial and temporal information in turbulent fields and local mechanisms of heat transfer (Kerr 1996; Verzicco & Camussi 2003; Hartlep *et al.* 2005; Shishkina & Wagner 2006, 2007).

1.2.1 Temperature and thermal dissipation rate

Closely related parameter to the Nusselt number is the mean of the thermal dissipation rate, which can be written as (see Grossmann & Lohse 2000)

$$\langle \epsilon_T \rangle_V = \frac{Nu}{\sqrt{RaPr}} \, . \tag{1.21}$$

The symbol $\langle . \rangle_V$ represents an averaging over the volume and an ensemble of statistically independent snapshots. The thermal dissipation rate field itself measures the magnitude of the temperature gradient and is defined as

$$\epsilon_T(\boldsymbol{x}, t) = \kappa \left(\frac{\partial T}{\partial x_i} \right)^2 \, . \tag{1.22}$$

Here $x_i = x, y, z$. Both equations, Eqns. (1.21) and (1.22), imply that the statistics of the fluctuating thermal dissipation field is connected with the local heat flux, $\boldsymbol{j}(\boldsymbol{x}, t) = -\kappa \boldsymbol{\nabla} T$. The measurement of the thermal dissipation field – and thus of the spatial derivatives of the temperature field – is experimentally challenging, especially in high-Rayleigh-number turbulence. Experiments can usually provide well-resolved time derivative (Belmonte & Libchaber 1996) or temporal increments of the temperature field (Zhou & Xia 2002). In case of temporal increments in convection, closed forms of the corresponding probability density functions (PDF) of stretched exponential type have been constructed successfully by Ching (1991, 1993). For other flows, such as axisymmetry jets, turbulent channel flows or homogeneous isotropic turbulence, PDFs of the velocity increments have been constructed

as a superposition of Gaussian distributions (Castaing, Gagne & Hopfinger 1990) or a product of a Gaussian random variable and a scale-dependent random multiplier (Chevillard *et al.* 2006). In Rayleigh-Bénard convection, time derivatives, however, cannot be translated into spatial derivatives by a Taylor frozen-flow hypothesis as in pipe or channel flows. Furthermore, for turbulence in a closed vessel, the concept of homogeneity is limited to the cell center only. Recently, He *et al.* (2007) were able to measure four temperature signals close to each other simultaneously to reconstruct temperature gradients. Their analysis disentangled contributions to the total thermal dissipation coming from the bulk and boundary layers. Rayleigh numbers $Ra \sim 10^9$ were attained in their experiments, but the resolution of the gradients remained limited to scales larger or equal to the thermal boundary layer thickness. Direct numerical simulations by Kerr (1996) and more recently by Shishkina & Wagner (2007) focused on the geometric properties of thermal plumes, the structures that carry the heat away from the bottom plate.

A detailed statistical analysis of the spatial derivatives of the temperature and the thermal dissipation field in different regions of the convection cell is thus incomplete. Very recent investigations by Emran & Schumacher (2008), He & Tong (2009) and Kaczorowski & Wagner (2009) shed more light in this regard. Moreover, knowledge about the strength of fluctuations around the mean temperature gradient and their dependence on the Rayleigh number allows for a validation of predictions by scaling theories, e.g. those by Grossmann & Lohse (2000). Such analysis is also interesting from the perspective of passive scalar mixing in turbulence where progress in understanding the mechanisms that cause intermittent fluctuations has been made recently (Shraiman & Siggia 2000). A first and open point is to understand the differences between passive and active scalars such as the temperature in convective turbulence. For the passive scalar case, it is known that larger amplitudes of the dissipation fields are mostly concentrated on fine scales (Kushnir *et al.* 2006) and that their statistical study puts rather large resolution constraints on DNS (Schumacher *et al.* 2005; Schumacher & Sreenivasan 2005; Donzis *et al.* 2008).

Therefore, we provide a detailed height-dependent statistical analysis of the temperature, its fluctuations and spatial derivatives. Due to constraints on the DNS grid resolution, our study is limited to a moderate Rayleigh number range, $Ra = 10^7 - 10^9$, for the cell with aspect ratio $\Gamma = 1$. Odd-order moments of spatial derivatives along an imposed outer mean scalar gradient have been used successfully to quantify deviations from local isotropy in shear flows or for the mixing of scalars in turbulence (Warhaft 2002; Pumir 1996; Schumacher & Sreenivasan 2003). We adopt these ideas for the present active scalar case and discuss the dependence of these anisotropy measures on Ra in different regions of the convection cell. Furthermore, we study the statistics of the thermal dissipation rate in the bulk and close to the bottom and top plates of the convection cell. The results are then related to findings from the passive scalar dissipation field. Our study is intended to build a bridge between the mixing of passive and active scalar fields by comparing the statistical properties for both cases. Motivated by the concept of Grossmann &

Lohse (2004), we also propose new definitions of the plume and background domi-
nated thermal dissipation rate fractions, which are conditioned with respect to the
quantity $u_z\theta$, which is always positive for the rising or falling plumes in a convec-
tion cell. We provide detailed scaling relations of the thermal dissipation rate with
respect to the Rayleigh number, based on our new definitions as well as the bulk
and boundary layer contributions and make a comparative study. Our aim is to
understand the discrepancies between the theories (e.g. Grossmann & Lohse 2000,
2004) and experiments (e.g. He *et al.* 2007; He & Tong 2009).

1.2.2 Geometry dependence of the heat transfer and large-scale circulation

Until now, the variation of turbulent heat transfer with respect to two of the three
dimensionless control parameters in thermal convection, namely the Rayleigh num-
ber Ra and the Prandtl number Pr, was the focus of most of the laboratory experi-
ments and simulations. The dependence on the third control parameter, the aspect
ratio Γ, has been studied much less extensively. Only a few systematic analyses
of high-Rayleigh-number convection in flat cells with $\Gamma > 1$ have been reported
(Wu & Libchaber 1992; Funfschilling *et al.* 2005; Hartlep *et al.* 2005; Sun *et al.*
2005; Niemela & Sreenivasan 2006; du Puits *et al.* 2007), although large-aspect
ratio systems are relevant for nearly all geophysical and astrophysical flows (Stein
& Nordlund 2006) and many engineering applications such as an energy-efficient
design of indoor ventilation systems (Zerihun Desta *et al.* 2005). Furthermore, an
explicit dependence on the aspect ratio is missing in any of the existing scaling
theories for the turbulent heat transfer (Siggia 1994; Grossmann & Lohse 2000).
Grossmann & Lohse (2003) refined their original ansatz by including variations of
the kinetic boundary layer thickness at the plates and sidewalls as a function of the
aspect ratio, however, they found that the global heat transfer laws were indepen-
dent of Γ. This can be attributed to the fact that their argumentation is built on
the volume flux conservation, which requires a large scale flow – a so-called "wind
of turbulence". In fact all existing scaling theories require such a large-scale flow
for the ansatz of their boundary layer dynamics. It is well-known that the coherent
large-scale circulations present at $\Gamma \sim 1$ break down into more complex and less co-
herent patterns when the aspect ratio is increased far beyond unity ($\Gamma \gg 1$). Such
phenomena were reported by several authors: for example by means of Fourier spec-
trum analysis by Hartlep *et al.* (2003), plume structure visualizations by Shishkina
& Wagner (2006) or comparisons of the autocorrelations of the temperature and
velocity fields by du Puits *et al.* (2007).

In this work, we, therefore, want to study the dependence of convective turbulence
on the aspect ratio in a cylindrical cell by three-dimensional direct numerical sim-
ulations. Our focus is on aspect ratios larger than unity. Values for Γ cover a
range between 0.5 and 12 for Rayleigh numbers between 10^7 and 10^9 and for a con-

stant Prandtl number $Pr = 0.7$. We try to address and augment the following two questions that have been partly discussed in other works: How does the turbulent heat transfer at fixed Rayleigh and Prandtl numbers vary the aspect ratio? Which changes in the global flow structure are associated with an increase of the aspect ratio beyond unity?

1.2.3 Lagrangian particle dispersion

Finally, we want to explore and complement some of the previous studies on the Lagrangian particle dispersion in turbulent convection. Most of the experimental and numerical investigations in turbulence have been conducted in the Eulerian frame of reference. Although Eulerian and Lagrangian studies are complementary, true temporal structures are revealed when the measurement of turbulent fluctuations is conducted along the particle trajectories (Voth *et al.* 2002). DNS studies on the Lagrangian turbulence have been conducted in the past, for example, by Yeung & Pope (1989) and most recently for the thermal convection in a Cartesian slab by Schumacher (2008, 2009). With the advancement in sophisticated apparatus, e.g. high resolution digital cameras, experiments on particles tracking in turbulence have drawn significant attention in recent decades (La Porta *et al.* 2001; Mordant *et al.* 2002; Gasteuil *et al.* 2007; Lobutova *et al.* 2009). Those studies were focused on the statistics of velocity or acceleration, measurements of local heat flux, identification of plumes and the geometrical characteristics of the particles (Braun *et al.*). Nevertheless, particle tracking experiments in the laboratory have some limitations, e.g. the size of the tracer particles and the size of the domain observable by the digital cameras. DNS on Lagrangian particle tracking has no such limitations, however, the challenging part here is to achieve high Rayleigh number Ra, which is restricted by the DNS grid resolution criteria. In the Lagrangian frame, we study the heat transfer, particle dispersion properties for the pair separation, statistics of the acceleration and the convective heat flux as well as the velocity and temperature increments for the data set $\Gamma = 1$ and 3 for $Ra = 10^7$, and $\Gamma = 1$ for $Ra = 10^8$.

1.3 Outline of the work

This thesis contains seven chapters. In *Chapter 1*, we give a brief introduction to Rayleigh-Bénard convection, the Boussinesq approximation to the equations of motion as well as a short discussion on the linear stability of the Rayleigh-Bénard system.

Chapter 2 deals with the numerical models, DNS grid resolution criteria, discretization schemes and the aspect-ratio-constraints on the DNS grid size as well as grid convergence studies.

In *Chapter 3*, we report the statistics of the total temperature field as well as its fluctuations and gradients. The analysis includes the height dependence of the temperature, its vertical derivatives, skewness and flatness. We also compare our findings with those of the passive scalar case. The studies are conducted in the cell with aspect ratio $\Gamma = 1$ for a moderate Rayleigh number range, $Ra = 10^7 - 10^9$, keeping the Prandtl number constant ($Pr = 0.7$).

Chapter 4 presents detailed analysis of the thermal dissipation field in different sub-volumes of the convection cell. We give an overview of the existing scaling theories on the thermal dissipation rate with respect to the Rayleigh number. Motivated by the theories of Grossmann & Lohse (2000, 2004), we provide new definitions of the plume and background dominated thermal dissipation rate fractions. We relate our findings to those of the existing scaling theories and experiments as well. The same data sets as in the previous chapter are taken here.

The dependence of the aspect ratio Γ on the heat transfer Nu is reported in *Chapter 5*. The variations in the heat transfer due to changes in the large-scale circulation (LSC) patterns in convection are elaborated with the flow field visualization. Comparisons are made with those in the weakly nonlinear regime above the onset of convection. The analysis includes a wide range of aspect ratio $\Gamma = 0.5 - 12$ for $Ra = 10^7 - 10^9$ and a fixed $Pr = 0.7$.

The studies on the Lagrangian tracer particle dispersion in Rayleigh-Bénard convection are provided in *Chapter 6*. A brief description of the interpolation scheme is given there. Due to the staggered grid arrangement, we adopt linear interpolation for the velocity field, which simplifies the computation. The time marching is done by the analytical integration of ordinary differential equations (ODEs) in the Lagrangian frame. The investigations are carried out for the pair dispersion properties and the heat transfer in the Lagrangian frame of reference as well as the statistics of the acceleration, the convective heat transfer and the velocity and temperature increments. The relevant parameters are: $\Gamma = 1$ and 3 for $Ra = 10^7$, and $\Gamma = 1$ for $Ra = 10^8$.

Finally, the concluding remarks are made in *Chapter 7*.

2 Numerical Scheme

The convective terms in the Navier-Stokes equations encompass the nonlinear dynamics of fluid flow. Complex flow phenomena such as instabilities, bifurcations and turbulence are the manifestation of the nonlinear dynamics. Due to this inherent nonlinearity, the existence of analytical solutions of the Navier-Stokes in complex flow configurations is not known except for a few simple laminar cases like the Couette flow, the Poiseuille flow and the Blasius boundary layer flow. Alternative approaches are sought to solve the system, e.g. to simplify the equations with the help of some statistical filtering processes like the Reynolds averaging and employ some adhoc basis modeling techniques such as RANS, LES or to conduct direct numerical simulation, in which no simplification is required and all scales of the flow are resolved numerically.

Time and computer capacity constraints do not allow for a broad use of DNS in large-scale industrial applications. Therefore, Reynolds-averaged Navier-Stokes (RANS) modeling and large eddy simulation (LES) are common in such complex external and internal flows, e.g. for aircraft wings and combustion chambers. Nevertheless, DNS has become an essential tool in conducting basic research in physics in recent decades. Because of its accuracy, DNS can be regarded as a direct competition to the experiments. Laboratory experiments are expensive and cannot provide, for example, the whole spectrum of spatial data in a domain. In contrast, DNS provides fully resolved spatial and temporal information in a turbulent field. The DNS database is extensively used in validation of the RANS and LES based engineering models.

2.1 Direct Numerical Simulation

Turbulent flow is characterized by complex three dimensional random motions with a wide range of temporal and spatial scales. Classical Richardson cascade hypothesis tells us that turbulent motions are composed of eddies of different sizes, small and large. The largest eddy could be of the size of the characteristic length L of the flow and the smallest ones are of the size of a dissipative scale, the Kolmogorov length η_K. In most cases, large eddies are fed energy by the mean flow. Since they are unstable, they break down into smaller and smaller eddies in a cascade process until disappear completely at the dissipation scale, at which the kinetic energy is

converted to internal energy due to the finite viscosity of the fluid. Small scale turbulence is assumed to be isotropic and universal and, therefore, independent of flow types.

In DNS approach, resolving turbulent features such as three-dimensionality and time-dependence of flow is very challenging. DNS is the most accurate method available today. Its accuracy is bounded by the particular numerical scheme, e.g. spectral methods, finite difference schemes. In order to capture all of the significant turbulent structures, the computational domain should be at least as large as the size of the largest eddy, L. For homogeneous isotropic turbulence with an uniform grid spacing, the DNS computational complexity is $L/\eta_K \sim Re_L^{3/4}$ (Ferziger & Perić 2001), with Re_L the Reynolds number based on L. In case of a three-dimensional domain, this complexity grows to $N \sim Re_L^{9/4}$ – where N is the number of grid points, which is extremely high in terms of cost and time, since typical Reynolds numbers in turbulent flows of practical importance could reach up to $Re \sim 10^9$ (Oh & Kang 1992). Latest advancements in supercomputing allow to achieve DNS simulations for a grid size of $N \sim 10^{10-11}$ (Kaneda *et al.* 2003; Schumacher *et al.* 2005; Yeung *et al.* 2005; Donzis *et al.* 2008). So far the highest Rayleigh number in DNS studies of Rayleigh-Bénard convection is $Ra \sim 10^{14}$ as reported by Amati *et al.* (2005) for a cylindrical cell with aspect ratio $\Gamma = 0.5$. In our present study, we could reach aspect ratio $\Gamma = 3$ for a simulation with $Ra = 10^9$.

2.2 Discretization methods

The non-dimensional Boussinesq equations, Eqns. (1.7)–(1.9), are rewritten in the cylindrical coordinate system. Boundary conditions are the no-slip condition for the velocity at all boundaries, isothermal top and bottom plates with adiabatic sidewalls for the temperature (Figure 2.1).

We employ the DNS scheme by Verzicco & Orlandi (1996) and their code. The equations are solved on a staggered grid, where the velocities are stored at the center of the surfaces, and the temperature and pressure are stored at the center of the cell as described in Figure 2.2. The staggered grid is used in order to avoid odd-even decoupling between the pressure and velocity that occurs on a collocated grid in finite-difference discretization (Harlow & Welch 1965). The Odd-even decoupling error leads to so-called checker-board patterns in the solutions.

The grid spacings are non-uniform in the axial and radial directions. In the axial direction, they correspond to the Tschebycheff collocation points, which ensure a dense clustering in the thermal boundary layers close to the hot and clod plates. The spatial discretization is performed by the second-order central difference scheme. A fractional-step method combined with a third-order Runge-Kutta for the advection terms and the Crank-Nicolson scheme for the viscous terms are employed for the
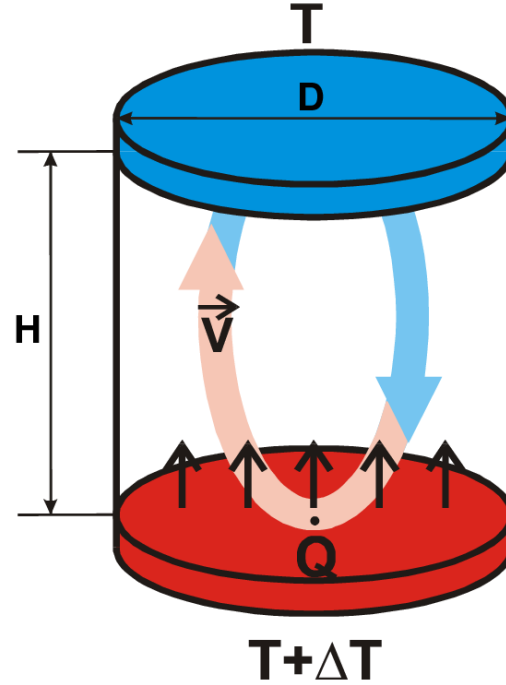
Figure 2.1: Rayleigh-Bénard cell with height H and diameter D. Boundary conditions are: no-slip condition for the velocity at all boundaries, isothermal top and bottom plates, and adiabatic sidewalls for the temperature.

temporal discretization. The time advancement scheme can be written as (see Kim & Moin 1985; Verzicco & Orlandi 1996 for details)

$$
\begin{aligned}
\frac{\hat{u}_i - u_i^n}{\Delta t} &= \gamma_n H_i^n + \rho_n H_i^{n-1} - \alpha_n G_i p^n \\
&\quad + \frac{\alpha_n}{2}(A_{i\phi} + A_{ir} + A_{iz})(\hat{u}_i + u_i^n)\,,
\end{aligned}
\tag{2.1}
$$

$$
\frac{u_i^{n+1} - \hat{u}_i}{\Delta t} = -\alpha_n G_i \Phi^{n+1}\,,
\tag{2.2}
$$

with the incompressibility condition

$$
D_i(u_i^{n+1}) = 0\,,
\tag{2.3}
$$

is enforced for each cell. The symbol $\hat{u}_i$ represents the intermediate velocity field, which is globally divergence free but not locally ; H_i – the convective terms; D_i – the discrete divergence operator; G_i – the discrete gradient operator; $A_{i\phi}, A_{ir}$ and A_{iz} are the discrete difference operators for the viscous terms in the azimuthal, radial and axial directions, respectively. The values of the coefficients α_n, γ_n and ρ_n depend on a particular time advancement scheme, e.g. Runge-Kutta, Adam-Bashforth. The tridiagonal system which arises from a factorization of Eqn. (2.1) is solved (Beam & Warming 1976). This results in a significant reduction of the
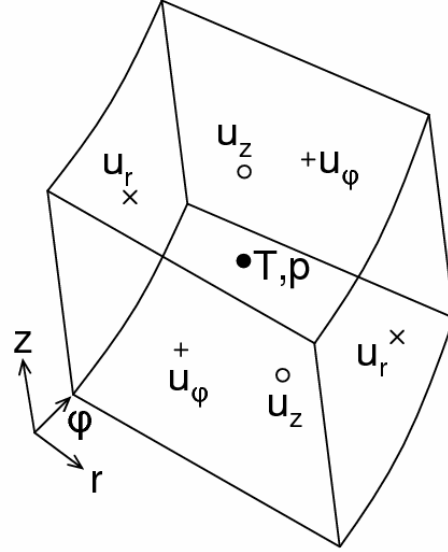
Figure 2.2: Position of variables in a three-dimensional cell on a staggered grid in the cylindrical coordinates. The temperature and pressure are stored at the center of the cell. The velocity components are located at the center of the faces.

computational cost compared to an inversion of a sparse matrix. The resulting tridiagonal system is given by (Verzicco & Orlandi 1996)

$$
\begin{aligned}
(1 - \beta_n A_{i\phi})(1 - \beta_n A_{ir})(1 - \beta_n A_{iz})(\hat{u}_i - u_i^n) &= \Delta t \left(\gamma_n H_i^n + \rho_n H_i^{n-1} - \alpha_n G_i p^n \right) \\
&+ \Delta t \, \alpha_n (A_{i\phi} + A_{ir} + A_{iz}) u_i^n \,,
\end{aligned}
$$

where $\beta_n = \alpha_n \Delta t / 2$. Due to the staggered grid arrangement, boundary conditions for some of the velocity components are required at a particular boundary (Kim & Moin 1985). After elimination of u_i^{n+1} from Eqn. (2.2) by taking the divergence of Eqn. (2.2) and with the help of incompressibility condition, Eqn. (2.3), one can obtain a discrete Poisson equation for the scalar Φ^{n+1} as

$$
\Delta_h \Phi^{n+1} = \frac{1}{\alpha_n \Delta t} D_i \hat{u}_i \,. \tag{2.4}
$$

Here Δ_h is the discrete Laplacian in the cylindrical coordinates. To solve the Poisson equation, Eqn. (2.4), one-dimensional Fast Fourier Transform (FFT) is applied in the azimuthal direction and a two-dimensional Laplace operator is inverted in the r-z plane for each azimuthal mode. The FISHPACK package (Schwarztrauber 1974) is used as the Poisson solver.

2.3 Spatial grid resolution criteria

For fluid with $Pr < 1$, the Kolmogorov scale η_K is the smallest scale to be resolved in DNS simulations of convective turbulence. Recent investigations by Schumacher *et al.* (2005) and Donzis *et al.* (2008) have demonstrated that the smallest scale η_K and the largest wave number k_{max} satisfy the inequality

$$k_{max}\,\eta_K > c\,,\tag{2.5}$$

with $c > 3$ for a well resolved grid. The largest wave number is given by the dealiasing rule as (Orszag 1971)

$$k_{max} = \sqrt{2}N/3\,.\tag{2.6}$$

For $N = L/\Delta$ and $L = 2\pi$ gives $k_{max} \approx \pi/\Delta$. It follows that the mean grid size, Δ, is

$$\Delta \leq \frac{\pi}{c}\eta_K\,.\tag{2.7}$$

Substitution of $\eta_K = \dfrac{\nu^{3/4}}{\langle\epsilon\rangle^{1/4}}$ and $\langle\epsilon\rangle = \dfrac{\nu^3}{L^4}(Nu-1)RaPr^{-2}$ (Grossmann & Lohse 2000) into Eqn. (2.7) yields

$$\Delta \leq \frac{\pi}{c}L\left(\frac{Pr^2}{(Nu-1)Ra}\right)^{1/4}\text{ for } Nu \gg 1.\tag{2.8}$$

This is clearly an improvement over the Grötzbach (1983) criterion, in which $c = 1$. Consequently Δ becomes much smaller if $c = 3$. Hence the DNS grid size according to the Grötzbach criterion is

$$\Delta_G \leq \pi\eta_K = \pi L\left(\frac{Pr^2}{(Nu-1)Ra}\right)^{1/4}\,.\tag{2.9}$$

In the cylindrical coordinate system, the mean grid spacing, $\tilde{\Delta}$, can be estimated as

$$\tilde{\Delta} = \max_{\boldsymbol{x}=(\phi,r,z)}\sqrt[3]{r\Delta_\phi\Delta_r\Delta_z}\,,\tag{2.10}$$

where Δ_ϕ, Δ_r and Δ_z are the grid spacings in the azimuthal, radial and axial directions, respectively. This $\tilde{\Delta}$ should never exceed Δ given by Eqn. (2.9).

2.4 Dependence of DNS grid on the aspect ratio

The aspect ratio for a cylindrical cell is defined as

$$\Gamma = \frac{D}{H} = \frac{2R}{H}\,,\tag{2.11}$$
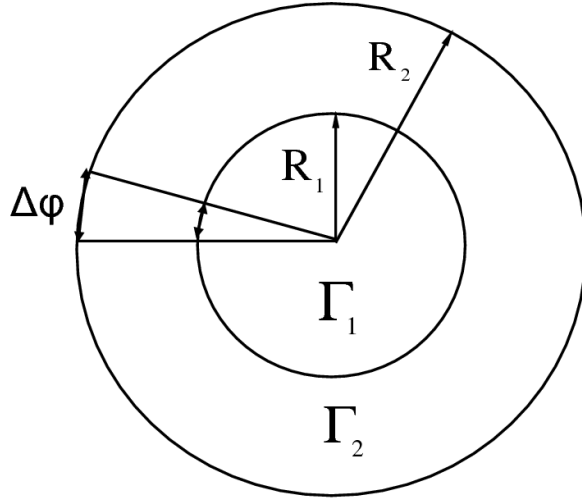
Figure 2.3: Plan view of two concentric cylindrical cells whose aspect ratios are Γ_1 and Γ_2 for the radii R_1 and R_2 ($R_2 > R_1$), respectively.

where R is the radius and H is the height of the cylinder. Now consider two cylindrical cells with a constant height H and aspect ratios Γ_1 and Γ_2 ($\Gamma_2 > \Gamma_1$) as shown in Figure 2.3. Given a small angle $\Delta\phi$, the corresponding azimuthal grid spacings are

$$\Delta x_1 = R_1 \Delta\phi, \tag{2.12}$$
$$\Delta x_2 = R_2 \Delta\phi. \tag{2.13}$$

Here Δx_1 and Δx_2 are the azimuthal grid size at radial positions R_1 and R_2, respectively. With the help of Eqn. (2.11), Eqns. (2.12) and (2.13) give

$$\frac{\Delta x_1}{\Delta x_2} = \frac{R_1 \Delta\phi}{R_2 \Delta\phi} = \frac{\Gamma_1}{\Gamma_2}. \tag{2.14}$$

With an increasing aspect ratio, it is evident form Eqn. (2.14) that Δx_2 must be reduced by a factor Γ_1/Γ_2 in order to sustain the same size as Δx_1. The DNS grid size N is thus a function of the aspect ratio as give by

$$N = \Gamma N_\phi \times \Gamma N_r \times N_z, \tag{2.15}$$

with N_ϕ, N_r and N_z are the number of grid points in the azimuthal, radial and axial directions, respectively. It turns out that N has a growth rate of Γ^2. However, in a cylindrical geometry, the center region is over-resolved compared to the sidewall region.

2.5 Convergence studies

We use the free-fall velocity U_f and free-fall time t_f as normalization factors. These are given by

$$U_f = \sqrt{\alpha g \Delta T H}, \tag{2.16}$$

$$t_f = \frac{H}{U_f}. \tag{2.17}$$

A prefactor C_k, where

$$U_c = C_k U_f, \tag{2.18}$$

is necessary to calculate the appropriate convective velocity U_c and convective time t_c. The prefactor is defined as

$$C_k = \sqrt{\left\langle \frac{u_x^2 + u_y^2 + u_z^2}{U_f^2} \right\rangle_{V,t}}. \tag{2.19}$$

The symbol $\langle \cdot \rangle_{V,t}$ represents an averaging over the cell volume $V = \pi R^2 H$ and an ensemble of statistically independent snapshots. The convective velocity U_c is an alternative definition of the characteristic velocity in terms of the root-mean-square velocity as oppose to U_f. Figure 2.4 displays the plane-averaged C_k (Eqn. 2.19) as

	$N_\phi \times N_r \times N_z$	$\tilde{\Delta}$	Δ_G	η_K	$Nu \pm \sigma$	σ in%	N_{BL}
1	$97 \times 49 \times 64$	0.0221	0.0235	0.0075	16.90 ± 0.11	0.65	8
2	$193 \times 97 \times 128$	0.0110	0.0235	0.0075	16.73 ± 0.08	0.50	14
3	$257 \times 129 \times 210$	0.0077	0.0235	0.0075	16.76 ± 0.05	0.30	24

Table 2.1: Nusselt number convergence for three different grid spacings– (1) coarse grid with $\tilde{\Delta} \approx \Delta_G$, (2) medium grid with $\tilde{\Delta} \approx 0.5\,\Delta_G$ and (3) fine grid with $\tilde{\Delta} \approx \eta_K$ – for the data set $Ra = 10^7$, $Pr = 0.7$ and $\Gamma = 1$. N_{BL} is the number of grid planes inside the thermal boundary layer, $\tilde{\Delta}$– mean DNS grid spacing as in Eqn. (2.10) and Δ_G – the grid spacing according to the Grötzbach criterion, $\tilde{\Delta} \leq \pi \eta_K$, which is given by Eqn. (2.9).

a function of height of the cell for three Rayleigh numbers, namely $Ra = 10^7$, 10^8 and 10^9, and for aspect ratio $\Gamma = 1$. The simulations are conducted over at least 141 nondimensional time units. In can be observed that the values vary between $C_k \approx 0.17$ and 0.19. For wide-aspect-ratio rectangular cells, this factor is typically $C_k \approx 0.1$ (Kerr 1996; van Reeuwijk et al. 2008).

In order to verify the quality of grid spacings in our simulations, we have performed several pilot studies for different grid spacings as provided in Table 2.1 and analyzed
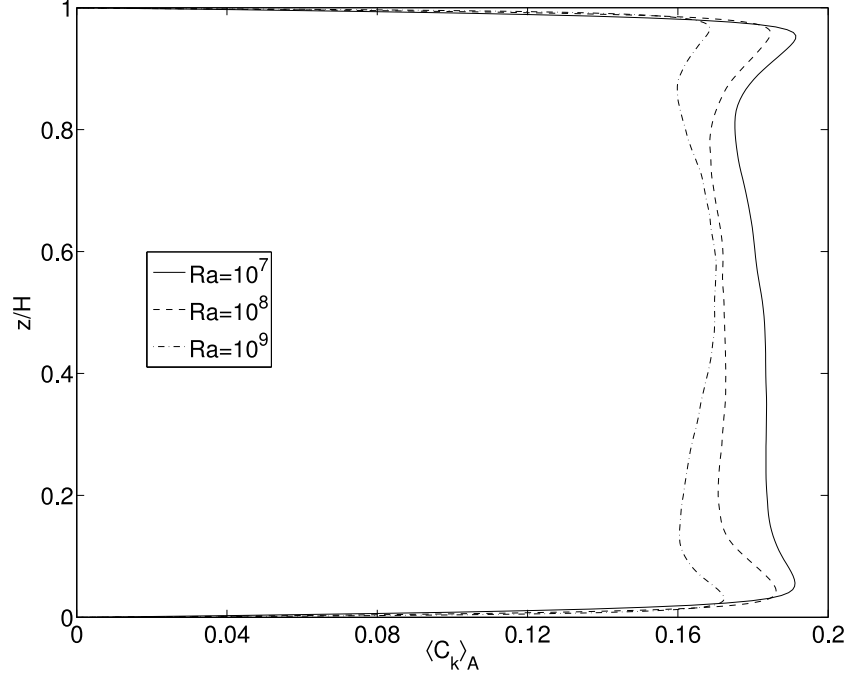
Figure 2.4: Plots of the plane-averaged C_k (Eqn. 2.19) as a function of height of the cell for three Rayleigh numbers – $Ra = 10^7$, 10^8 and 10^9 – and aspect ratio $\Gamma = 1$. The statistics are gathered over at least $141 \times t/t_f$ time units.

the Nusselt number for each case. The global Nusselt number Nu is obtained by integrating Eqn. (1.10) over the cell height as

$$Nu = \frac{1}{H} \int_0^H Nu(z) \mathrm{d}z = 1 + \frac{H}{\kappa \Delta T} \langle u_z T \rangle_{V,t} . \qquad (2.20)$$

The standard deviation σ of Nu is calculated as

$$\sigma = \sqrt{\frac{1}{N_z} \sum_{j=1}^{N_z} [Nu(z_j) - Nu]^2} . \qquad (2.21)$$

Here z_j is the vertical coordinate at gridplane j, and $Nu(z)$ and Nu follow from Eqns. (1.10) and (2.20), respectively. The relative deviation with respect to the mean value is smaller than 1% for all the three cases in Table 2.1 and thus comparable with Kerr (1996).

Figure 2.5 plots $Nu(z)$ over the cell height for the three simulations described in Table 2.1. In case of the coarse grid (simulation No. 1), spike-like jumps in both of the thermal boundary layers and large-amplitude oscillations in the bulk are visible, which result in a higher value of σ compared to the other two cases. Eventhough it satisfies the Grötzbach criterion, the grid planes in the thermal boundary layer are not sufficient to resolve the gradients. In case of the medium and fine grids,
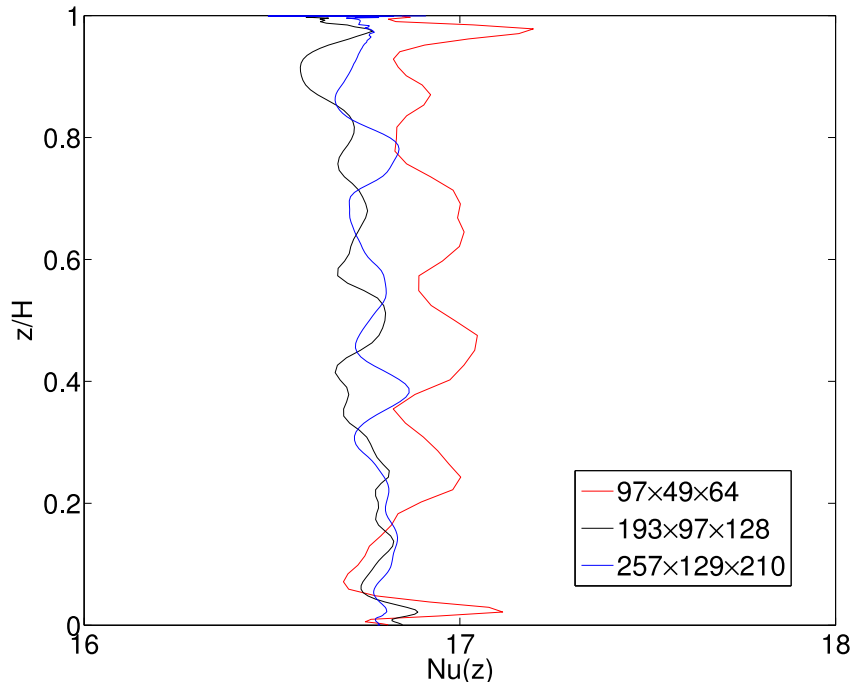
Figure 2.5: Variation of the plane averaged Nusselt number with respect to the height of the cell for three different grid spacings as mentioned in Table 2.1.

simulation No. 2 and 3 respectively, for which the total grid points are increased by an order of magnitude compared to the coarse grid, the $Nu(z)$ profiles are smoother with small standard deviation in the global heat transfer Nu. There is not much improvement from medium to fine grids albeit almost doubling the number of boundary layer grid planes and a denser spacing in the bulk. Therefore, for this particular Rayleigh number, $Ra = 10^7$, we have selected medium grid for further simulations. However, we have adopted $\tilde{\Delta} \approx \Delta_G$ (see Eqn. (2.9)) for simulations with higher Rayleigh numbers ($Ra > 10^7$) and for larger aspect ratios ($\Gamma >> 1$) with a minimum 14 grid planes in the thermal boundary layer. The impact of the resolution on Nu was also discussed recently by Stevens $et\ al.$ (2009).

The smallest mean scale in a turbulent flow is the Kolmogorov dissipation length, which is defined as

$$\eta_K = \frac{\nu^{3/4}}{\langle \epsilon \rangle^{1/4}},$$ (2.22)

where $\langle \epsilon \rangle$ is the mean of the energy dissipation rate (Pope 2000), which is given by

$$\epsilon(\boldsymbol{x}, t) = \frac{\nu}{2} \left(\frac{\partial u_i}{\partial x_j} + \frac{\partial u_j}{\partial x_i} \right)^2.$$ (2.23)

The resolution criteria based on η_K works well in homogeneous isotropic turbulence, but has to be modified for the inhomogeneous situation. As we will see in chapter 4
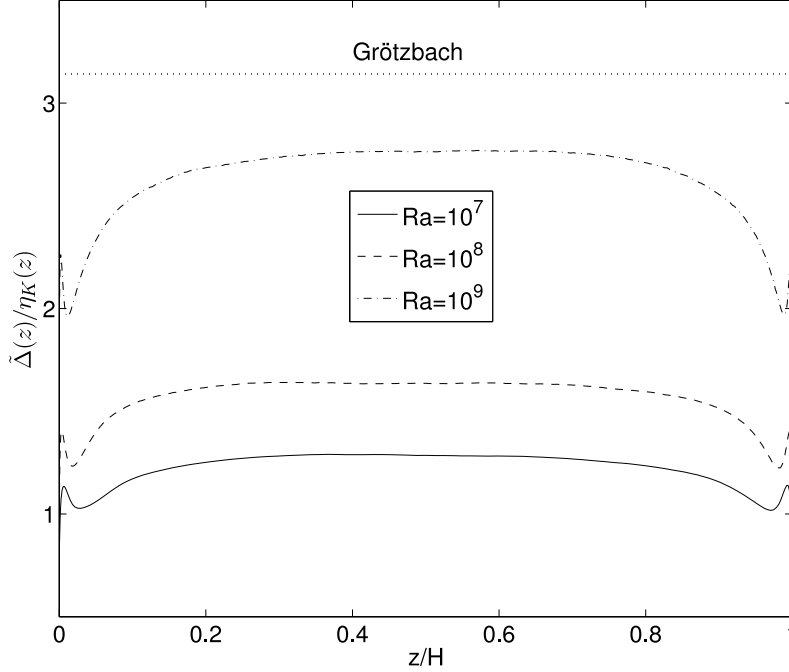
Figure 2.6: Ratio of the maximum geometric mean grid spacing $\tilde{\Delta}(z)$ and the Kolmogorov scale $\eta_K(z)$ (see Eqn. (2.24)) for three different Rayleigh numbers in a cell with aspect ratio $\Gamma = 1$. The horizontal dotted line indicates the global Grötzbach resolution criterion $\tilde{\Delta}/\eta_K \leq \pi$.

that the mean dissipation rate is strongly height-dependent in our investigations, we define a height-dependent Kolmogorov scale as

$$\eta_K(z) = \frac{\nu^{3/4}}{\langle \epsilon(z) \rangle_{A,t}^{1/4}} \, . \tag{2.24}$$

Figure 2.6 displays the ratio $\tilde{\Delta}(z)/\eta_K(z)$ over the cell height for three different Rayleigh numbers, namely $Ra = 10^7$, 10^8 and 10^9 for simulations in a cell with aspect ratio $\Gamma = 1$. One can observe that the ratio varies close to the upper and lower plates and levels off in the bulk. Overall, it does not exceed the global resolution criterion by Grötzbach (1983), $\tilde{\Delta} \leq \pi\eta_K$ as in Eqn. (2.9), for the given Rayleigh numbers.

3 Statistics of the temperature and its gradients

In this chapter we study the fine-scale statistics of the temperature field in turbulent Rayleigh-Bénard convection in a cylindrical cell with aspect ratio $\Gamma = 1$ for a moderate Rayleigh number range $Ra = 10^7 - 10^9$. We provide detailed statistics of the temperature T, its fluctuations θ and the vertical derivative $\partial_z \theta$ as well as the skewness and flatness for different quantities. We also compare our results with the passive scalar case.

3.1 Mean temperature and temperature fluctuations

In Rayleigh-Bénard convection, coherent thermal elements continuously detach from the thermal boundary layers and tend to rise from a hotter to a colder region, and fall from a colder to a hotter region due to the action of buoyancy force before they disappear in the bulk as their temperature matches with the surrounding ones. Figure 3.1 shows such thermal plume-activity in a cell with aspect ratio $\Gamma = 1$ for the simulation at $Ra = 10^8$. In the top panel, 3D isosurfaces denote the dimensionless temperature, where the red color (hot plumes) corresponds to isolevel 0.7 and the blue color (cold plumes) corresponds to isolevel 0.3. A 2D temperature isosurface in rz-plane through $\phi = 0 - \pi$ line is shown in the bottom panel. We wish to study now which impact these coherent structures have on the statistics of temperature field. We also see in the figure a thin hot and cold layer at the bottom and top plates, respectively. This is the thermal boundary layer and its thickness is defined as

$$\delta_T = \frac{1}{2Nu}.$$ (3.1)

Since $Pr = 0.7$ in our studies, the associated velocity boundary layer has about the same thickness as δ_T. Plumes can be considered as fragments of the thermal boundary layer, which detach randomly from both plates.

The temperature field is decomposed into a mean profile $\langle T \rangle_{A,t}$ and fluctuations θ as

$$T(\boldsymbol{x}, t) = \langle T \rangle_{A,t}(z) + \theta(\boldsymbol{x}, t).$$ (3.2)

The symbol $\langle . \rangle_{A,t}$ denotes an averaging over the horizontal plane and an ensemble of statistically independent snapshots. Sometimes, we omit the subscript t in such
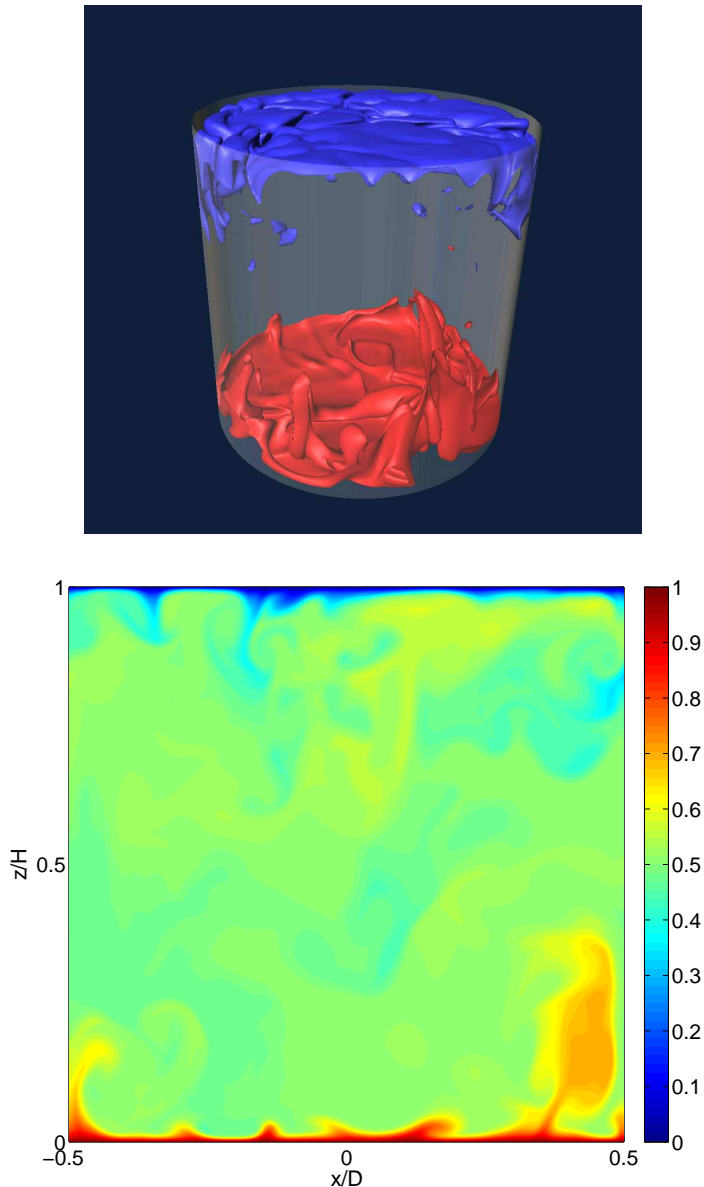
Figure 3.1: Instantaneous temperature isosurface plots show the rising and falling plumes in a cylindrical cell with aspect ratio $\Gamma = 1$ for the simulation at $Ra = 10^8$. In the top panel, the red color (hot plumes) corresponds to isolevel 0.7 and the blue color (cold plumes) corresponds to isolevel 0.3. In the bottom panel, a 2D temperature isosurface in rz-plane along $\phi = 0 - \pi$ line is shown.

averaging for the simplification. We plot the mean temperature profiles for three different cases for the simulation at $Ra = 10^8$ in the cell with aspect ratio $\Gamma = 1$ in Figure 3.2. The standard plane-averaged mean profile $\langle T \rangle_A(z)$ is compared with two other profiles, which are taken at two fixed radial positions– close to the axis $(r \approx 2\Delta_r)$ and close to the sidewall $(r \approx R)$ – and averaged azimuthally. It can be

Figure 3.2: Mean temperature profiles at $Ra = 10^8$, $\Gamma = 1$. The standard profile $\langle T \rangle_A(z)$ is compared with two other profiles, which are calculated at fixed radial positions and averaged azimuthally. One is taken at the sidewall ($r \approx R$), the other is close to the axis of the cell ($r \approx 2\Delta_r$). All mean profiles vary from 0 to 1 along the horizontal axis but only interval $[0.4, 0.6]$ is shown.

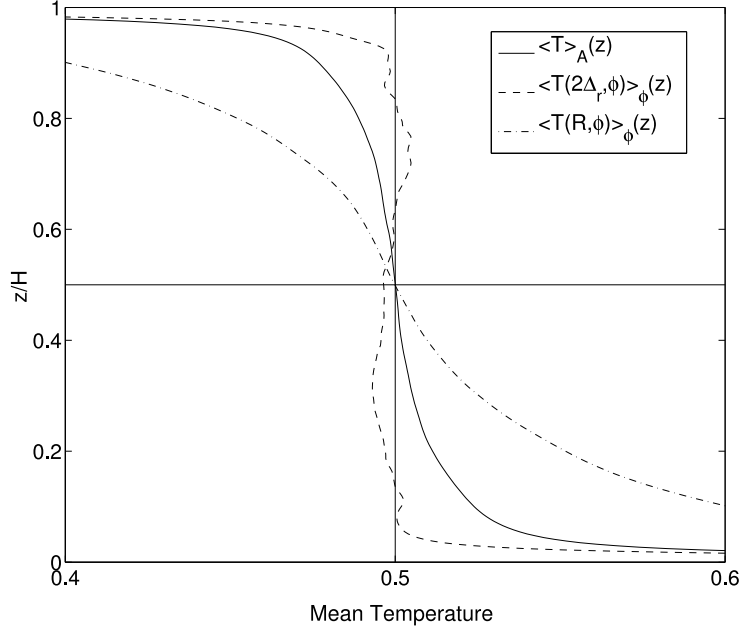| Ra	Nu	Re	$N_\phi \times N_r \times N_z$	Δ_G	$\tilde{\Delta}$	δ_T	$\tilde{\delta}_T$	t/t_f
1×10^7	16.73	682	$193 \times 97 \times 128$	0.0236	0.0104	0.0300	0.0253	151
5×10^7	25.86	1444	$257 \times 129 \times 160$	0.0139	0.0080	0.0193	0.0162	151
1×10^8	31.67	2036	$271 \times 151 \times 200$	0.0111	0.0069	0.0158	0.0138	151
5×10^8	52.43	4530	$301 \times 201 \times 256$	0.0065	0.0058	0.0095	0.0084	151
1×10^9	65.00	6255	$361 \times 181 \times 310$	0.0053	0.0051	0.0077	0.0065	82

Table 3.1: List of parameters for different simulations. The Nusselt number is calculated as in Eqn. (2.20). The Reynolds number Re is based on the rms velocity as in Eqns. (3.3)–(3.4) and follows $Re = 0.33 Ra^{0.475}$. Grid spacings Δ_G and $\tilde{\Delta}$ are given by the Grötzbach criterion, Eqn. (2.9), and Eqn. (2.10), respectively. δ_T is determined as $H/(2Nu)$ and $\tilde{\delta}_T$ is estimated from the variance of temperature fluctuations profiles $\langle \theta^2 \rangle_A(z)$ (Figure 3.3). The convective time unit is $t_c = C_k t/t_f$, with $C_k \approx 0.17 - 0.19$ from Figure 2.4. We have improved the statistics for some simulations for the aspect ratio dependence analysis (see Table 5.1 in chapter 5).

seen that the slopes of the temperature profiles vary significantly. While the profile $\langle T \rangle_A(z)$ has almost zero slope at $z = 0.5$, a destabilizing slope, $d\langle T \rangle_\phi(z)/dz < 0$, is observed close to the sidewall. Close to the center, the situation is reversed,
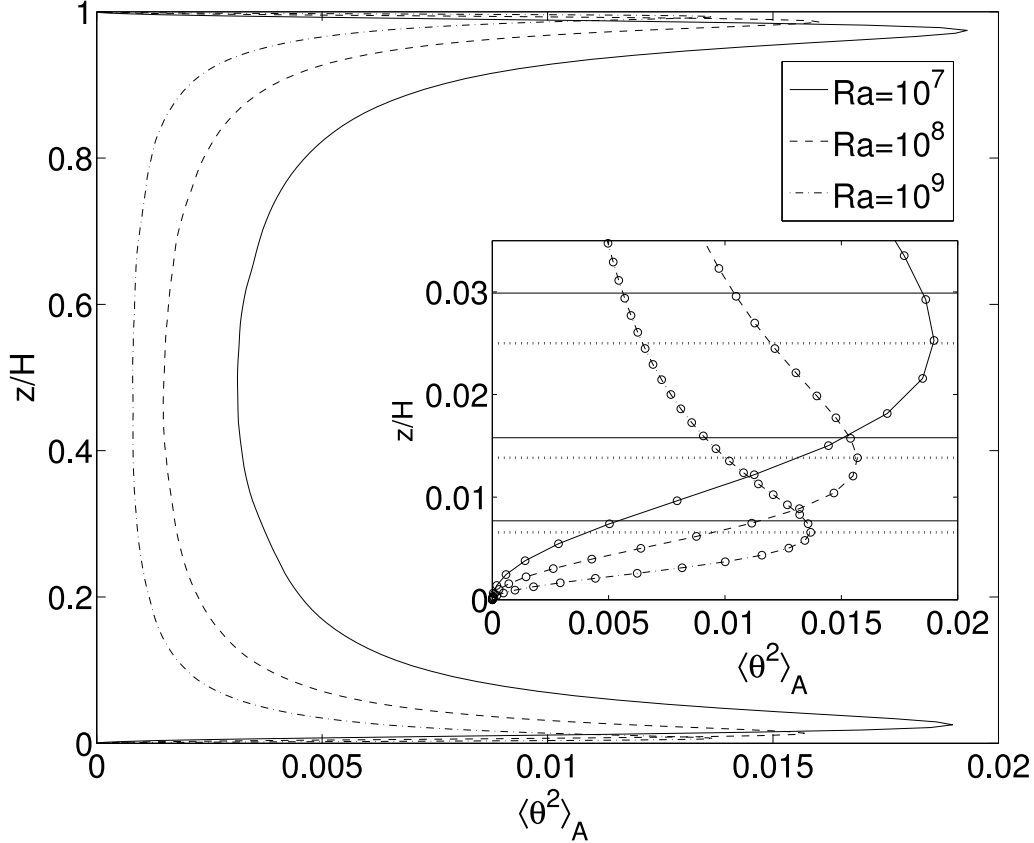
Figure 3.3: Mean square fluctuations $\langle\theta^2\rangle_A$ as a function of z/H for three Rayleigh numbers– $Ra = 10^7, 10^8$ and 10^9– for aspect ratio $\Gamma = 1$. The inset magnifies the thermal boundary layer. The solid horizontal lines in the inset correspond to $\delta_T = H/(2Nu)$ and the dotted lines for $\tilde{\delta}_T$, the distance at which the maximum of $\langle\theta^2\rangle_A$ intersect the z axis.

where we observe a stabilizing slope, $d\langle T\rangle_\phi(z)/dz > 0$. Our finding agrees with the recent experiment by Brown & Ahlers (2007) and confirms that the assumption of the temperature drop ΔT across the thermal boundary layer is rather a simplification, which, however, works well for many considerations. The presence of a non-vanishing local mean temperature gradient can have an impact on the statistics of the small-scale temperature fluctuations, similar to the passive scalar case. This point will be discussed in more detail in section 3.2. The thickness of the thermal boundary layer, δ_T, can be estimated either by $\delta_T = H/(2Nu)$ or from the maximum value of the variance of temperature fluctuations, $\langle\theta^2\rangle_A$, profile. We denote the later definition as $\tilde{\delta}_T$. Both definitions differ by a small magnitude as can be seen in Table 3.1. The grid planes in the thermal boundary layer for various simulations are listed there as well. We plot $\langle\theta^2\rangle_A$ as a function of height of the cell in Figure 3.3 for three different Rayleigh numbers and a fixed aspect ratio $\Gamma = 1$. In the inset of this Figure, deviations between δ_T and $\tilde{\delta}_T$ are highlighted.
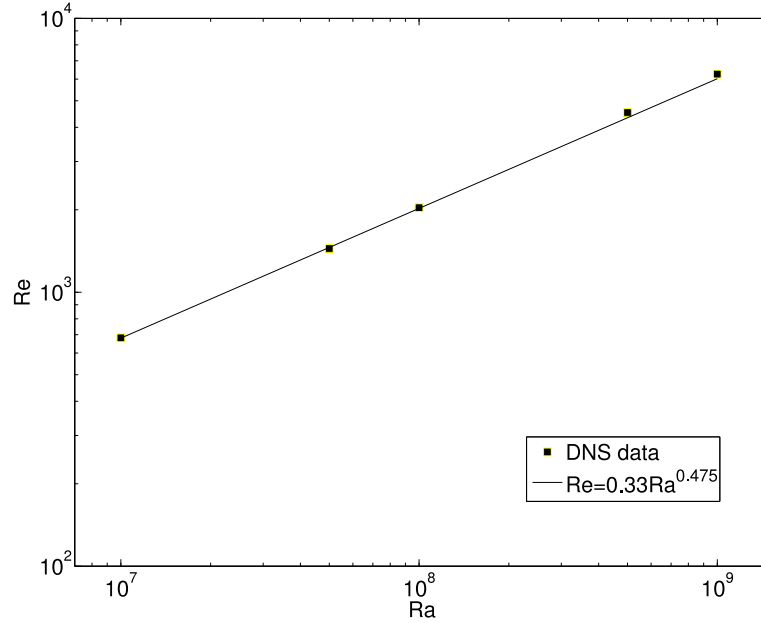
Figure 3.4: Log-log plot of Re as a function of Ra for five simulations in Table 3.1. The DNS results agree with the power law $Re = 0.33Ra^{0.475}$.

The Reynolds number Re can be estimated as

$$Re = \frac{U_{rms}H}{\nu} , \qquad (3.3)$$

where the rms velocity U_{rms} is given by

$$U_{rms} = \sqrt{\left\langle u_x^2 + u_y^2 + u_z^2 \right\rangle_{V,t}} . \qquad (3.4)$$

Here $\langle . \rangle_{V,t}$ represents an averaging over the whole volume and an ensemble of statistically independent turbulent fields. Figure 3.4 displays Re as a function of Ra for the data set provided in Table 3.1 in logarithmic scale. A power law $Re = 0.33Ra^{0.475}$ is obtained for the DNS data set, which is roughly in agreement with Brown *et al.* (2007) and van Reeuwijk *et al.* (2008).

3.2 Higher-order temperature statistics

Figure 3.5 shows the probability density functions (PDFs) of the dimensionless temperature $\tilde{T}$ at different heights from the bottom plate as a function of the Rayleigh number. The findings are in agreement with Siggia (1994), Kerr (1996) and He & Tong (2009). As expected, the PDFs in Figure 3.5a become increasingly symmetric toward the center of the convection cell. This height-dependent asymmetry can be

measured alternatively by the skewness of temperature fluctuations, S_θ, which is given by

$$S_\theta(z) = \frac{\langle \theta^3 \rangle_A}{\langle \theta^2 \rangle_A^{3/2}}. \tag{3.5}$$

The graphs of $S_\theta(z)$ are shown in Figure 3.6a. A small skewness around $\delta_T = 1$
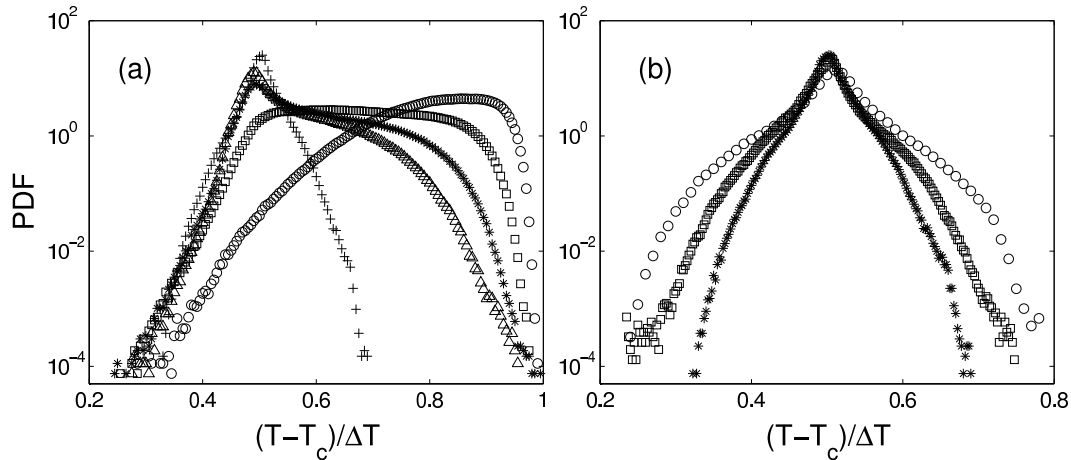
Figure 3.5: Probability density functions (PDF) of the dimensionless temperature $\tilde{T}$. (a) All data points are taken for $Ra = 10^9$ and for the whole plane at height z. Heights are $z = 0.5\delta_T$ ($\circ$), $z = \delta_T$ ($\square$), $z = 2\delta_T$ ($*$), $z = 4\delta_T$ ($\triangle$) and $z = 0.5H$ ($+$). (b) Data points are taken at the center plane $z = 0.5$ for different Rayleigh numbers: $Ra = 10^7$ ($\circ$), $Ra = 10^8$ ($\square$) and $Ra = 10^9$ ($*$).
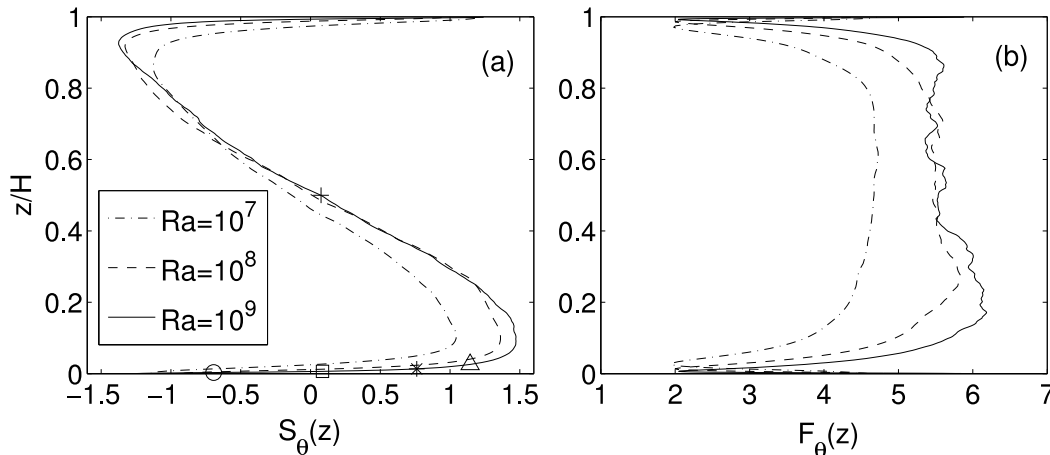
Figure 3.6: Height dependence of the skewness (a) and flatness (b) of the temperature fluctuations. Data points are given for three Rayleigh numbers as shown in the legend. The symbols in the skewness curve of $Ra = 10^9$ indicate the distances from the wall for which the PDFs in Figure 3.5a are plotted.
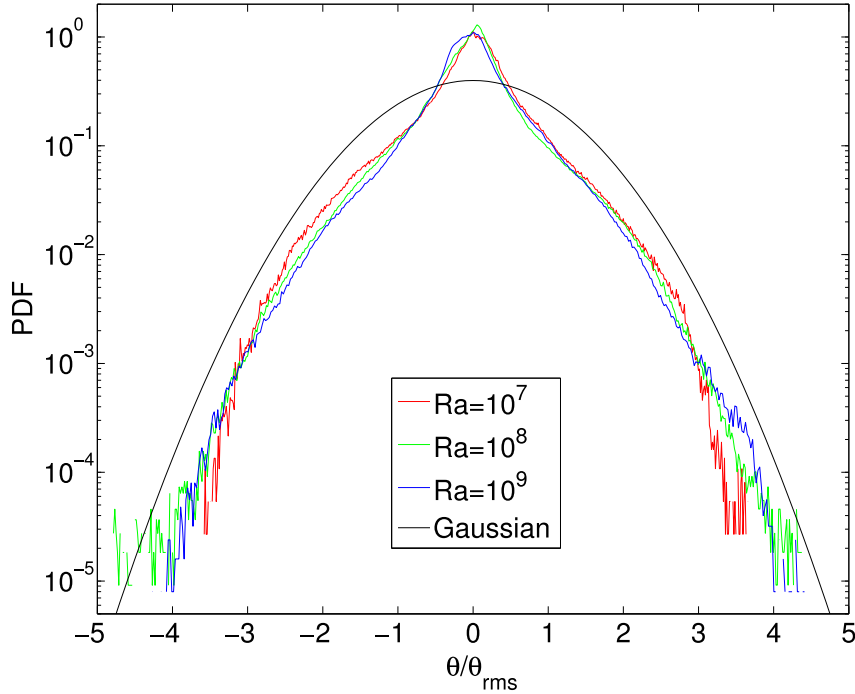
Figure 3.7: The PDFs the temperature fluctuations, θ, in the center plane ($z = 0.5H$) for different Rayleigh numbers as shown in the legend. The simulations are conducted in a cell with aspect ratio $\Gamma = 1$. Each PDF is normalized with the corresponding rms value calculated over the horizontal plane area, $A = \pi R^2$, at $z = 0.5H$.

implies that rising and falling plumes are present at the edge of the bottom and top thermal boundary layers. Simultaneously, the colder and hotter pockets of temperature are generated in the vicinity of the thermal plumes which detach from the thermal boundary layer. This is a consequence of the incompressibility of the fluid as investigated more detailed in the Lagrangian frame of reference by Schumacher (2008, 2009). Up to a height of $z/H \approx 0.1$, the skewness increases monotonically before it declines to zero at the cell center plane. The plots show that the maximum value of skewness increases with increasing Rayleigh number. A large positive value of the skewness close to the bottom plate means that rising plumes with $T(z) > \langle T \rangle_A(z)$ are dominant in this region of the convection cell. The distribution of the temperature in the center plane ($z = 0.5$) of the cell as a function of the Rayleigh number is shown in Figure 3.5b. The profiles are clearly non-Gaussian for all three Rayleigh numbers. The support of the PDF becomes narrower with increasing Ra. The PDF for the fluctuations θ has similar shape in the center plane (Figure 3.7). We find that the PDFs for the two larger Rayleigh numbers almost collapse when θ is normalized by the corresponding root-mean-square value, θ_{rms}. The PDF for $Ra = 10^7$ has slightly smaller tails and all distributions are sub-Gaussian.

The magnitude of the deviations from Gaussianity can be measured by the flatness which is given by

$$F_\theta(z) = \frac{\langle \theta^4 \rangle_A}{\langle \theta^2 \rangle_A^2} . \tag{3.6}$$

Figure 3.6b shows the vertical profiles of the flatness for three Rayleigh numbers. The non-Gaussianity, i.e., a flatness larger than 3, is present for all three cases. This is in agreement with other studies such as by Heslot *et al.* (1987), Castaing *et al.* (1989) and Ching (1991). It can also be observed that the flatness values almost match each other in the bulk for the two larger Rayleigh numbers. This could indicate that the transition to the so-called hard turbulence regime of convection has been completed. Dimotakis (2005) discussed a mixing transition for passive scalars at $Re \sim 10^4$. Above this threshold, a weaker Re dependence was predicted. A similar behavior could be the reason for our observation (our $Re = 6255$ for $Ra = 10^9$, see Table 3.1). All flatness profiles have a minimum right above the thermal boundary layer. The slight asymmetry of the profile at $Ra = 10^9$ is due to limitations in the statistical analysis. Even a longer time advancement and 140 statistically independent snapshots were not sufficient to obtain a symmetric profile since the flatness analysis is done plane by plane.
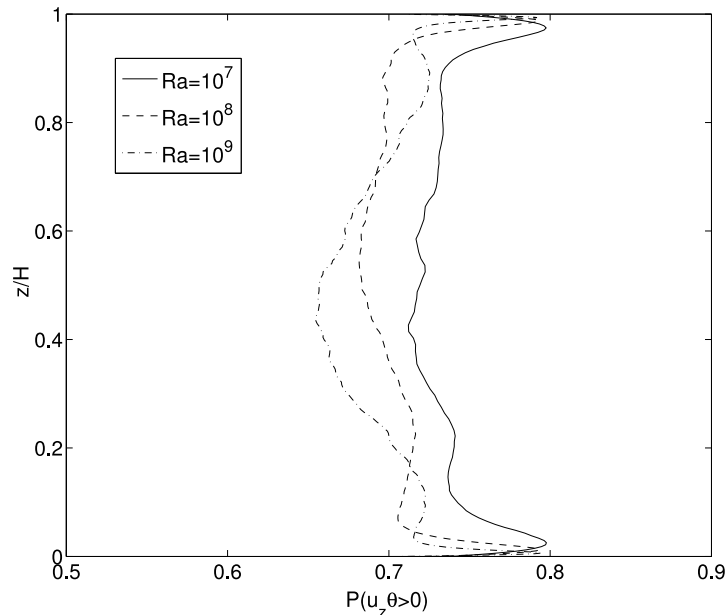

Figure 3.8: Vertical profiles of the probability of $u_z\theta > 0$ for three different Rayleigh numbers.

As already seen, the non-Gaussian PDF of the total temperature and the temperature fluctuations in the cell center is a robust feature in thermal convection. Similar behavior was observed in experiments by Heslot *et al.* (1987) and Castaing *et al.*

(1989). Almost an exponential shape was emphasized by Yakhot (1989) on the basis of a hierarchy of moment equations for the temperature fluctuations. These ideas have been extended by Ching (1993) later. Yakhot suggested that this form prevails even for moderate Rayleigh numbers (which implies moderate Reynolds numbers), whenever regions with $u_z\theta > 0$ are dominant. A correlation between the vertical velocity and temperature fluctuation is nothing else but a fingerprint of a local blob of heat transferred through the cell. Inspection of our data yields indeed that larger regions with $u_z\theta > 0$ are present everywhere in the cell, even in the center where coherent plumes are absent. This is shown in Figure 3.8 where we plot the height dependence of the probability $P(u_z\theta > 0)$ for three different Rayleigh numbers. It can be clearly seen that the probability decreases with increasing Rayleigh number, but remains significantly larger than 0.5 for all three cases. The outcome is another manifestation of the net transfer of heat through the cell.

The passive scalar turns out to be more sensitive to a particular driving and the Reynolds number of the advecting flow. When a mean scalar gradient is absent, the statistics is close to Gaussian or sub-Gaussian as observed by Mydlarski & Warhaft (1998) and Watanabe & Gotoh (2004). In case of a non-vanishing mean scalar gradient, based on a simple one-dimensional random advection model, Pumir *et al.* (1991) suggested that an exponential distribution is a generic feature in passive scalar convection. This was confirmed experimentally for sufficiently high Reynolds numbers (Gollub *et al.* 1991; Jayesh & Warhaft 1991, 1992). However, sub-Gaussian distributions of θ have also been found for the passive scalar turbulence by Overholt & Pope (1996), Ferchichi & Tavoularis (2002) and Schumacher & Sreenivasan (2005). Experiments by Gylfason & Warhaft (2004) observed that the statistics depends on a particular driving of the turbulent flow. While an active grid caused sub-Gaussian fluctuations, a fine static grid caused super-Gaussian passive scalar distributions. Furthermore, the deviations from Gaussian distributions decreased with increasing downstream distance in their experiments. The two findings imply that the ratio of the integral scales to the system scale is important. This point needs to be addressed more detailed in the future.

3.3 Vertical derivative of temperature fluctuations

An important question in turbulent convection is whether the fluctuations of the temperature field in the bulk can be considered as being locally isotropic. In order to shed light on this point we adopt an approach that has been used successfully for passive scalars with a mean scalar gradient (Warhaft 2000). As we have seen in Figure 3.2, the local mean temperature gradient can deviate from zero while the overall profile sums up to a mean temperature gradient which is almost zero. Following Brown & Ahlers (2007), we define a ratio Ξ that relates a difference of the azimuthally averaged mean temperatures at fixed radial distance r_0 to the total

temperature drop. It is given by

$$\Xi(r_0) = \frac{\langle T(r_0)\rangle_\phi(z = 3H/4) - \langle T(r_0)\rangle_\phi(z = H/4)}{\Delta T} . \qquad (3.7)$$

Close to the sidewall, we get $\Xi(R) = -0.12$, -0.07 and -0.04 for $Ra = 10^7$, 10^8 and $Ra = 10^9$, respectively. This slope is mainly due to the rising and falling plumes along the large-scale circulation. Close to the axis of the cell, it follows $\Xi(2\Delta_r) = 0.015$, 0.009 and 0.006 for $Ra = 10^7$, 10^8 and 10^9, respectively. Although decreasing with increasing Rayleigh number for both cases, their magnitude is not negligible. We observe that local mean temperature gradients are present. This supports the idea to conduct an analysis similar to that in passive scalar turbulence. The statistics of the vertical derivative of the temperature, $\partial_z \tilde{T}$, is shown in
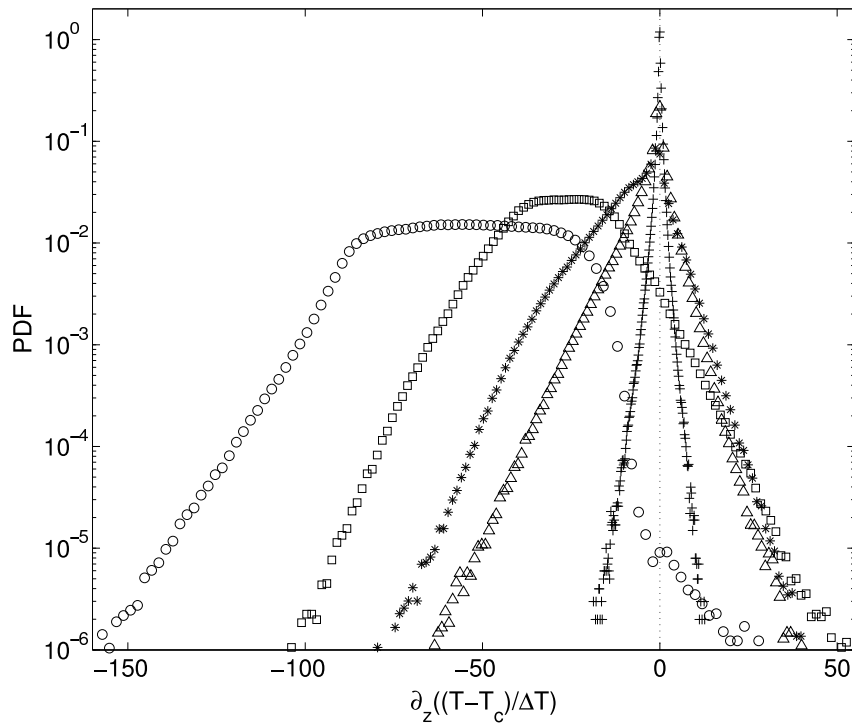
Figure 3.9: Probability density functions (PDF) of vertical derivative of the temperature, $\partial \tilde{T}/\partial z$, taken in the same planes as in Figure 3.5a. The data set is for $Ra = 10^9$ and $\Gamma = 1$. Heights are $z = 0.5\delta_T$ ($\circ$), $z = \delta_T$ ($\square$), $z = 2\delta_T$ ($*$), $z = 4\delta_T$ ($\triangle$) and $z = 0.5H$ ($+$).

Figure 3.9. The PDFs are taken at the same heights as those for the temperature in Figure 3.5a. A sharp decrease of the PDF at $0.5\delta_T$ is present in the vicinity of $\partial_z \tilde{T} = 0$, simply because positive vertical derivatives are very unprobable close to the bottom plate. With increasing distance from the plate, the support of the PDF decreases. A negative skewness of all distributions can be observed which implies preferential derivatives along the mean negative temperature gradient. Recall also

that a turbulent field is thought to be perfectly locally isotropic when all odd-order derivative moments are exactly zero. The derivative skewness with respect to the temperature fluctuations θ is defined as

$$S_{\partial_z\theta}(z) = \frac{\left\langle \left(\frac{\partial\theta}{\partial z}\right)^3 \right\rangle_V}{\left\langle \left(\frac{\partial\theta}{\partial z}\right)^2 \right\rangle_V^{3/2}} \,. \tag{3.8}$$

It measures the deviations from the local isotropy at smaller scales in convective turbulence. Figure 3.10 shows that such deviations are indeed present in different regions of the cylindrical domain. With increasing Rayleigh number and thus increasing Reynolds number, the derivative skewness $S_{\partial_z\theta}(z)$ decreases in magnitude in the bulk (see Figure 3.10a). Following the original idea of the return to local isotropy in a simple shear flow (Lumley 1967) and its adoption to the passive scalar case (Warhaft 2000), a return would require a rather rapid decay of the skewness with respect to the Taylor microscale Reynolds number R_λ, i.e.

$$|S_{\partial_z\theta}| \sim R_\lambda^{-1} \,. \tag{3.9}$$

This was not found in passive scalar case for Schmidt numbers around unity
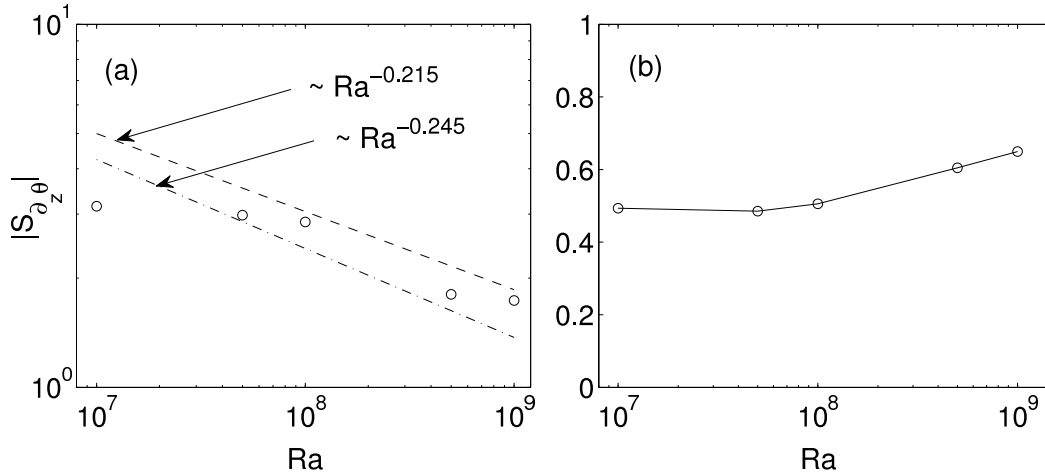
Figure 3.10: Skewness of the vertical temperature derivative as a function of the Rayleigh number Ra. (a) Data analysis is performed in the bulk of the cell for points in $V = \{r, \theta, z \,|\, 0.4H \leq z \leq 0.6H\}$. Data points are displayed in double-logarithmic axes. In addition, the decay laws of the skewness with respect to Ra are shown. The decay is in line with a return to isotropy (dashed lines). (b) Analysis is conducted in the thermal boundary layer for points in $V = \{r, \theta, z \,|\, 0 \leq z \leq \delta_T\}$. Points are plotted in logarithmic-linear diagram.

(Warhaft 2000). Given the scaling dependence of the Reynolds number with respect to the Rayleigh number, which will be discussed in more detail in section 4.3,

and the relation $Re \sim R_\lambda^2$, a return to local isotropy in convection would require a decay law which is given by

$$|S_{\partial_z\theta}| \sim Ra^{-\zeta/2}, \tag{3.10}$$

for a fixed Pr. Here ζ is the scaling exponent for the relation $Re \sim Ra^\zeta$, which was found to vary between $\zeta = 0.43$ and 0.49 in experiments (Brown *et al.* 2007). Figure 3.10a indicates that our data follow such a decay law for the larger Rayleigh numbers. This is in line with the observation that the local mean gradients in the bulk decrease in magnitude with increasing Ra. The mean temperature gradient still causes ramps and cliffs of the temperature and thus a non-vanishing derivative skewness, but its impact seems to be weaker compared to a passive scalar which lacks a return to isotropy trend. A larger range of Rayleigh numbers and the analysis of the hyperskewness would allow to draw a firm conclusion.

The opposite trend with respect to the Rayleigh number can be observed in the thermal boundary layer where the skewness $S_{\partial_z\theta}(z)$ is increasing in magnitude with growing Rayleigh numbers (see Figure 3.10b). Figure 3.9 shows that the PDFs of $\partial_z\tilde{T}$ have strong negative skewness, in particular, in the boundary layer. This observation is due to the fact that the heat transfer is mostly contributed by the second term of Eqn. (1.10) and that the fluctuations about the mean are consequently dominated by the conductive contributions $j_z = -\kappa\partial_z\theta$. We come back to this point in the next chapter when discussing the height dependence of thermal dissipation rate in chapter 4.
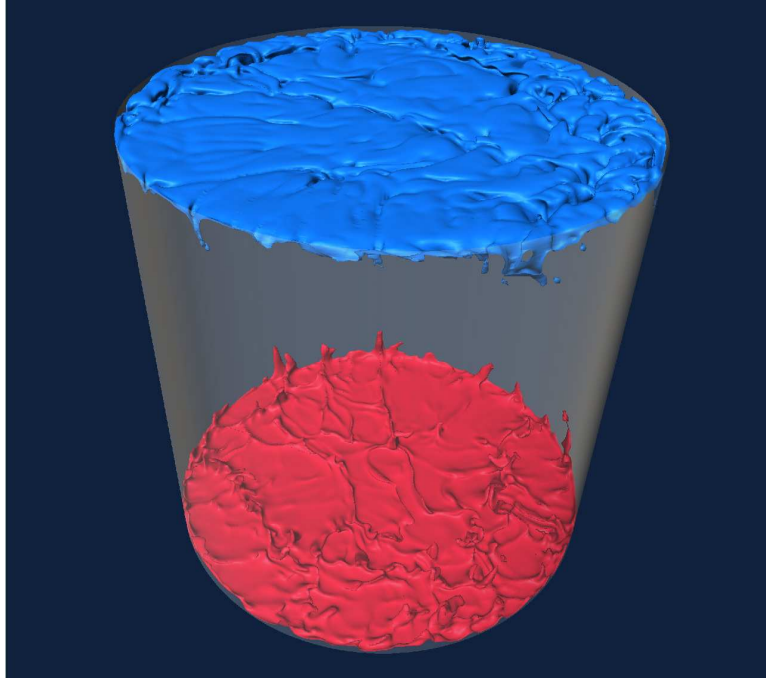
4 Thermal dissipation rate

Thermal dissipation rate in convective turbulence plays an important role in understanding the transport of heat through the convection cell since its volume-averaged quantity is directly correlated to the global heat transfer (Eqn. 1.21). The local temperature dissipation field, $\epsilon_T(\boldsymbol{x}, t)$, provides vital information in understanding the dynamics and morphology of the coherent thermal elements – i.e., plumes, which can be observed in Figure 4.1. Measurement of ϵ_T is very challenging from the experimental perspective since it involves simultaneous measurement of the temperature at different spatial points. Moreover, it is almost impossible to determine the global quantity – the volume-averaged temperature dissipation rate $\langle \epsilon_T \rangle_V$ – in experiments since the spatial resolution is constrained. It is also difficult to resolve the thermal boundary layer, δ_T, due to the dimension of the temperature probe, which could be larger then δ_T. However, the DNS data base provides a complete picture of any field variable in turbulent convection.

In this chapter, we analyze the vertical profiles of the thermal dissipation rate and its probability distributions in different sub-volumes, namely the bulk and boundary layer, of the convection cell. Motivated by the work of Grossmann & Lohse (2004), we propose new definitions of the plume and background dominated thermal dissipation rate fractions, which are conditioned with respect to the quantity $u_z \theta$. We present detailed scaling relations of ϵ_T with respect to Ra, based on our new definitions as well as the bulk and boundary layer contributions and make a comparative study. Our aim is to understand the discrepancies between the theories (e.g. Grossmann & Lohse 2000, 2004) and experiments (e.g. He *et al.* 2007; He & Tong 2009).

4.1 Instantaneous field of $\epsilon_T(\boldsymbol{x}, t)$

Figure 4.1 presents the isosurface plots of an instantaneous snapshot of T (Figure 4.1a) and ϵ_T (Figure 4.1b) for the simulation at $Ra = 10^9$ in the convection cell with aspect ratio $\Gamma = 1$. We recognize the ridges in the temperature isosurface which correspond to the plumes that detach from the bottom and top boundary layers. Associated with the rising and falling plumes are larger amplitudes in the thermal dissipation rate field which can be observed in Figure 4.1b, similar to findings by Kerr (1996) and Shishkina & Wagner (2007). The pattern of ridges (or

(a) Temperature field with isolevels 0.7 (red) and 0.3 (blue).
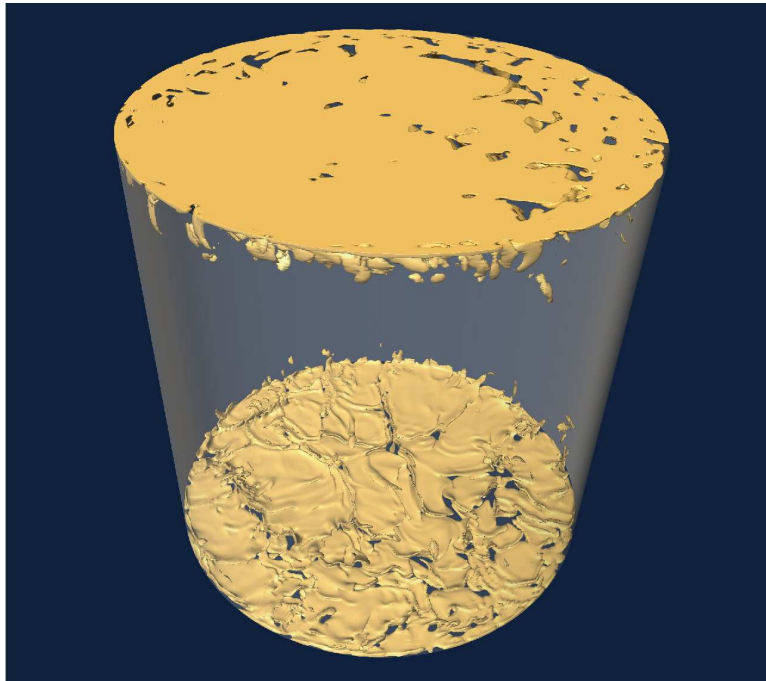
(b) Thermal dissipation rate field with isolevel $10 \times \langle \epsilon_T \rangle_V$.

Figure 4.1: Instantaneous snapshot of the temperature and the thermal dissipation rate in turbulent convection. The simulation is conducted for $Ra = 10^9$ in the aspect ratio $\Gamma = 1$ cell.

(a) $T(r, \phi, z_0, t_0)$ at $z_0 = \delta_T$

(b) $\epsilon_T(r, \phi, z_0, t_0)$ at $z_0 = \delta_T$

(c) $T(r, \phi, z_0, t_0)$ at $z_0 = H/2$

(d) $\epsilon_T(r, \phi, z_0, t_0)$ at $z_0 = H/2$
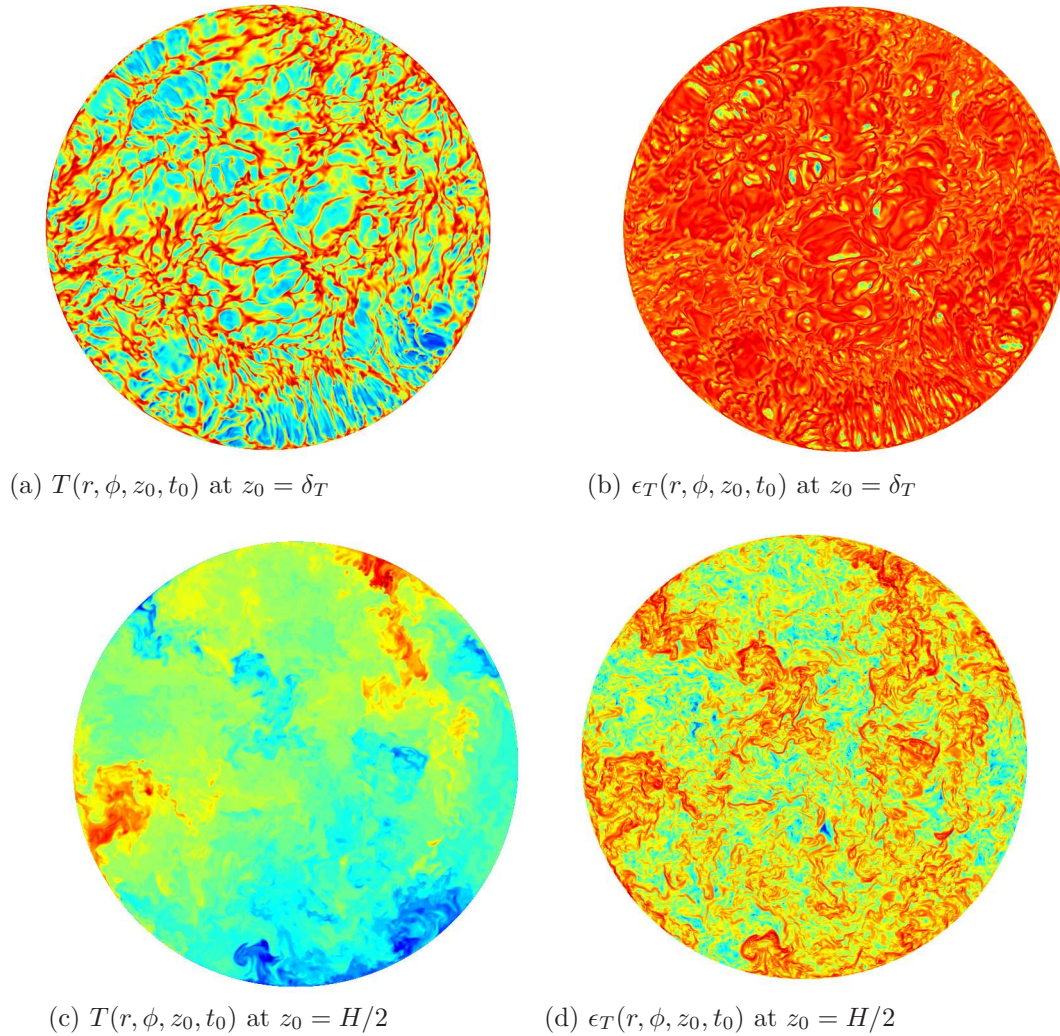
Figure 4.2: Contour plots of the total temperature and the thermal dissipation rate for the simulation at $Ra = 10^9$ and $\Gamma = 3$. Two-dimensional slices of instantaneous fields are taken: (a,b) at $z_0 = \delta_T$ and (c,d) at $z_0 = H/2$. Contours of ϵ_T in (b,d) are plotted in log_{10} scale.

stems) in Figure 4.1a is recaptured almost one-to-one in Figure 4.1b. The plot also indicates that the local maxima of the thermal dissipation rate field ϵ_T are dominant close to the both plates and not in the cell center. Two dimensional contour plots of instantaneous temperature and thermal dissipation rate field are shown in Figure 4.2. The 2D-slices are taken at different heights – close to the boundary layer, $z_0 = \delta_T$, and at the center plane, $z_0 = H/2$ – in a cylindrical cell with aspect ratio $\Gamma = 3$ and for a simulation at Rayleigh number $Ra = 10^9$. While the temperature contours in Figure 4.2a are closely related to the permanent and random detachment of thermal plumes, the contours in Figure 4.2c resemble to those of the passive scalar which is stirred and advected in homogeneous turbulence

(Watanabe & Gotoh 2004). The corresponding contours of the thermal dissipation field in Figures 4.2b and 4.2d illustrate clearly the strong vertical inhomogeneity in the convection cell. The inhomogeneity is also reflected in the statistics of $\epsilon_T(\boldsymbol{x}, t)$, which is explained in section 4.2.

4.2 Vertical profiles of ϵ_T

In order to quantify the vertical inhomogeneity of $\epsilon_T(\boldsymbol{x}, t)$ more precisely, we decompose the thermal dissipation rate field into contributions which result from the mean temperature profile and the temperature fluctuations. With Eqn. (1.22) and the decomposition in Eqn. (3.2), it follows

$$\epsilon_T(\boldsymbol{x}, t) = \kappa \left[\left(\frac{\partial \langle T \rangle_A}{\partial z} \right)^2 + 2 \frac{\partial \langle T \rangle_A}{\partial z} \frac{\partial \theta}{\partial z} + (\boldsymbol{\nabla} \theta)^2 \right] , \tag{4.1}$$

$$= \epsilon_{\langle T \rangle}(z) + 2\kappa \frac{\partial \langle T \rangle_A}{\partial z} \frac{\partial \theta}{\partial z} + \epsilon_\theta(\boldsymbol{x}, t) \tag{4.2}$$

The mixed term vanishes after averaging over planes at fixed height z and thus

$$\langle \epsilon_T \rangle_A(z) = \epsilon_{\langle T \rangle}(z) + \langle \epsilon_\theta \rangle_A(z) . \tag{4.3}$$

Figure 4.3 plots the vertical profiles of both contributions to the total thermal dissipation rate for Rayleigh numbers $Ra = 10^7$ (Figures 4.3a,c) and 10^9 (Figures 4.3b,d). All values on the horizontal axis are given in units of the corresponding ensemble mean, $\langle \epsilon_T \rangle_V = Nu/\sqrt{RaPr}$ (see also Eqn. (1.21)). The contribution of the mean temperature profile, $\epsilon_{\langle T \rangle}$, is dominant in the thermal boundary layer and decreases rapidly to almost zero toward the cell center (see Figures 4.3a,b). This mean profile contribution increases with increasing Rayleigh number since the scale across which the significant temperature variation occurs – i.e., the thermal boundary layer thickness δ_T – becomes smaller. Conversely, the thermal dissipation rate due to the temperature fluctuations is dominant in the bulk and exceeds the mean profile contribution by more than 3 orders of magnitude (not shown here). As displayed in Figures 4.3(c,d) for both Rayleigh numbers, the total dissipation remains significantly below $Nu/\sqrt{RaPr}$ in the bulk.

From the advection-diffusion equation, Eqn. (1.5), we derive a balance equation for the temperature variance. Multiplication of Eqn. (1.5) with T in combination with the decomposition in Eqn. (3.2), and averaging over the horizontal plane at a fixed height leads to

$$\frac{\mathrm{d}\langle \theta^2 \rangle_A}{\mathrm{d}t} = -\langle u_z \theta \rangle_A \frac{\mathrm{d}\langle T \rangle_A}{\mathrm{d}z} - \kappa \langle (\boldsymbol{\nabla} \theta)^2 \rangle_A - \kappa \left(\frac{\mathrm{d}\langle T \rangle_A}{\mathrm{d}z} \right)^2 + \ldots \tag{4.4}$$

We identify the first term on the right-hand side of Eqn. (4.4) as the production term, $P_T(z)$, the second as the thermal dissipation due to temperature fluctuations,
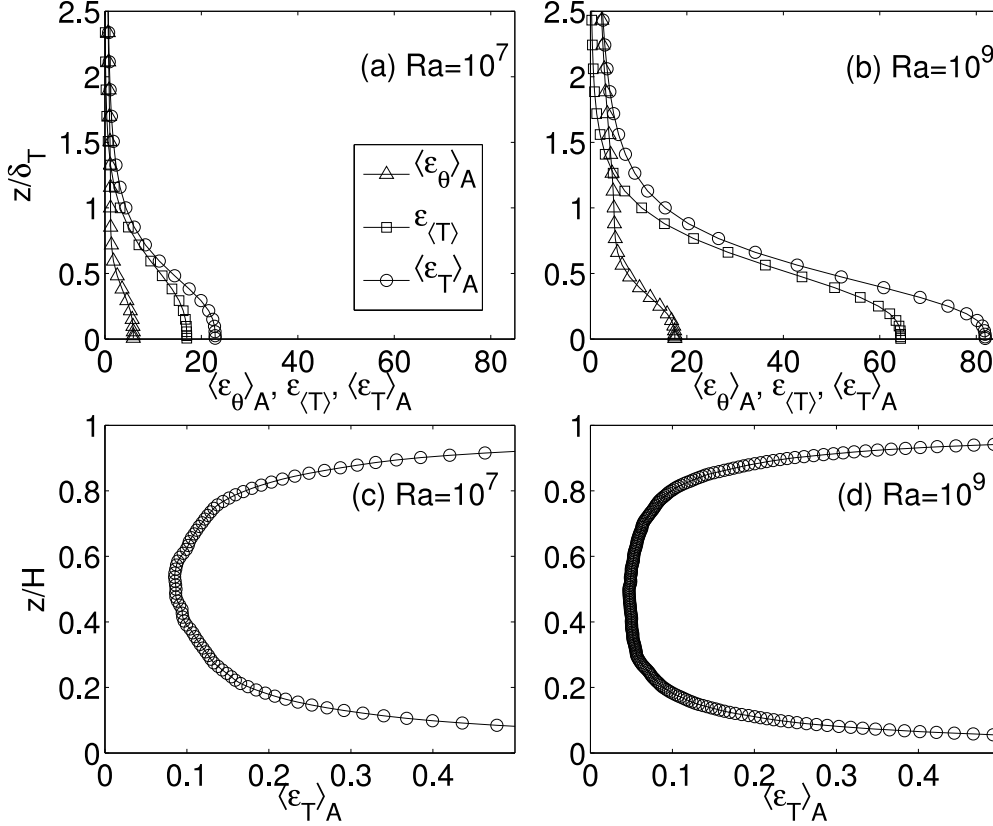
Figure 4.3: Vertical profiles of the two contributions to the total thermal dissipation rate which follow from the mean temperature and the temperature fluctuations (see Eqn. (4.2)). Data points are for Rayleigh number $Ra = 10^7$ (a,c) and $Ra = 10^9$ (b,d). The terms on the horizontal axis are normalized by the ensemble average of the total dissipation rate $\langle\epsilon_T\rangle_V = Nu/\sqrt{RaPr}$ (see Eqn. (1.21)). In (c,d), the vertical profiles of the total thermal dissipation rate are replotted in order to demonstrate that they decrease significantly below the global quantity $\langle\epsilon_T\rangle_V$.

$\langle\epsilon_\theta\rangle_A(z)$, and the third one as the thermal dissipation due to the mean temperature profile, $\epsilon_{\langle T\rangle}(z)$. The remaining flux terms are not shown here. Both dissipation rates sum up to the total dissipation $\langle\epsilon_T\rangle_A(z)$ (see Eqn. 4.3). Figure 4.4a plots the vertical profiles of the four above mentioned terms. The term $\epsilon_{\langle T\rangle}(z)$ dominates inside the boundary layer, while the contribution due to fluctuations, $\langle\epsilon_\theta\rangle_A(z)$, is dominant in the bulk as shown in Figure 4.3 also. It can be seen that the production is maximum close to $\delta_T = 1$. The ratio $P_T(z)/\langle\epsilon_T\rangle_A(z) > 1$ for $\delta_T \leq z \leq 5\delta_T$ (Figure 4.4b), which means that in this region a significant fraction of the temperature variance is injected into the system. This production dominated region above the boundary layer can be regarded as the plume mixing zone. Now, consider the mixing zone length as l_m (Figure 4.4b). We obtain a power law relation $l_m = 0.5 \times Ra^{-0.15}$ for five Rayleigh numbers, namely $Ra=\{1 \times 10^7, 5 \times 10^7, 1 \times 10^8, 5 \times 10^8$ and $1 \times 10^9\}$ with a fixed aspect ratio $\Gamma = 1$. It shows that l_m here is of the same order
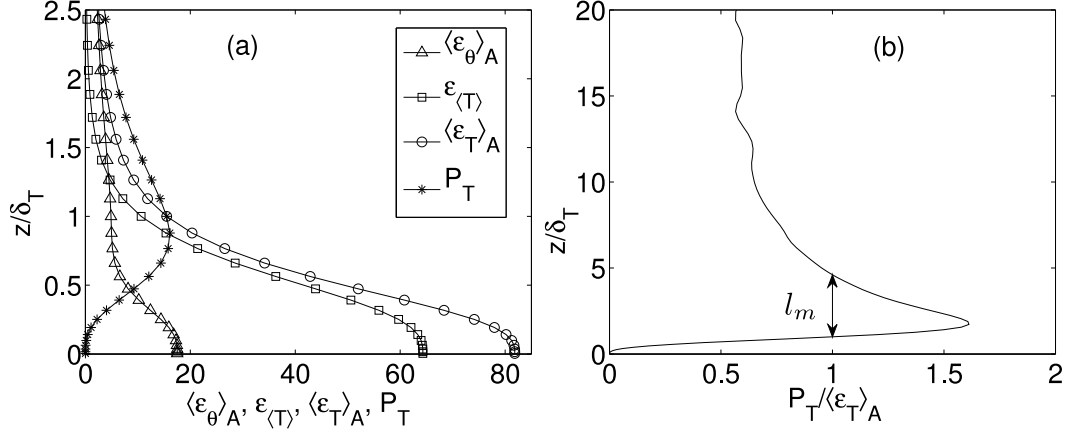
Figure 4.4: Height-dependent profiles of the turbulent production of temperature variance, $P_T(z)$, contributions to the total thermal dissipation rate, $\langle\epsilon_T\rangle_A(z)$, due to temperature fluctuations, $\langle\epsilon_\theta\rangle_A(z)$, and the mean temperature profile, $\epsilon_{\langle T\rangle}(z)$ are plotted in (a) (see Eqn. (4.4)). The height is given in units of the thermal boundary layer thickness $\delta_T = H/(2Nu)$. The terms on the horizontal axis are normalized with respect to the global quantity $\langle\epsilon_T\rangle_V = Nu/\sqrt{RaPr}$ (see Eqn. (1.21)). In plot (b), the ratio of the production to the total thermal dissipation rate is shown. The plume mixing zone length l_m is defined as the thickness above δ_T, for which $P_T/\langle\epsilon_T\rangle_A > 1$. The analysis is conducted for $\Gamma = 1$ and $Ra = 10^9$.

of magnitude as the one reported by Procaccia *et al.* (1991) ($l_m = 2 \times Ra^{-0.143}$) and Zhou & Xia (2002) ($l_m \sim Ra^{-0.13}$). In the former case, l_m is estimated from the scaling argument and, therefore, the prefactor is different from ours. In the later case, l_m is calculated from the height-dependent profiles of the temperature derivative skewness for the experiments conducted in a cylindrical cell filled with water.

4.3 Scaling relations

From Eqn. (1.21) and the scaling relation $Nu \sim Ra^\beta$, the Rayleigh-number dependence of the ensemble average $\langle\epsilon_T\rangle_V$ yields

$$\langle\epsilon_T\rangle_V \sim Ra^{\beta - \frac{1}{2}} = Ra^\gamma, \qquad (4.5)$$

which gives an exponent $\gamma = -0.217$ in our simulations as shown in Figure 4.5 for the data set $Ra=\{5 \times 10^6, 10^7, 5 \times 10^7, 10^8, 5 \times 10^8, 10^9\}$ and $\Gamma = 1$.

Grossmann & Lohse (2000) decomposed the mean dissipation rate into the boundary layer contribution, $\langle\epsilon_T\rangle_{BL}$, and the bulk contribution, $\langle\epsilon_T\rangle_{Bulk}$, as

$$\langle\epsilon_T\rangle = \langle\epsilon_T\rangle_{BL} + \langle\epsilon_T\rangle_{Bulk}, \qquad (4.6)$$
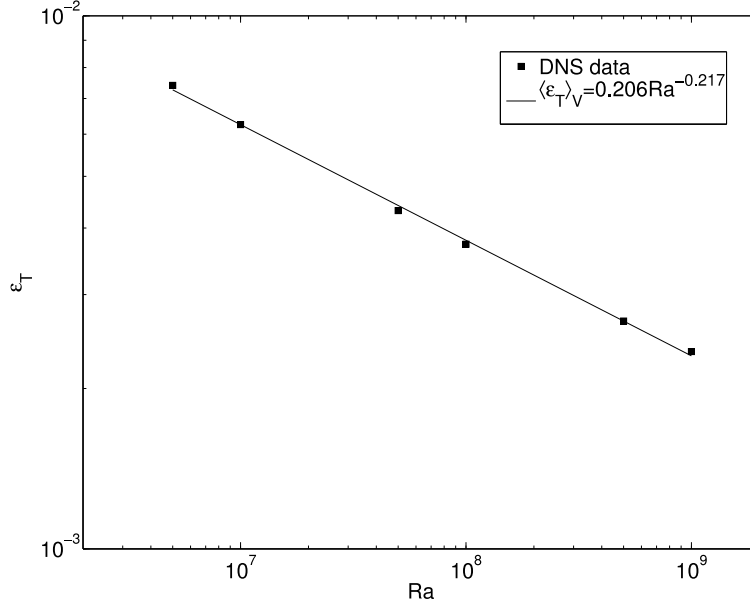
Figure 4.5: Volume-averaged thermal dissipation rate, $\langle \epsilon_T \rangle_V$, as a function of Ra for the data set $Ra = \{5 \times 10^6, 10^7, 5 \times 10^7, 10^8, 5 \times 10^8, 10^9\}$ and $\Gamma = 1$. The DNS data points follow the scaling $\langle \epsilon_T \rangle_V = 0.206 Ra^{-0.217}$.

with the scaling relations

$$
\begin{aligned}
\langle \epsilon_T \rangle_{BL} &\sim Ra^{\beta}, \\
\langle \epsilon_T \rangle_{Bulk} &\sim Ra^{\zeta}.
\end{aligned}
\tag{4.7}
$$

The exponent ζ follows from a scaling of the Reynolds number with respect to the Rayleigh number, $Re \sim Ra^{\zeta}$, and is found between 0.43 and 0.49 (Ahlers *et al.* 2009). The boundary layer contribution in Eqn. (4.7) follows from the assumption of a power law $Nu \sim Ra^{\beta}$ for the turbulent heat transfer. The exponent β is found between 2/7 and 1/3 (Ahlers *et al.* 2009). In our studies, we exclude the dependence on the Prandtl number and consider only a fixed value of $Pr = 0.7$.

Following the GL theory (Grossmann & Lohse 2000), we define different subvolumes, bulk and boundary layer (BL) regions, in the cylindrical cell. The corresponding mean thermal dissipation rates are given by

$$
\langle \epsilon_T \rangle_{Bulk} = \kappa \left\langle \left(\frac{\partial T}{\partial x_i} \right)^2 \right\rangle_{Bulk} \quad \text{for} \quad x_i = (x, y, 0.4 \leq z \leq 0.6).
\tag{4.8}
$$

$$
\langle \epsilon_T \rangle_{BL} = \kappa \left\langle \left(\frac{\partial T}{\partial x_i} \right)^2 \right\rangle_{BL} \quad \text{for} \quad x_i = (x, y, z \leq \delta_T).
\tag{4.9}
$$

In line with the definitions of averaging in section 2.5, we combine again an average over many realizations of turbulent fields and a volume average which is taken now over the subvolumes, BL and $Bulk$, as defined in Eqns. (4.8) and (4.9), respectively.

4.3.1 Scaling in the boundary layer

From the GL theory (cf. Eqn. (2.15) in Grossmann & Lohse 2000), one can estimate the thermal dissipation in the thermal boundary layer by assuming that it is due to the mean temperature drop across δ_T only and that $\langle \epsilon_T \rangle_{BL} \approx \epsilon_{\langle T \rangle}$, which gives

$$\langle \epsilon_T \rangle_{BL} \approx \kappa \left(\frac{\Delta T}{2\delta_T} \right)^2 \frac{\delta_T}{H} \sim \kappa \left(\frac{\Delta T}{H} \right)^2 Nu \sim Ra^\beta . \qquad (4.10)$$

The factor δ_T/H stands for the fraction of the total volume which is occupied by the boundary layer. The last relation in Eqn. (4.10) holds if κ is a constant. For Rayleigh numbers between 5×10^7 and 10^9, our DNS data set gives a scaling with respect to Rayleigh number as

$$\langle \epsilon_T \rangle_{BL} \approx 0.016 \times Ra^{0.10} . \qquad (4.11)$$

This exponent is significantly smaller than those predicted by the scaling theories, $\beta = 2/7$ or $1/3$ and even a larger exponent of 0.63 was found in the experiments by He et $al.$ (2007) and He & Tong (2009). The discrepancies between our findings and He et $al.$ results could be due to the fact that their data points are taken at several points across a vertical line inside the thermal boundary layer, while we have averaged the thermal dissipation rate over the volume fraction as in Eqn. (4.9). Their experiments were conducted for different values of Pr than ours. Moreover, in experiments, it is not possible to achieve the same level of spatial resolution in the boundary layer as in DNS. The estimation given in Eqn. (4.10) does not consider all of the boundary layer dynamics, e.g. significant contribution of $\langle \epsilon_\theta \rangle_{BL}$ as seen in Figure 4.3. In addition, we have found that $\langle \epsilon_\theta \rangle_{BL}$ has almost the same scaling with Rayleigh number as $\langle \epsilon_T \rangle_{BL}$ in our DNS simulations.

4.3.2 Scaling in the bulk

In the bulk of the cylindrical cell, the thermal dissipation rate is due to temperature fluctuations only (cf. Figure 4.3), which can be estimated with the help of Eqn. (2.12) in Grossmann & Lohse (2000) as

$$\langle \epsilon_T \rangle_{Bulk} \approx \langle \epsilon_\theta \rangle_{Bulk} \sim \frac{U(\Delta T)^2}{H} = \kappa \frac{(\Delta T)^2}{H^2} RePr , \qquad (4.12)$$

It requires the knowledge of $Re(Ra, Pr)$ in order to get the full insight. The power law $Re \sim Ra^\zeta$ gives a range of exponents between $\zeta = 0.43$ and 0.49 (Brown et $al.$ 2007; Ahlers et $al.$ 2009). This variation in ζ is due to a particular choice of the definition of Reynolds number , e.g. Re based on the characteristic velocity. It follows thus from Eqn. (4.12) that

$$\langle \epsilon_T \rangle_{Bulk} \sim Ra^\zeta , \qquad (4.13)$$

for a fixed Prandtl number with an exponent $\zeta > 0$. However, our DNS simulations for the data set $Ra=\{5 \times 10^6,\ 10^7,\ 5 \times 10^7,\ 10^8,\ 5 \times 10^8,\ 10^9\}$ and $\Gamma = 1$ give a negative exponent for ζ as

$$\langle \epsilon_T \rangle_{Bulk} \approx 0.32 \times Ra^{-0.38}\,, \tag{4.14}$$

in the bulk sub-volume, which comes close to the experimental findings by He *et al.* (2007) and He & Tong (2009) and follows also the observed trend of Verzicco & Camussi (2003). This trend ($\zeta < 0$) does not alter even if the bulk volume fraction is increased in the analysis. For example, an exponent $\zeta = -0.34$ in Eqn. (4.14) was obtained for $0.2 \leq z \leq 0.8$. We conclude that the scaling exponent, which is rather robust with respect to changes of the volume fraction, has the opposite sign compared to the one reported by Grossmann & Lohse (2000). The reason for this discrepancy could be that the dimensionally correct ansatz $U(\Delta T)^2/H$ may not be appropriate for the thermal dissipation rate. Similar to fluid turbulence, the Rayleigh numbers and, therefore, the Reynolds numbers are still too small to reach the regime in which the thermal dissipation rate given in units of $U(\Delta T)^2/H$ is a constant. This is known as the dissipation anomaly (Donzis *et al.* 2005). Both $\langle \epsilon_T \rangle_{Bulk}/(U_{rms}T_{rms}^2/H)$ and $\langle \epsilon_T \rangle_{Bulk}/(U_{rms}\Delta T^2/H)$ still decrease with increasing Ra for our data set, with U_{rms} is defined in Eqn. (3.4).

4.3.3 Scaling based on plume and background dominated mean dissipation rate

Later, Grossmann & Lohse (2004) refined their concept based on differences in the Rayleigh-number-dependence of the mean thermal dissipation, which were reported in DNS studies by Verzicco & Camussi (2003). The decomposition of the mean thermal dissipation rate, $\langle \epsilon_T \rangle$, into a plume-dominated part, $\langle \epsilon_T \rangle_{pl}$, and a turbulent background contribution, $\langle \epsilon_T \rangle_{bg}$, gives the following power laws

$$\begin{aligned}
\langle \epsilon_T \rangle_{pl} &\sim& Ra^{\zeta/2}\,, \\
\langle \epsilon_T \rangle_{bg} &\sim& Ra^{\zeta}\,.
\end{aligned} \tag{4.15}$$

In both cases, Eqns. (4.7) and (4.15), the plume (or boundary layer) and background (or bulk) fractions are increasing functions with respect to Rayleigh number. Motivated by this approach and the discrepancies in the original GL theory (Grossmann & Lohse 2000), we propose the following definitions of the plume-dominated sub-volume, V_{pl}, and the background contribution sub-volume, V_{bg}, in the convection cell as

$$V_{pl} = \{\boldsymbol{x} \in V\ :\ u_z\theta > 0\}\,. \tag{4.16}$$

$$V_{bg} = V \setminus V_{pl} = \{\boldsymbol{x} \in V\ :\ u_z\theta \leq 0\}\,. \tag{4.17}$$

The corresponding mean thermal dissipation rates in those sub-volumes, as given by Eqns. (4.16) and (4.17), are $\langle \epsilon_T \rangle_{pl}$ and $\langle \epsilon_T \rangle_{bg}$, respectively. This means that the dissipation rates are conditioned with respect to the quantity $u_z\theta$.

(a) Temperature plot in rz plane at $\phi = 0 - \pi$ (b) $u_z\theta > 0$ in rz plane at $\phi = 0 - \pi$
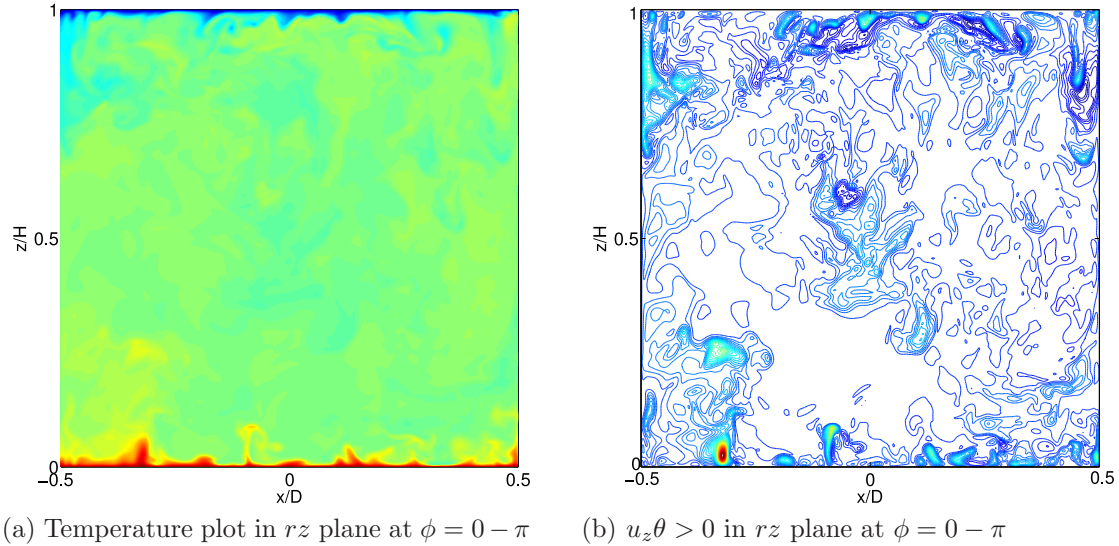
Figure 4.6: 2D contour plots of instantaneous snapshots for $Ra = 10^9$ and $\Gamma = 1$. Contour (a) is the total temperature field with red color represents the hot plumes and blue color the cold plumes. Contour (b) plots $u_z\theta > 0$, which separates plumes (hot or cold) according to the intensity of colors as highlighted by red and blue.
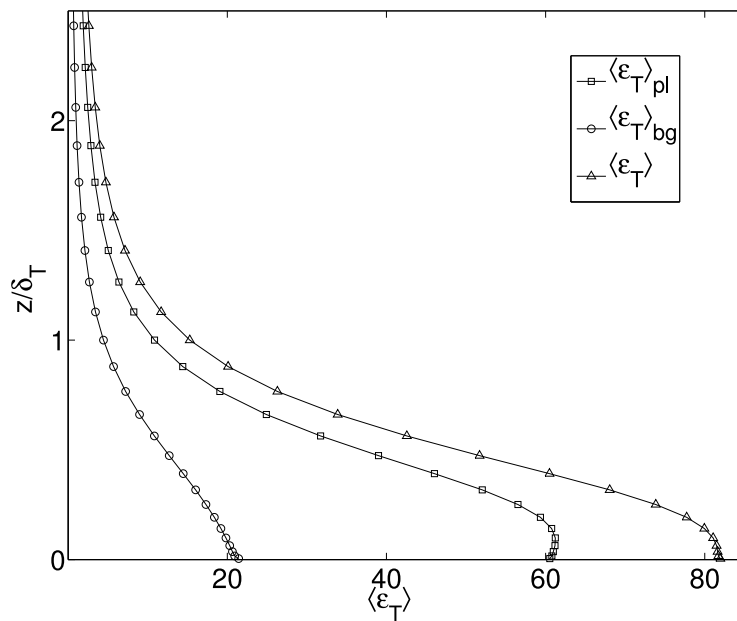
Figure 4.7: Plumes and background contributions to the total thermal dissipation rate $\langle \epsilon_T \rangle_A$. The simulation is conducted for $Ra = 10^9$ in a cell with aspect ratio $\Gamma = 1$. Averages are taken in planes at fixed height z for a sample of statistically independent snapshots. The data on the horizontal axis is normalized with respect to the global quantity $\langle \epsilon_T \rangle_V = Nu/\sqrt{RaPr}$.
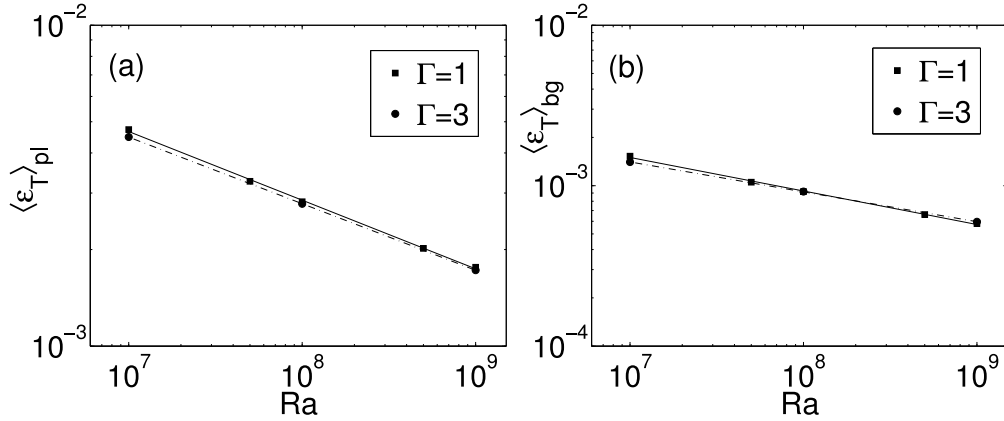
Figure 4.8: (a) plumes and (b) background contributions to the mean thermal dissipation rate as in Eqns. (4.16)-(4.17) are plotted as a function of the Rayleigh number Ra. Two series of simulations are compared, one for the aspect ratio $\Gamma = 1$ and the other for $\Gamma = 3$.

The motivation behind the choice of $u_z\theta$ as a splitting criterion can be explained from Figure 4.6. A plume element is a combination of the vertical upward (or downward) velocity u_z, and positive (or negative) temperature fluctuations θ, with the product $u_z\theta$ is always positive. Based on this splitting criterion, the plume elements in the total temperature field in Figure 4.6a are replicated in $u_z\theta > 0$ contours in Figure 4.6b. This suggests that our separation criterion is justified. Figure 4.7 displays the vertical profiles of $\langle\epsilon_T\rangle_{pl}$ and $\langle\epsilon_T\rangle_{bg}$ as well as the sum of both, $\langle\epsilon_T\rangle$. The plume contribution is about 75% of the total thermal dissipation rate in the thermal boundary layer. The profiles are similar to those plotted in Figure 4.3 for a decomposition shown in Eqn. (4.3). Figure 4.8 plots the dependence of the mean values on the Rayleigh number. We compare two series of simulations at different aspect ratios, $\Gamma = 1$ and 3. We observe slight differences in the means with respect to Γ. The power law fits remain, however, nearly unchanged. The power law fits for our DNS data set for the Rayleigh number range, $Ra = 10^7 - 10^9$, and $\Gamma = 1$ are

$$\langle\epsilon_T\rangle_{pl} = 0.15 \times Ra^{-0.214}, \tag{4.18}$$

$$\langle\epsilon_T\rangle_{bg} = 0.04 \times Ra^{-0.210}, \tag{4.19}$$

which indicate that the exponents are negative and almost the same in magnitude. However, the prefactors differ. Shishkina & Wagner (2008) and Schumacher (2008, 2009) observed that the rising of thermal plumes is connected to strong vorticity, in particular in the detachment zone. Strong gradients of the convecting fluid thus result in strong temperature gradients in the vicinity of plumes. Due to the incompressibility of the working fluid, strong updrafts will cause downdrafts next to it. To summarize, the refined analysis does not change our former findings qualitatively.
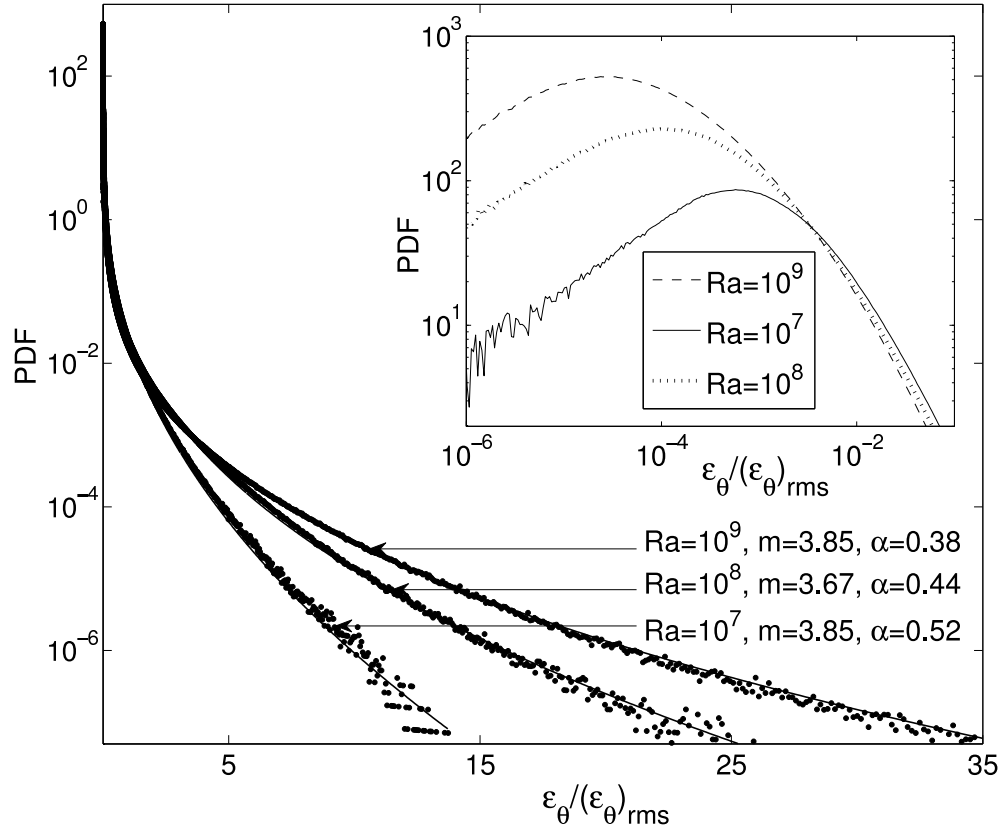
Figure 4.9: Tails of the PDFs of the thermal dissipation rates due to temperature fluctuations, ϵ_θ, in the bulk. Planes with $z \in [4\delta_T, H - 4\delta_T]$ are included. The tails are fitted by stretched exponentials as given by Eqn. (4.20) with the fit coefficients and exponents are indicated in the figure. The inset magnifies the PDFs for the smallest dissipation rate amplitudes in log-log scale. The data points are normalized with respect to the rms value calculated over the whole volume $V = \pi R^2 H$ and a sequence of statistically independent snapshots.

4.4 Stretched exponential behavior in the tails

The mismatch of the Rayleigh number scaling with the predictions by Grossmann & Lohse (2000) suggests that strong fluctuations of the thermal dissipation were not taken into account in their scaling, which is indeed not possible for a scaling theory. We discuss now the statistics of ϵ_θ and show that the extreme events are significant at least in the boundary layer. Figure 4.9 shows the PDF of the dissipation rate due to temperature fluctuations ϵ_θ in the bulk. The analysis is conducted in planes between $z \in [4\delta_T, H-4\delta_T]$. In correspondence with the passive scalar case (Overholt & Pope 1996; Schumacher & Sreenivasan 2005), we fit a stretched exponential to the fraction of the PDF which extends from the most probable amplitude (see the inset of Figure 4.9) to the end of the tail. We define $X = \epsilon_\theta/\langle\epsilon_\theta\rangle_V$ and $X^* = X - X_{mp}$,

with X_{mp} is the abscissa of the most probable (mp) value. Data points are fitted to

$$p(X^*) = \frac{C}{\sqrt{X^*}} \exp\left(-mX^{*\alpha}\right) .$$ (4.20)

Similar to the passive scalar case, we do observe fatter tails with increasing
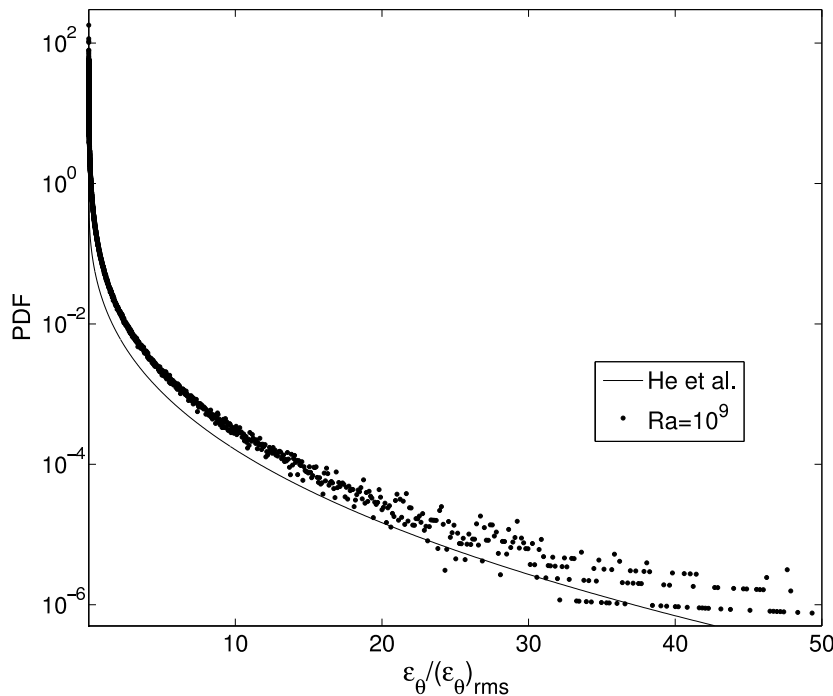
Figure 4.10: PDFs of ϵ_θ at the center plane $(z = 0.5H)$ normalized with respect to $(\epsilon_\theta)_{rms}$, which is also taken at $z = 0.5H$ for the area $A = \pi R^2$. Our DNS data set for $Ra = 10^9$ is compared with the experimental results (FIG. 4) of He *et al.* (2007) for $Ra = 9.6 \times 10^8$ and $Pr = 5.4$. The statistics are gathered again over a sequence of statistically independent snapshots. Data points are more scattered in the far tail compared to Figure 4.9 because here only a single plane is included in the analysis as opposed to the bulk volume there.

Rayleigh number (and therefore with increasing Reynolds number). This is in line with an increasing degree of small-scale intermittency of the thermal dissipation rate field. Overholt & Pope (1996) and Schumacher & Sreenivasan (2005) have conducted a similar analysis for the passive scalar dissipation rate in a homogeneous isotropic turbulent flow. There, a minimal exponent $\alpha = 1/3$ can be derived analytically in the limit of a very large Peclét number. The scalar is then advected in a flow which is white in time (Chertkov *et al.* 1998; Gamba & Kolokolov 1999). The advection of a passive scalar in a Navier-Stokes flow resulted in tails that were sparser, i.e. $\alpha \geq 1/3$ (Yeung *et al.* 2005). Our present analysis indicates that this threshold is also approached to the hard-turbulence regime of convection.
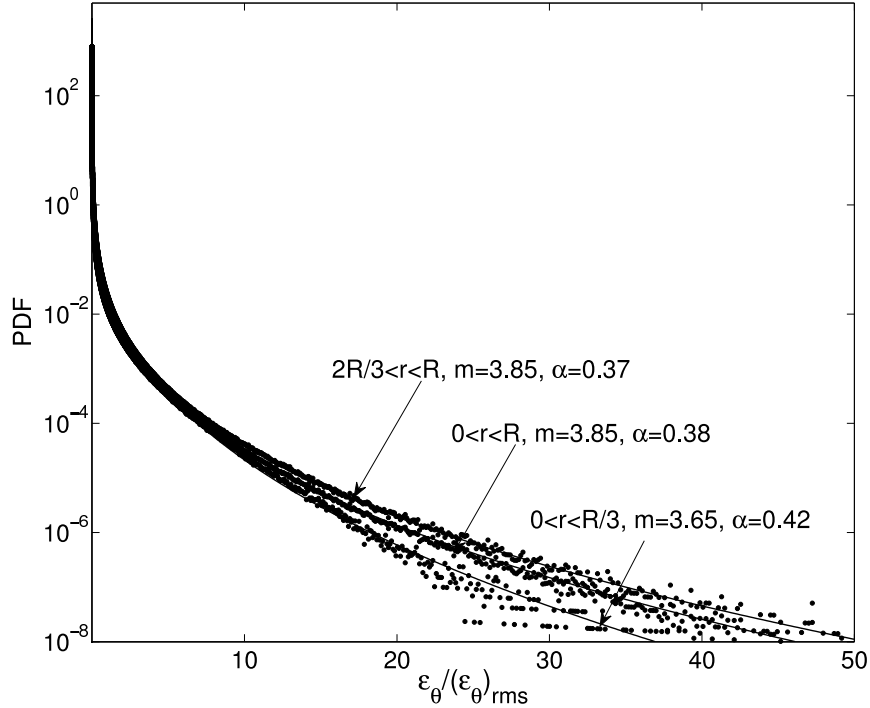
Figure 4.11: Tails of the PDFs of ϵ_θ in the bulk ($z \in [4\delta_T, H - 4\delta_T]$) for three cases, namely the whole bulk ($0 < r < R$, middle curve, see also Figure 4.9), the center zone ($R/3 < r < R$, bottom curve) and close to the sidewalls ($2R/3 < r < R$, top curve). The analysis is conducted for the simulation at $Ra = 10^9$ and $\Gamma = 1$. The PDF is normalized by the corresponding rms value. The rms value is obtained for the whole volume, $V = \pi R^2 H$, and a sequence of statistically independent realizations of turbulent fields.

Figure 4.10 replots our data in the center plane for $Ra = 10^9$ in units of the rms value of thermal dissipation $(\epsilon_\theta)_{rms}$ in order to compare them with those obtained by He *et al.* (2007). A slightly sparser tail in their experiments was observed. The reason for the difference between both cases might be due to the improved resolution of the temperature gradient in our simulations, which was not possible in the experiment, as mentioned before. Moreover, the Prandtl number ($Pr = 5.4$) was almost an order of magnitude larger in the experiment. An increasing Prandtl number reduces the thermal boundary layer thickness and might cause less plume mixing in the bulk. Less pronounced plumes will cause smaller amplitudes of the thermal dissipation. Such a trend with the Prandtl number would differ from passive scalar turbulence, where the tails of the PDF of ϵ_θ become fatter with increasing Prandtl (or Schmidt) number for a given Reynolds number of the advecting flow (Schumacher & Sreenivasan 2005). There a less diffusive scalar field generates sharper gradients. It remains open which of those two effects is more dominant. Further studies are required to understand the dependence of the temperature gradient statistics on the Prandtl number in thermal convection.
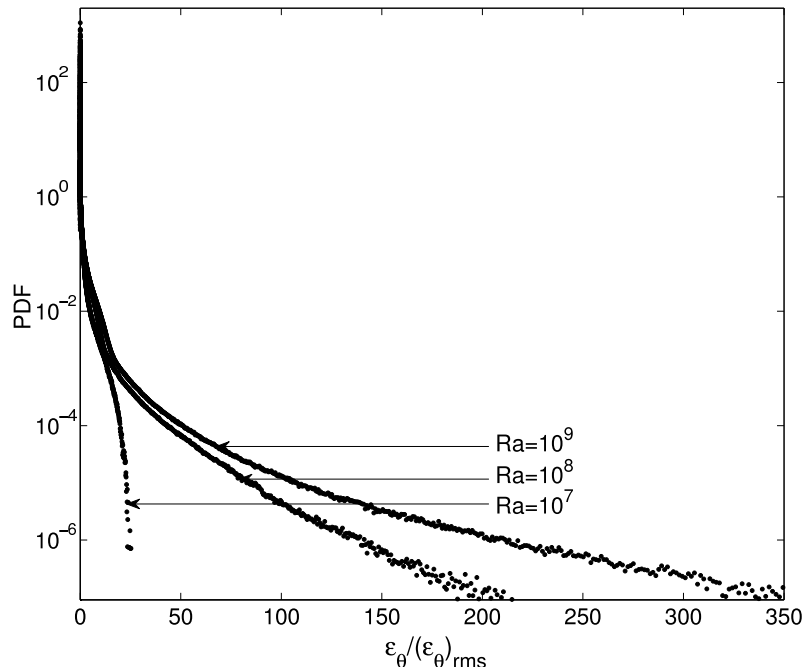
Figure 4.12: Tails of the PDFs of ϵ_θ close to the bottom plate ($z \in [0, 4\delta_T]$) for different Ra. The data points are normalized with respect to the rms value calculated over the cell volume $V = \pi R^2 H$ and a sequence of statistically independent snapshots.

We also investigate how the statistics of the thermal dissipation rate field is affected by the averaging volume. We have selected two concentric cylinders in the bulk ($z \in [4\delta_T, H - 4\delta_T]$) for this purpose. One is in the center region ($0 < r < R/3$) and the other is in the outer region close to the sidewalls ($2R/3 < r < R$). We present the PDFs of ϵ_θ in these sub-volumes in Figure 4.11 for the simulation at $Ra = 10^9$ and $\Gamma = 1$. The tail of the PDF in the sidewall region is more extended compared to that in the center zone. This implies that the flow in the sidewall region is more intermittent than in the center. This increasing degree of intermittency can be attributed to the large-scale circulation (LSC), which is dominant near the sidewalls and the plumes, which are carried by the mean flow along the LSC. In this region, a destabilizing mean temperature gradient is detected as explained earlier in Figure 3.2 (see also Brown & Ahlers 2007). We will discuss the LSC in more details later in chapter 5.

When repeating the analysis for the part of the volume ($z \in [0, 4\delta_T]$) that has been excluded before, distributions as shown in Figure 4.12 result. It is observed that the amplitudes of the dissipation rate increase by an order of magnitude for the largest Ra compared to those in the bulk (Figure 4.9). The fatter tails for the boundary layer data are in line with the analysis of the plane averaged vertical profiles (Figure 4.3). The fluctuations of the thermal dissipation rate increase with increasing Ra.

4.5 Deviations from log-normality

The intermittent nature of the thermal dissipation field leads to deviations from log-normality, as can be seen in Figure 4.13 where the same data set has been studied as in Figure 4.9. In order to highlight the differences in PDFs, we replot the data in linear-linear and linear-logarithmic axes in Figure 4.13a and Figure 4.13b, respectively. It can be seen that neither the core nor both tails of the PDF fit perfectly with the log-normal form. This is similar to the passive scalar mixing. Small-amplitude tails are fatter than the log-normal curve while large-amplitude tails remain sparser (Ferchichi & Tavoularis 2002; Schumacher & Sreenivasan 2005). The trend of the data with Rayleigh numbers between 10^7 and 10^9 suggests a very slow convergence towards the log-normality. The repetition of the analysis in the vicinity of the thermal boundary layers for the same data set as in Figure 4.12, reveals even stronger deviations (see Figure 4.14). For the large-amplitude tail, a bump is observed. A similar feature has been reported by Kaczorowski & Wagner (2007, 2009). Our analysis suggests that this particular feature is due to the boundary layer dynamics. The bump in the distribution remains also when the PDF is analyzed for the whole volume in the cylindrical cell .
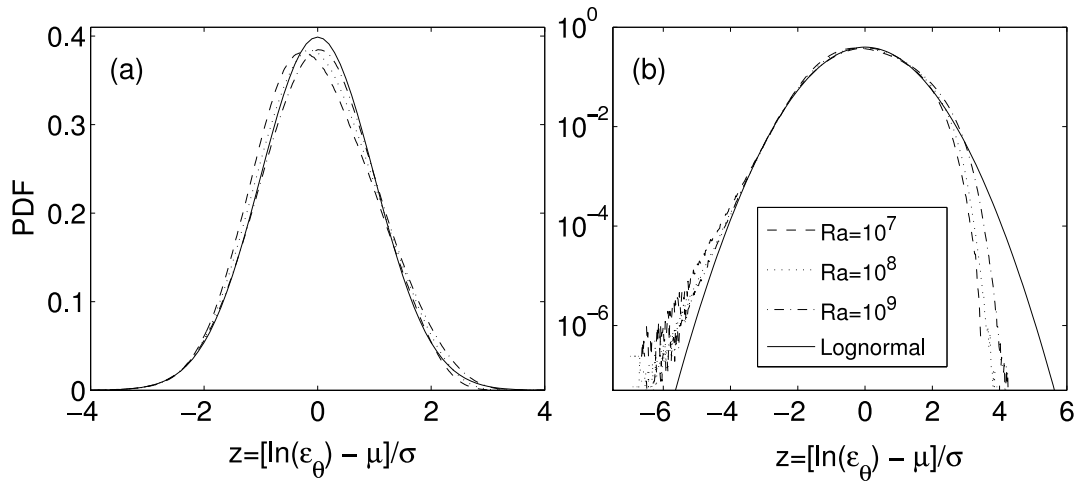
Figure 4.13: Replot of the same data set as for Figure 4.9 in log-normal coordinates. μ is the mean of $\ln(\epsilon_\theta)$ and σ is the corresponding standard deviation. The solid line indicates a log-normal distribution. (a) Linear-linear plot. (b) Linear-logarithmic plot of the same data. Rayleigh numbers are given in the legend.
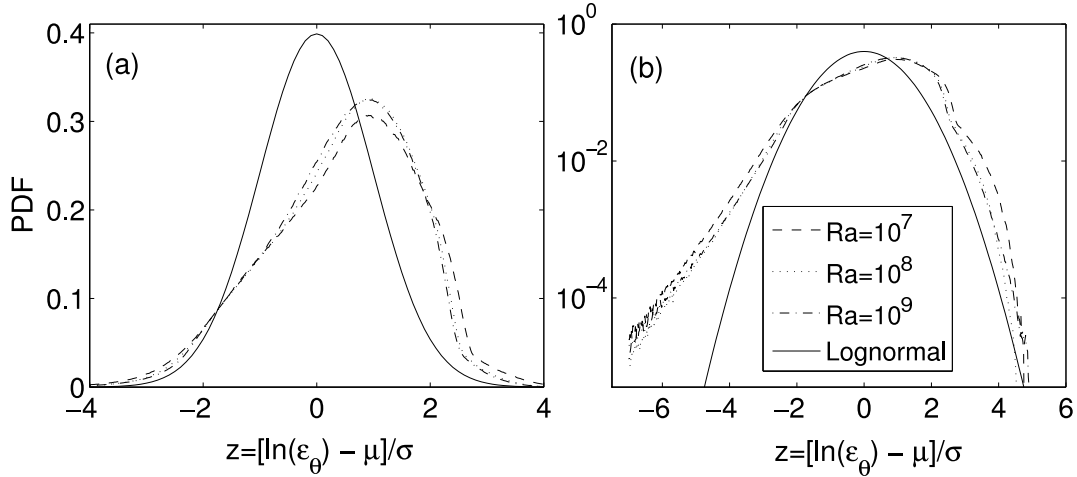
Figure 4.14: Replot of the same data set as for Figure 4.12 in log-normal coordinates. Line and symbol styles are the same as in Figure 4.13.
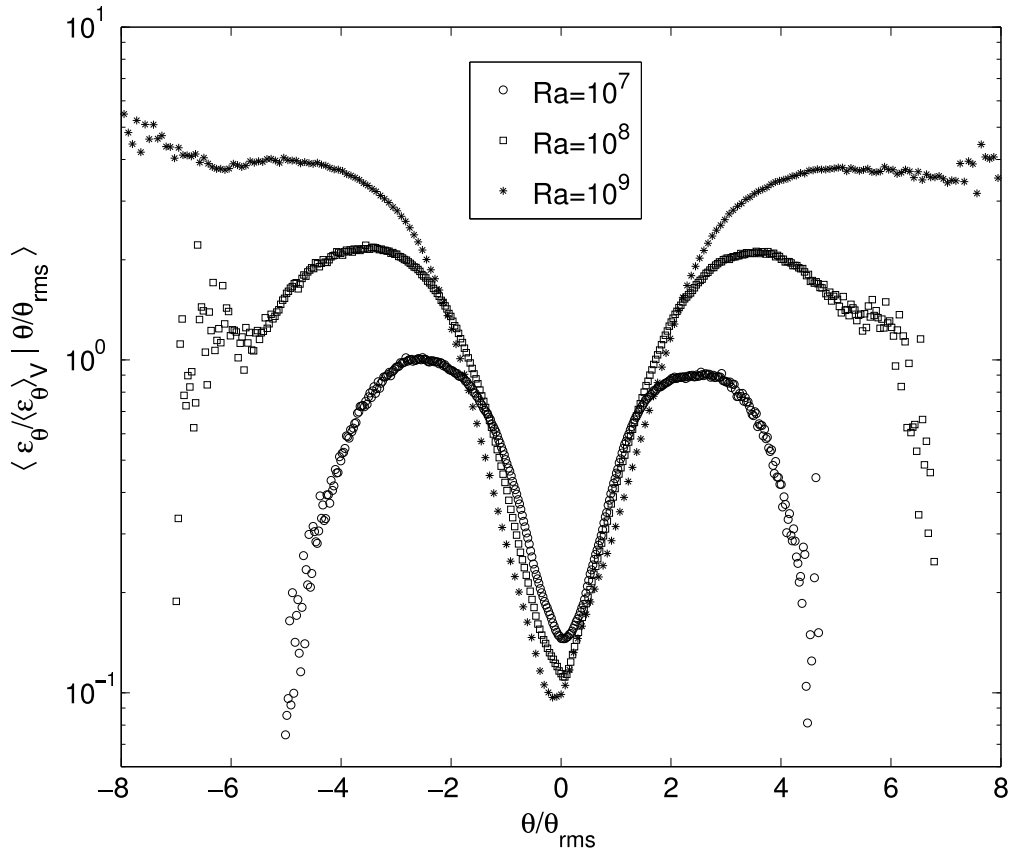
Figure 4.15: Conditional mean dissipation in the bulk ($z \in [4\delta_T, H - 4\delta_T]$) as a function of the Rayleigh number. The rms of θ has been taken over the whole volume, $V = \pi R^2 H$, and for a sequence of statistically independent snapshots.

4.5.1 Conditional mean thermal dissipation

Deviations from the Gaussian distributions of the temperature fluctuation are also manifested in the conditional mean thermal dissipation. It is known that a conditional mean scalar dissipation is constant for a Gaussian scalar field, i.e. independent with respect to the scalar amplitude (e.g. Overholt & Pope 1996). The mean is defined as

$$\langle \epsilon_\theta | \theta(\mathbf{x}, t) = \psi \rangle = \int_0^\infty \mathrm{d}\epsilon_\theta \, \epsilon_\theta \, \frac{p(\epsilon_\theta, \theta(\mathbf{x}, t) = \psi)}{p(\theta(\mathbf{x}, t) = \psi)} \,, \tag{4.21}$$

where $p(\epsilon_\theta, \theta)$ is the joint PDF of the thermal dissipation rate and the temperature fluctuation. Figure 4.15 displays clearly the V-shape for the conditional mean for the temperature fluctuations values around $\theta/\theta_{rms} = 0$. This is consistent with the deviations from Gaussianity, which were observed for the distributions of the temperature field in Figure 3.5. At larger magnitudes of θ, the graphs reach a maximum before decreasing to zero since the support of the joint PDF and the temperature PDF is bounded. The V-shape is more pronounced with increasing Rayleigh number which is due to the higher thermal dissipation amplitudes observable in the flow (see Figure 4.9). Our results agree with the findings of Jayesh & Warhaft (1992).

5 Aspect ratio dependence

In this chapter we study the aspect ratio dependence of heat transfer with corresponding changes in the large-scale circulation (LSC) patterns in the convection cell. Since there are not many systematic investigations on the aspect ratio dependence of heat transfer, we intend to explore more details in this regard, in particular to establish an explicit scaling relation $Nu(\Gamma, Ra)$ for a certain range of parameters. We have selected an aspect ratio range, $\Gamma = 0.5 - 12$, and a Rayleigh number range, $Ra = 10^7 - 10^9$, for this purpose. The simulations are conducted at a fixed Rayleigh number Ra by varying the aspect ratio Γ of the cylindrical geometry. The Prandtl number, $Pr = 0.7$, remains constant for all cases. In the beginning, we discuss the changes in the vertical convective flux and temperature profiles due to the aspect ratio variation. In section 5.2, we provide the scaling relation $Nu(Ra, \Gamma) = A(\Gamma) Ra^{\beta(\Gamma)}$ for several aspect ratios. Finally, we analyze the LSC patterns in fully turbulent fields and compare with those in the moderately nonlinear regime right above the onset of convection in section 5.3.

5.1 Profiles of the vertical convective flux and temperature

The vertical convective flux as well as the vertical gradient of the temperature are responsible for the net heat transfer in convection as can be seen in Eqn. (1.10). The plots in Figure 5.1 reveal that there are significant changes in $u_z T$ profiles with respect to Γ. Here, the quantity $u_z T$ is averaged over the horizontal plane at fixed height z with an ensemble of at least 150 statistically independent samples separated each other by 1 t/t_f time unit, where t_f is given by Eqn. (2.17). The Rayleigh number is $Ra = 10^7$ in this case. The temperature profiles in Figure 5.2 show that the variations for the flat cells ($\Gamma \geq 1$) are much smaller compared to the slander cell ($\Gamma = 0.5$). In case of the slender cell, a large destabilizing slope $(d \langle T \rangle_A (z)/dz)$ in the mean temperature profile is appeared, since the orientation of the LSC patterns in this case (see Verzicco & Camussi 2003) is different from those in the other cells ($\Gamma \geq 1$, see section 5.3).

The variations in $\langle u_z T \rangle_{A,t} (z)$ and $\langle T \rangle_{A,t} (z)$ profiles contribute to significant changes in the global heat transfer Nu with respect to Γ, which are made clear in the next section (see Table 5.1 and Figure 5.4). Figure 5.3 displays the magnified view of
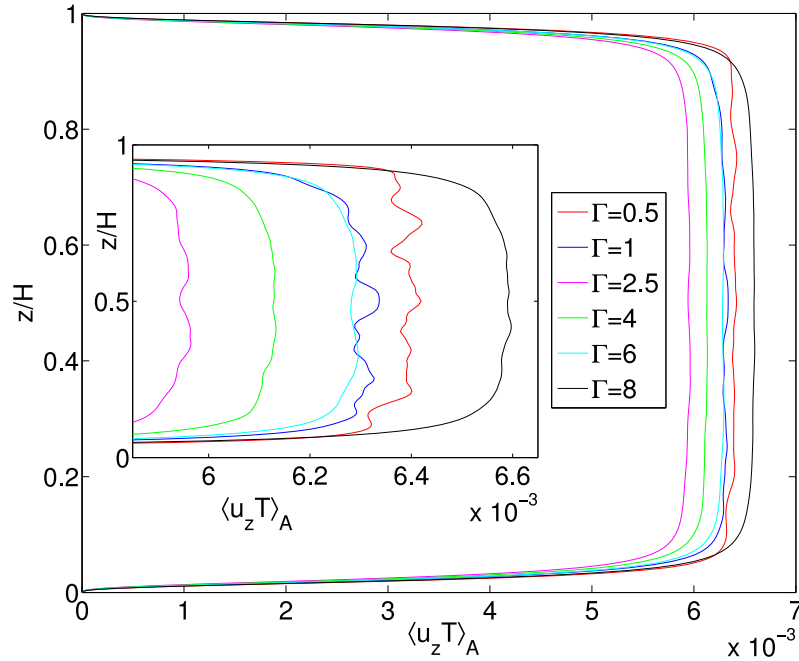
Figure 5.1: The z-dependent mean profiles of u_zT for different aspect ratios at $Ra = 10^7$. The inset shows the magnified view close to the maximum of $\langle u_zT\rangle_A$. Data set for the statistical analysis and the grid points are listed in Table 5.1.
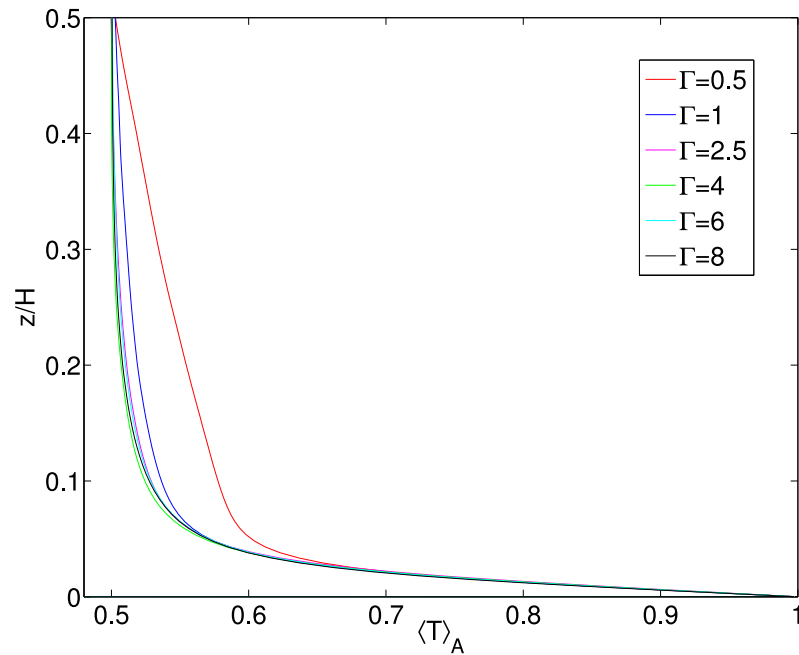
Figure 5.2: The z-dependent mean profiles of the temperature. Due to symmetry, $z/H = 0 - 0.5$ is covered here. Data set is the same as in Figure 5.1.
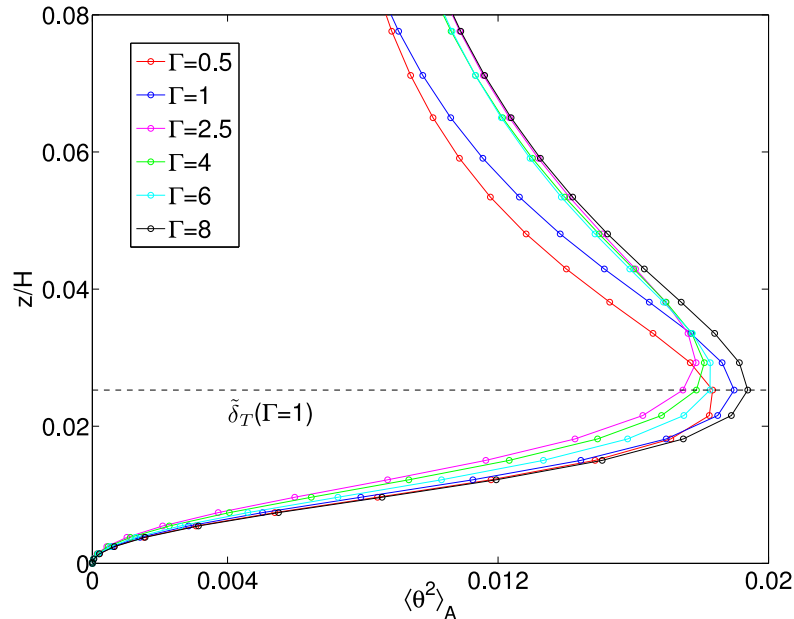
Figure 5.3: Magnified view of the variance temperature fluctuations profiles, $\langle\theta^2\rangle_{A,t}(z)$, close to the bottom plate of the cell. The horizontal dashed line shows the thermal boundary layer thickness $\tilde{\delta}_T$ corresponds to $\Gamma = 1$. This $\tilde{\delta}_T$ slightly differs from $\delta_T = 1/(2Nu)$ as explained in section 3.1. The same data set as in Figure 5.1 is used here.

the variance of temperature fluctuations profiles, $\langle\theta^2\rangle_{A,t}(z)$, close to the bottom boundary layer. The thermal boundary layer thickness $\tilde{\delta}_T$ for $\Gamma = 1$ is marked by the dashed line there and it differs slightly in magnitude (± 1 grid plane) due to aspect ratio variations. We have resolved the thermal boundary layer with at least 14 grid planes in this case.

5.2 Dependence of the global heat transfer on aspect ratio

5.2.1 $Nu(\Gamma)$ at fixed Rayleigh number Ra

We have listed the parameters of our DNS simulations for the aspect ratio studies in Table 5.1. The global Nusselt number Nu is obtained from Eqn. (2.20) and the standard deviation σ of Nu is calculated as in Eqn. (2.21). The total integration time in terms of the convective time unit is $t_c = C_k t/t_f$, where C_k is given in Eqn. (2.19) and Figure 2.4. It shows that the standard deviations are less than or equal to 1% and thus similar to Kerr (1996). The integration time is comparable with van Reeuwijk *et al.* (2008).

$N_\phi \times N_r \times N_z$	Ra	Γ	t/t_f	$Nu \pm \sigma$	σ in %
$97 \times 65 \times 128$	10^7	0.50	300	17.08 ± 0.07	0.4
$193 \times 97 \times 128$	10^7	1.00	150	16.73 ± 0.08	0.5
$217 \times 133 \times 128$	10^7	1.50	111	16.37 ± 0.08	0.5
$217 \times 133 \times 128$	10^7	1.75	151	16.11 ± 0.03	0.2
$217 \times 133 \times 128$	10^7	2.00	250	15.88 ± 0.07	0.4
$217 \times 133 \times 128$	10^7	2.25	251	15.97 ± 0.04	0.2
$257 \times 165 \times 128$	10^7	2.50	251	15.77 ± 0.03	0.1
$257 \times 165 \times 128$	10^7	2.75	251	15.97 ± 0.04	0.3
$257 \times 165 \times 128$	10^7	3.00	150	16.06 ± 0.05	0.3
$301 \times 211 \times 128$	10^7	4.00	150	16.22 ± 0.03	0.2
$385 \times 281 \times 128$	10^7	6.00	150	16.66 ± 0.04	0.2
$401 \times 311 \times 128$	10^7	8.00	150	17.44 ± 0.02	0.1
$513 \times 361 \times 128$	10^7	10.00	150	17.34 ± 0.03	0.2
$601 \times 401 \times 128$	10^7	12.00	150	17.49 ± 0.03	0.2
$151 \times 81 \times 160$	5×10^7	0.50	150	26.20 ± 0.21	0.8
$257 \times 129 \times 160$	5×10^7	1.00	150	25.86 ± 0.13	0.5
$271 \times 151 \times 160$	5×10^7	2.00	149	25.83 ± 0.12	0.5
$401 \times 225 \times 160$	5×10^7	3.00	145	25.90 ± 0.05	0.2
$151 \times 101 \times 256$	10^8	0.50	300	32.06 ± 0.24	0.7
$271 \times 151 \times 256$	10^8	1.00	150	32.21 ± 0.32	1.0
$271 \times 151 \times 256$	10^8	1.25	150	31.77 ± 0.15	0.5
$321 \times 161 \times 256$	10^8	1.50	150	31.39 ± 0.11	0.3
$321 \times 161 \times 256$	10^8	1.75	249	31.57 ± 0.10	0.3
$361 \times 181 \times 256$	10^8	2.00	145	31.25 ± 0.31	1.0
$401 \times 201 \times 256$	10^8	2.25	143	31.25 ± 0.21	0.7
$401 \times 201 \times 256$	10^8	2.50	146	31.87 ± 0.18	0.6
$401 \times 201 \times 256$	10^8	2.75	145	32.34 ± 0.08	0.3
$451 \times 225 \times 256$	10^8	3.00	141	32.29 ± 0.12	0.4
$541 \times 257 \times 256$	10^8	4.00	132	33.20 ± 0.08	0.2
$801 \times 451 \times 256$	10^8	8.00	81	34.78 ± 0.13	0.4
$201 \times 101 \times 310$	10^9	0.50	150	63.67 ± 0.56	0.9
$361 \times 181 \times 310$	10^9	1.00	139	64.31 ± 0.64	1.0
$811 \times 321 \times 310$	10^9	2.00	109	63.25 ± 0.26	0.4
$1025 \times 551 \times 310$	10^9	3.00	110	65.11 ± 0.50	0.8

Table 5.1: Simulation parameters for various Ra and Γ with a fixed $Pr = 0.7$. The convective time unit $t_c = C_k\, t/t_f$ (C_k is given in Eqn. (2.19)). The Nusselt number Nu and the standard deviation σ are calculated from Eqns. (2.20) and (2.21), respectively.
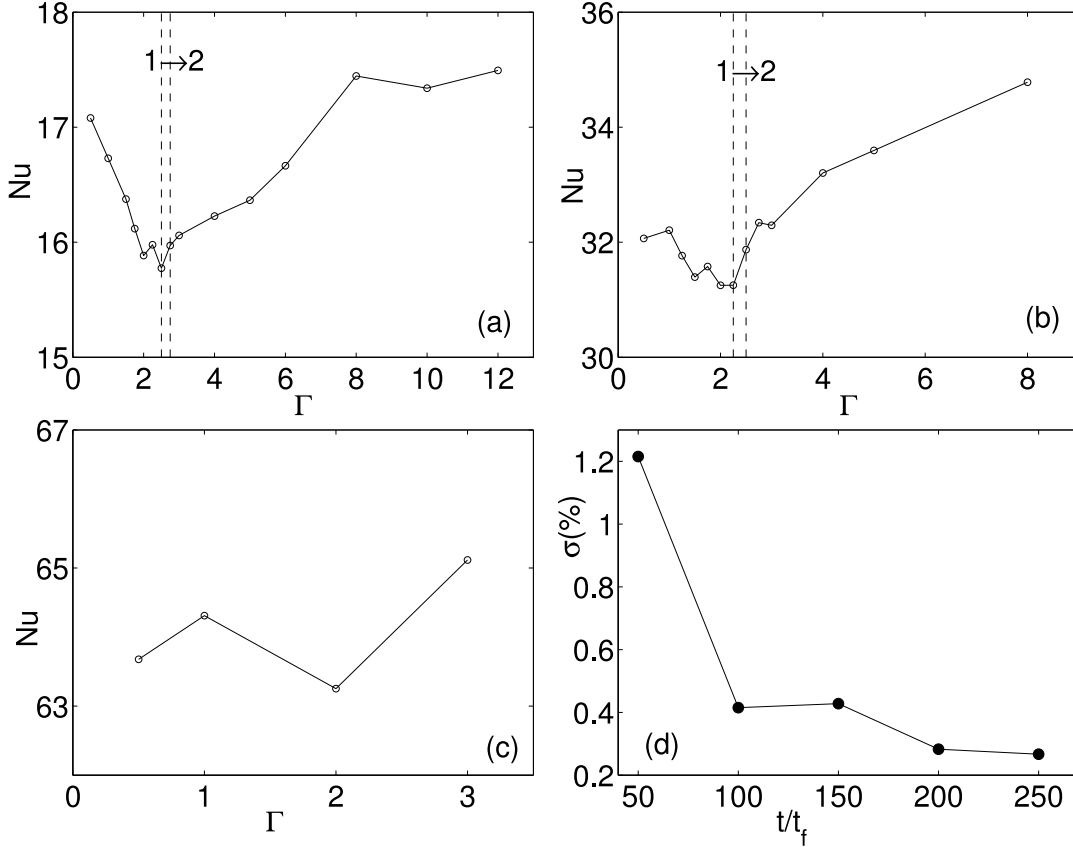
Figure 5.4: Nusselt number Nu as a function of the aspect ratio Γ for (a) $Ra = 10^7$, (b) $Ra = 10^8$, (c) $Ra = 10^9$. The crossover from one circulation roll to two rolls is indicated in (a) and (b) by two parallel dashed lines. For each snapshot, the Nusselt number is determined by volume averaging. In addition, an arithmetic mean is taken over $N_{samp} = t/t_f$ statistically independent turbulent samples (see Eqn. (2.20)). The convective time unit $t_c = C_k t/t_f$ (C_k is given in Eqn. (2.19) and Figure 2.4). The standard deviation σ, which is given by Eqn. (2.21), decreases with increasing number of samples N_{samp} is shown in (d) for the data set $Ra = 10^7$ and $\Gamma = 2$. Simulation parameters for all cases are listed in Table 5.1.

Figure 5.4 shows the Nusselt number Nu as a function of the aspect ratio Γ for three different Rayleigh numbers, namely $Ra = 10^7, 10^8$ and 10^9. At $Ra = 10^7$ (Figure 5.4a), Nu decreases with increasing Γ, attains a minimum value at $\Gamma \approx 2.5$, then increases up to a maximum value close to $\Gamma \approx 8$, and finally saturates for $\Gamma > 8$. Variations in $Nu(\Gamma)$ curve can also be observed in Figures 5.4b and 5.4c for the other two larger Rayleigh numbers. The minimum of $Nu(\Gamma)$ is detected at $\Gamma \approx 2.5$ and $\Gamma \approx 2.25$ for $Ra = 10^7$ and $Ra = 10^8$, respectively. This is the point at which a transition in the LSC from a single-roll to a double-roll pattern occurs (see Figure 5.7). On the basis of stability analysis, Oresta *et al.* (2007) have shown that there is always a single-roll for $\Gamma \leq 2$, irrespective of the initial

conditions, in the weakly nonlinear regime above the onset of convection. However, our Rayleigh numbers here are in fully turbulent regime. With our present computer capability, we could not go beyond $\Gamma > 8$ for $Ra = 10^8$ and $\Gamma > 3$ for $Ra = 10^9$. In particular, for the largest Rayleigh number, we can provide four data points only and, therefore, the minimum of $Nu(\Gamma)$ is inconclusive in this case, although it is apparently at $\Gamma \approx 2$ in Figure 5.4c. On the basis of our simulation data, we can not conclude exactly for which aspect ratio the Nusselt numbers become independent of the cell geometry. However, the trend indicates that it is right above $\Gamma = 8$ for $Ra = 10^7$ and beyond $\Gamma > 8$ for $Ra = 10^8$. The variations in Nu, as defined by the difference between the maximum and minimum in the Nusselt number series, are significant – especially for the lower Rayleigh numbers – and yield 10.9%, 11.3%, and 3.0% for $Ra = 10^7$, 10^8 and 10^9, respectively.

A closer inspection of the three panels in Figure 5.4 reveals non-monotonic graphs of $Nu(\Gamma)$ with local maxima and minima. We have first verified that there is sufficient statistical convergence of the data (see Table 5.1). Since statistical uncertainties can be excluded, there must be some physical reasons for the behavior observed in Figure 5.4. We observe time-averaged flow patterns in turbulent fields which are similar to those at the onset of convection (see Figures 5.7 and 5.8). In this case, an integer number of rolls must fit into the cell in the lower aspect ratio regime. This is the reason why, for example, the linear instability studies by Koschmieder (1969) and Charlson & Sani (1970, 1971) in the cylindrical cells with insulated side-walls yield stability curves $Ra_{cr}(\Gamma)$ with local extrema in the lower Γ regime, and extend to an asymptotic value for larger Γ only. Small discontinuities in $Nu(Ra)$ in the weakly nonlinear regime, which could be traced back to a change in the number of rolls in the cell, have been also reported by Gao *et al.* (1987). These pattern bifurcations can be studied when a small number of degrees of freedom dominates the dynamics. It is not obvious why in a fully turbulent case, where infinitely many degrees of freedom exist, coherent patterns exist and prevail. Similar patterns can, however, be found in a turbulent Taylor vortex flow at high Reynolds number (Lathrop *et al.* 1992).

The Proper Orthogonal Decomposition (POD) analysis by Bailon-Cuba, Emran & Schumacher (2009) has demonstrated that the LSC carries a significant amount of heat through the cell. It was also shown that a change in the LSC morphology causes jumps in the amount of heat transferred by the first few POD modes, e.g. the primary and secondary modes. Those findings strengthen our observation of Γ-dependent heat transfer (Figure 5.4). It should be mentioned that persistent coherent patterns at larger Rayleigh numbers are characterized as a sequence-of-bifurcations to the turbulent state (Busse 2003).

5.2.2 $Nu(Ra)$ at fixed aspect ratio Γ

Systematic experiments with aspect ratios Γ larger than unity were conducted by three groups. First, Wu & Libchaber (1992) detected a power law scaling with Ra, namely

$$Nu(Ra, \Gamma) = A(\Gamma) \times Ra^{\beta} . \tag{5.1}$$

Their measurements indicated almost an unchanged exponent β and an aspect-ratio-dependent prefactor. Second, Sun *et al.* (2005) suggested the following scaling law on the basis of their experiments as

$$Nu(Ra, \Gamma) = A_1(\Gamma) \times Ra^{\beta_1} + A_2(\Gamma) \times Ra^{\beta_2} . \tag{5.2}$$

This scaling is a combination of two power laws with $\beta_1 = 1/3$ and $\beta_2 = 1/5$. Again,
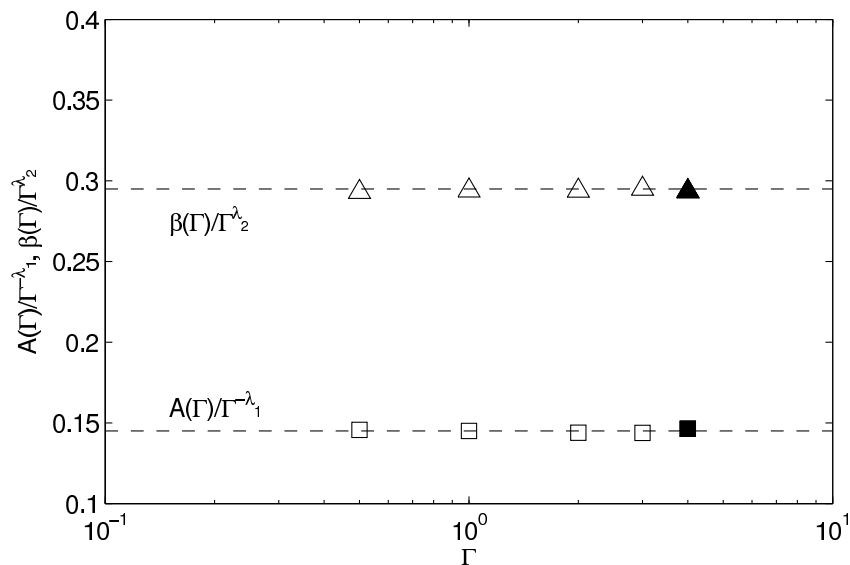
Figure 5.5: Aspect ratio dependence of the fit parameters, $A(\Gamma) \sim \Gamma^{-\lambda_1}$ and $\beta(\Gamma) \sim \Gamma^{\lambda_2}$ as a compensated power law plot. The exponents are $\lambda_1 = 0.18$ and $\lambda_2 = 0.03$. The open symbols correspond to our DNS simulation data and the filled symbols correspond to the data taken from Niemela & Sreenivasan (2006). We have fitted their data from $Ra = 1.10 \times 10^8$ to 9.51×10^9 (see Table 1 therein).

the prefactors depend on Γ and a saturation of the Nusselt number Nu for $\Gamma \geq 10$ has been detected. Third, Funfschilling *et al.* (2005) did not observe any sensitivity of the heat transfer on the aspect ratio in their studies. Their measurements gave power laws of the form

$$Nu(Ra, \Gamma) = A \times Ra^{\beta} , \tag{5.3}$$

but with a continuous drift of the exponent from $\beta = 0.28$ at $Ra \sim 10^8$ up to $\beta = 0.33$ at $Ra \gtrsim 10^{10}$. Their results were essentially unaltered by an increase

in the aspect ratio. On the numerical side, a power law of $Nu \sim \Gamma^{-1}$ for $\Gamma \le 3$ was obtained by Ching & Tam (2006) on the basis of two-dimensional steady state calculations. The present data allows us to compare our results with the scaling

Fit Coefficients	$\Gamma = \frac{1}{2}$	$\Gamma = 1$	$\Gamma = 2$	$\Gamma = 3$
A	0.165	0.145	0.127	0.118
β	0.287	0.294	0.300	0.305

Table 5.2: Nusselt number as a function of the Rayleigh number for different aspect ratios. The scaling $Nu \sim A \times Ra^{\beta}$ has been fit for four aspect ratios.

laws given in Eqns. (5.1)–(5.3). Table 5.2 lists the fit parameters for power laws in the form $Nu = A \times Ra^{\beta}$ for four aspect ratios, namely $\Gamma = 1/2, 1, 2$ and 3. For each aspect ratio, simulations are conducted for four Rayleigh numbers, namely $Ra = 10^7$, 5×10^7, 10^8 and 10^9. Within this range of Ra, we observe a growth of the exponent β from 0.287 to 0.305, which is about 6% variation. Both the prefactor A and exponent β seem to be functions of the aspect ratio and the functional form is thus

$$Nu(Ra, \Gamma) = A(\Gamma) \times Ra^{\beta(\Gamma)} . \tag{5.4}$$

Figure 5.5 shows power law fits of $A(\Gamma) \sim \Gamma^{-\lambda_1}$ and $\beta(\Gamma) \sim \Gamma^{\lambda_2}$ in a compensated form. The measurements that come closest to the present study, both in Rayleigh and Prandtl numbers, are those by Niemela & Sreenivasan (2006) for $\Gamma = 4$. A power law fit for their data range $1.10 \times 10^8 \le Ra \le 9.51 \times 10^9$ yields $Nu = 0.114 \times Ra^{0.306}$. Adding these parameters to Figure 5.5 covers data over almost a decade of Γ. We see that both parameters, A and β, almost perfectly follow the power law with respect to Γ. The exponent for β is small, with $\lambda_2 = 0.03$. The dependence of the prefactor A on Γ is stronger. It is clear that further studies are required to determine whether this weak dependence on Γ prevails at larger Rayleigh numbers. Furthermore, we can expect that, for sufficiently large Γ, both exponents will saturate to geometry-independent values. In addition, the saturation threshold for A and β most likely depends on the Prandtl number, which is constant in our case.

5.3 Large-scale circulation

The coherent structures in turbulent convection can be identified by time averaging of the flow field. We show 2D vector plots in rz plane along $\phi = 0 - \pi$ line for the cells with aspect ratios $\Gamma = 2$ and 3 for the simulations at a fixed Rayleigh number $Ra = 10^7$ in Figure 5.6. We identify a single circulation roll in case of
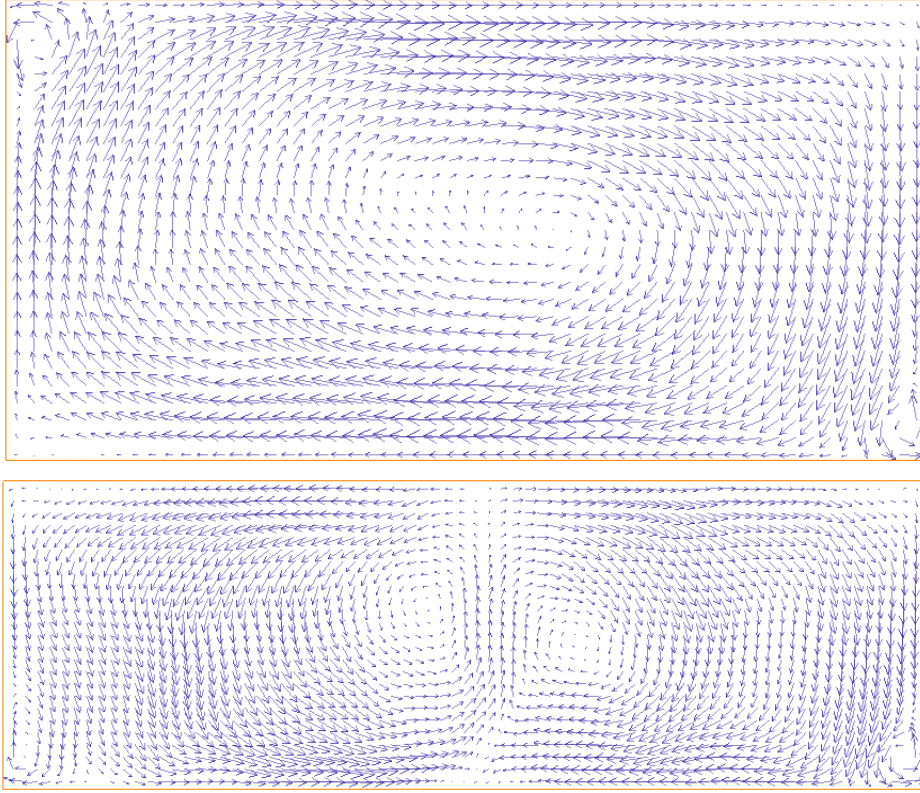
Figure 5.6: 2D vector plots of the mean velocity field in $r-z$ plane along $\phi = 0 - \pi$ line. Simulations are conducted at $Ra = 10^7$ and the velocity field is averaged over 50 snapshots, which are separated each other by $t/t_f = 1$ unit. A single circulation roll is visible for $\Gamma = 2$ cell (top panel) and two counter rotating rolls for $\Gamma = 3$ cell (bottom panel).

$\Gamma = 2$ cell (top panel) and two counter-rotating rolls for $\Gamma = 3$ cell (bottom panel). In Figure 5.7, we present the LSC patterns for three aspect ratios, namely $\Gamma = 2.5$, 3 and 6 at a fixed Rayleigh number $Ra = 10^7$. The streamline plots in the upper three panels have been obtained by averaging the velocity field over 50 consecutive snapshots. These snapshots are separated from each other by $\Delta t = t_f = H/U_f$. Averaging over three disjoint sequences of 50 snapshots leaves the observed LSC patterns unchanged. We conclude, therefore, that the detected LSC pattern is not transient. Transient behavior and large-scale saturation have been investigated by von Hardenberg *et al.* (2008). Our procedure removes not only small-scale fluctuations of the velocity field, but also oscillations of the LSC, which have been observed in recent experiments (e.g. Xi & Xia 2008; Brown & Ahlers 2008), mostly for $\Gamma \leq 1$. Between $\Gamma = 2.5$ and 2.75, the system bifurcates from a one-roll to a two-roll pattern (1st and 2nd columns of Figure 5.7). We have also identified this crossover in LSC between $2.25 < \Gamma < 2.5$ for $Ra = 10^8$. However, for $Ra = 10^9$ we have noticed a single-roll circulation pattern at $\Gamma = 2$ and a triple-roll pattern
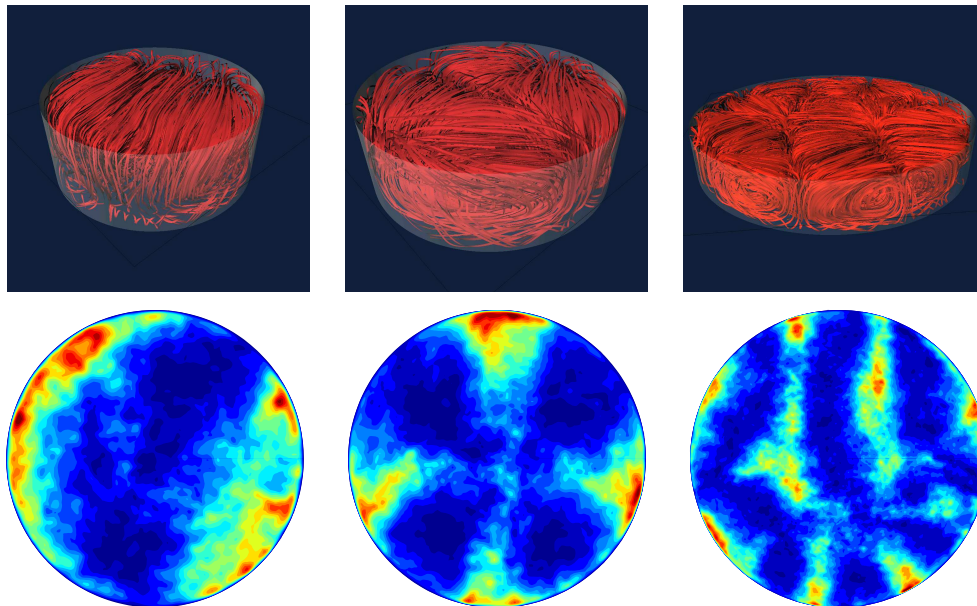
Figure 5.7: Flow patterns at different aspect ratios. Streamlines (top row) and contours of the local heat transfer $u_z\theta$ (bottom row) for three different aspect ratios, $\Gamma = 2.5$ (left column), $\Gamma = 3$ (middle column), and $\Gamma = 6$ (right column), at $Ra = 10^7$ are presented. All data are obtained by time averaging a sequence of 50 statistically independent snapshots. In the bottom row $\langle u_z\theta\rangle_t(r, \phi, z = 1/2)$ is shown.

at $\Gamma = 3$. The intermediate patterns between $2 < \Gamma < 3$ were not resolved in this case. A single-roll close to aspect ratio $\Gamma = 2$ is consistent with the findings of Sun *et al.* (2005), Oresta *et al.* (2007) and Bukai *et al.* (2009). The crossovers of the LSC are marked in Figures 5.4(a,b) by two parallel dashed lines. For all Rayleigh numbers studied here, this crossover takes place at similar, although not exact, values of Γ. With increasing aspect ratio, the LSC becomes a more complex multi-roll configuration, as can be seen in the third column of Figure 5.7 for $\Gamma = 6$.

In the lower row of Figure 5.7, we show the corresponding contour plots of $\langle u_z\theta\rangle_t$ at the midplane. The quantity $u_z\theta$ is the local convective heat flux and $u_z\theta > 0$ if rising and falling plumes are present. The appearance of rising and falling plumes (red in $\langle u_z\theta\rangle_t$ contours) in the three panels (lower row of Figure 5.7) is directly correlated to the corresponding LSC pattern of the time averaged velocity field. We have also verified that almost the same pattern holds for the fluctuations of the local heat transfer, as given by $\langle (u_z\theta)^2\rangle_t$. The LSC patterns were reproduced in the POD analysis by Bailon-Cuba, Emran & Schumacher (2009) as well.

As already indicated in Figure 5.7, the LSC becomes more complex when the aspect ratio becomes larger. For Rayleigh number 10^7, we were able to run a numerical simulation up to $\Gamma = 12$. Figure 5.8 reveals such complex LSC patterns in convective flow for two different Rayleigh numbers, $Ra = 10^7$ and $Ra = 6000$, at $\Gamma = 12$.
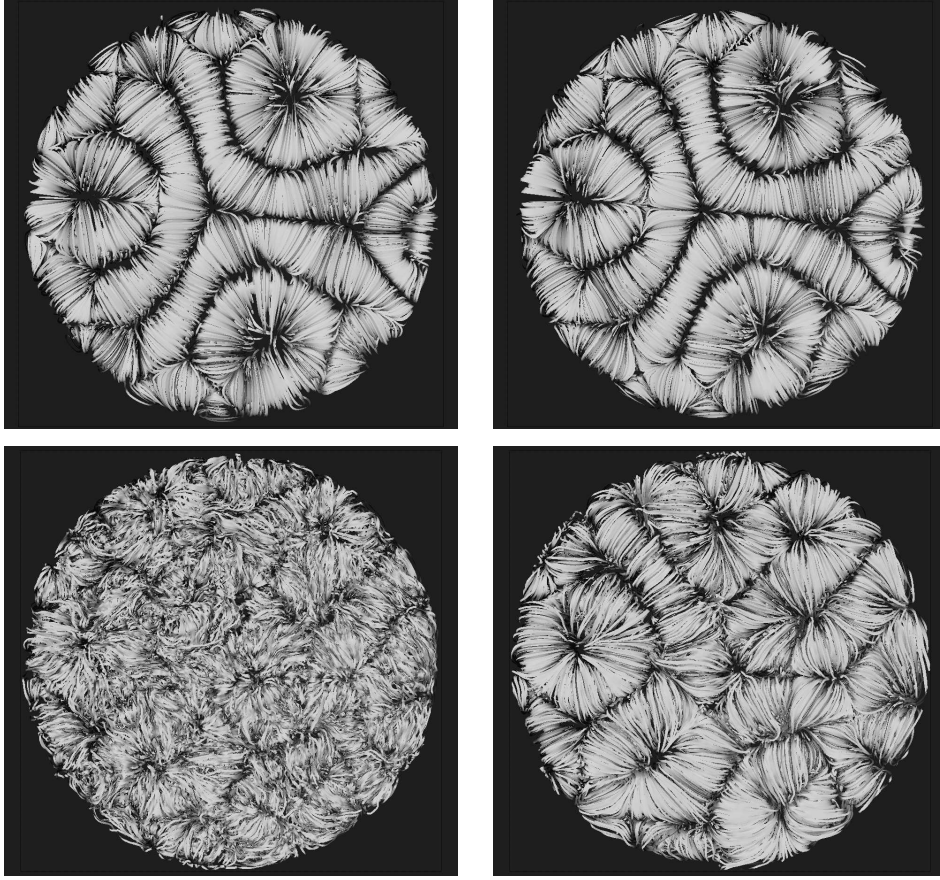
Figure 5.8: Top view of the large scale circulation (LSC) patterns at $\Gamma = 12$ for two different Rayleigh numbers, $Ra = 6 \times 10^3$ (top row) and $Ra = 10^7$ (bottom row). The streamlines of the instantaneous (left column) and time-averaged (right column) velocity field are shown here. In both cases, the time averaging is done over 50 t/t_f time units.
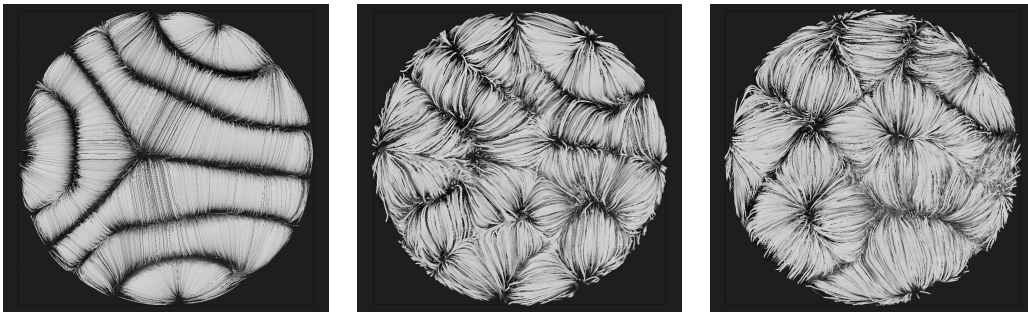
Figure 5.9: Rayleigh number dependence of the LSC. Left panel: $Ra = 6000$. Mid panel: $Ra = 10^7$. Right panel: $Ra = 10^8$. Simulations are conducted in a cell with aspect ratio $\Gamma = 8$. In all cases, the time averaging is done over 50 t/t_f time units.

The left column shows the top view of the streamlines for the instantaneous snapshots for both simulations, while the right column shows the time-averaged velocity field as in Figure 5.7. When the small-scale turbulence (see lower left panel) is filtered out, the resulting pattern is strikingly similar to that in the weakly nonlinear regime immediately above the onset of convection. We observe extended rolls and pentagon-like cells. These patterns have been reported, for example, in experiments by Croquette (1989) with argon at $Pr = 0.69$ for Rayleigh numbers $Ra \approx 2Ra_c$, where Ra_c is the critical Rayleigh number at the onset of convection. Figure 5.9 adds further support to the Rayleigh-number-dependence of the LSC. The left panel nicely displays the extended roll patterns at $Ra = 6000$ and in the cell with aspect ratio $\Gamma = 8$. Relics of these patterns are still present in the mid panel at $Ra = 10^7$. For the largest Rayleigh number, $Ra = 10^8$, the LSC is transformed into a pentagon-like cell structure. Similarly, if we compare the top-right panel of Figure 5.8 to the left panel of Figure 5.9, we see the reorganization of the LSC from roll shape to pentagon or hexagon-like structures with increasing aspect ratio. The LSC patterns can also be identified in the temperature field (Hartlep *et al.* 2005). Their study shows a clear dependence on the Prandtl number.

One possible argument against our observation of Γ–dependent Nusselt number could be that the Rayleigh number for the given Prandtl number $Pr = 0.7$ is still too small and that the convective turbulence has not yet reached the so-called *hard turbulence* regime, as discussed, for example, by Castaing *et al.* (1989). In order to weaken this argument, we determine the dissipation scale and relate it to the height of the cell. Since $Pr < 1$, the diffusive scale of the temperature, the Corrsin scale $\eta_c = (\kappa^3/\langle\epsilon\rangle)^{1/4}$, is larger than the Kolmogorov scale $\eta_K = (\nu^3/\langle\epsilon\rangle)^{1/4}$. The scale separation ratio gives: $H/\eta_K =$133, 278 and 588 for $Ra = 10^7$, 10^8 and $Ra = 10^9$, respectively. Here η_K is directly evaluated from the energy dissipation field as discussed in section 2.5. Even if we take a fraction of H, the scale separation is of $\mathcal{O}(10^2)$. Furthermore, for all the Rayleigh numbers discussed here, we have reported strongly non-Gaussian temperature statistics in chapter 3, which clearly indicate that the convective motion is in a state of fully developed turbulence.

Further similarities between the weakly nonlinear and turbulent regimes can be followed by inspecting the driving mechanisms for the flow circulation. The onset of a LSC is triggered by a slight dominance of buoyancy forces per unit mass, $f_b = g\alpha\theta$, compared to the restoring drag forces per unit mass, $f_d = \frac{1}{2}C(Re)u_z^2H$ (Fontenele Araujo (2005)). The difference between the onset of convection and the turbulent regime is contained in the friction coefficient $C(Re)$. For laminar flows $C(Re) \sim Re^{-1}$ and f_d is a viscous drag force. For larger Re, the force f_d is understood as a turbulent drag force and $C(Re) = const$. This might explain why the characteristic wavenumber does not change significantly.

We can summarize that, for the range of parameters covered here, the LSC patterns do not disappear in the turbulent regime up to $Ra = 10^9$. For the larger aspect ratios, pentagonal or hexagonal cells are formed preferentially.

6 Lagrangian tracer particles

The motion of a fluid particle can be measured either in the Eulerian or Lagrangian frame of reference. In the Eulerian frame, the particle is monitored at fixed points in space, whereas in the Lagrangian case it is monitored along its trajectory. Most of the experimental and numerical investigations in turbulent convection have been conducted in the Eulerian frame of reference. Although Eulerian and Lagrangian studies are complementary, true temporal structures are revealed when the measurement of turbulent fluctuations is conducted along the particle trajectories (Voth *et al.* 2002). With the advancement in sophisticated apparatus, e.g. high resolution cameras, experiments on particles tracking in turbulence have drawn significant attention in recent decades (La Porta *et al.* 2001; Mordant *et al.* 2002; Gasteuil *et al.* 2007; Lobutova *et al.* 2009). Nevertheless, laboratory experiments with particle tracking systems have some limitations, e.g. the size of the tracer particles and the size of domain observable by the digital cameras. DNS on Lagrangian particle tracking has no such limitations, however, the challenging part here is to achieve sufficiently high Reynolds numbers. The staggered grid arrangement allows us to adopt one-dimensional linear interpolation scheme for the velocity in a three-dimensional field and analytical integration for the time marching, which simplifies the computational efforts.

In the beginning of this chapter, we discuss the interpolation scheme for our Lagrangian studies. In the subsequent section, we provide the results, which include particle pair dispersion analysis, heat transfer in the Lagrangian frame, probability distributions of the acceleration as well as the convective heat transfer. Finally, we present some results on Lagrangian velocity and temperature increments.

6.1 Interpolation scheme

The advection of a particle along its trajectory can be described by a set of ordinary differential equations (ODEs) as

$$\frac{d\boldsymbol{x}_p(t)}{dt} = \boldsymbol{u}(\boldsymbol{x}_p, t) \,. \tag{6.1}$$

Here $\boldsymbol{u} = (u_\phi(\phi_p), u_r(r_p), u_z(z_p))^T$ is the velocity of the particle at position $\boldsymbol{x}_p = (\phi_p(t), r_p(t), z_p(t))^T$ in the cylindrical coordinates, with the symbols ϕ, r and z

correspond to the azimuthal, radial and axial directions, respectively. The ODEs in (6.1) have to be solved either by an analytical or a numerical scheme, e.g. the Euler forward method, a Runge-Kutta scheme. Since we have adopted staggered
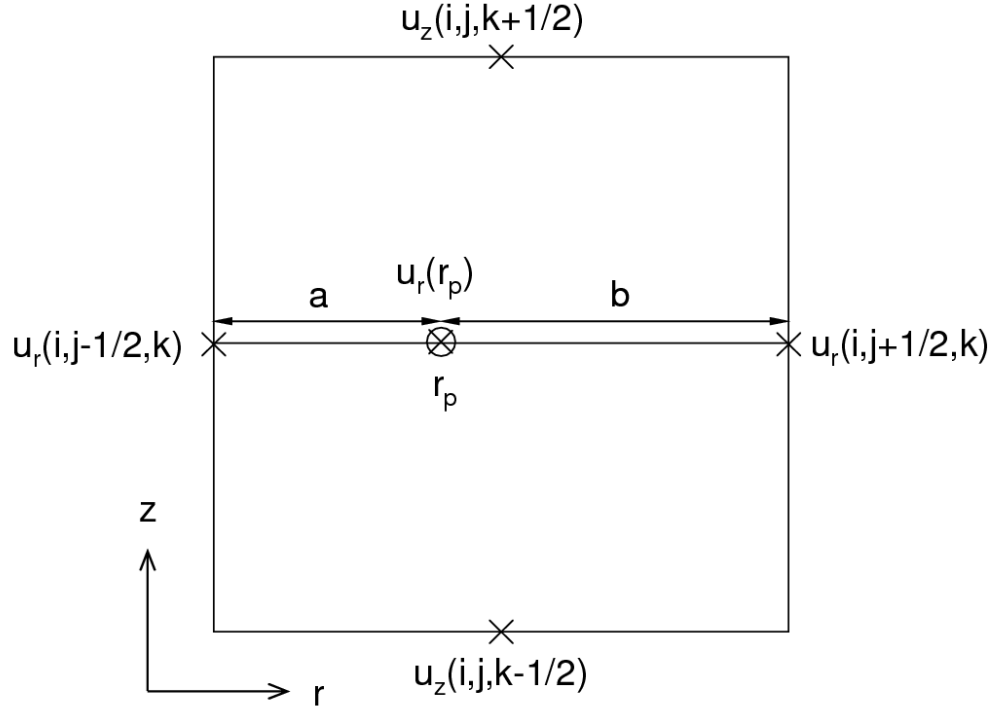
Figure 6.1: Position of the velocity components on a 2D staggered grid in rz plane, which is the mid section of a typical 3D cell as shown in Figure 2.2 in the cylindrical coordinates. The indices i, j and k correspond to the azimuthal, radial and axial directions, respectively. The particle velocity $u_r(r_p)$ at position r_p is obtained by the linear interpolation of the Eulerian velocities $u_r(i, j - 1/2, k)$ and $u_r(i, j + 1/2, k)$.

grid for the Eulerian simulations, we need only one-dimensional linear interpolation of the velocity components as shown in Figure 6.1. Given the Eulerian velocities at the mid points of the edges of a 2D cell (Figure 6.1, see also Figure 2.2), we calculate the corresponding Lagrangian components at an arbitrary position inside the cell as

$$u_r(r_p) = \frac{a \times u_r(i, j + 1/2, k) + b \times u_r(i, j - 1/2, k)}{a + b}, \tag{6.2}$$

$$u_\phi(\phi_p) = \frac{c \times u_\phi(i + 1/2, j, k) + d \times u_\phi(i - 1/2, j, k)}{c + d}, \tag{6.3}$$

$$u_z(z_p) = \frac{e \times u_z(i, j, k + 1/2) + f \times u_z(i, j, k - 1/2)}{e + f}. \tag{6.4}$$

With the help of the interpolation scheme described above, one can derive analytical solutions of the ODEs in Eqn. (6.1). Following Schönfeld (1995), we rewrite the ODE in the r-direction as

$$\frac{dr_p}{dt} = u_r(r_p) = \frac{r_p - r_L}{r_R - r_L}u_{r,R} + \left(1 - \frac{r_p - r_L}{r_R - r_L}\right)u_{r,L}, \tag{6.5}$$

where $u_{r,R}$ and $u_{r,L}$ are the velocities at known positions r_R and r_L, respectively and r_p is the particle's position in between. The subscripts L and R refer to the left and right faces of a 3D-cell (Figure 2.2), respectively. Rearranging Eqn. (6.5) yields (Wolk 2003)

$$\frac{dr_p}{dt} + r_p(-\frac{\Delta u_r}{\Delta r}) = u_{r,L} - r_L\frac{\Delta u_r}{\Delta r}, \tag{6.6}$$

with $\Delta u_r = u_{r,R} - u_{r,L}$ and $\Delta r = r_R - r_L$. Multiplying both sides of Eqn. (6.6) with the integration factor $e^{-\frac{\Delta u_r}{\Delta r}t}$ gives

$$\frac{d}{dt}\left(r_p\,e^{-\frac{\Delta u_r}{\Delta r}t}\right) = \left(u_{r,L} - r_L\frac{\Delta u_r}{\Delta r}\right)e^{-\frac{\Delta u_r}{\Delta r}t}. \tag{6.7}$$

Now integrating both sides of Eqn. (6.7) with respect to t gives the r-position of the particle as

$$r_p(t) = r_L - u_{r,L}\frac{\Delta r}{\Delta u_r} + C\,e^{\frac{\Delta u_r}{\Delta r}t}. \tag{6.8}$$

At $t = t_0$

$$r_p(t_0) = r_L - u_{r,L}\frac{\Delta r}{\Delta u_r} + C\,e^{\frac{\Delta u_r}{\Delta r}t_0}. \tag{6.9}$$

Subtracting Eqn. (6.9) from Eqn. (6.8) results in

$$\delta r = r_p(t) - r_p(t_0) = C\left(e^{\frac{\Delta u_r}{\Delta r}t} - e^{\frac{\Delta u_r}{\Delta r}t_0}\right). \tag{6.10}$$

From Eqn. (6.9) and with $r_p(t_0) = r_0$, the constant C is

$$C = \left(r_0 - r_L + u_{r,L}\frac{\Delta r}{\Delta u_r}\right)e^{-\frac{\Delta u_r}{\Delta r}t_0}. \tag{6.11}$$

From Eqn. (6.6)

$$\frac{dr_p}{dt}\Big|_{t=t_0} = u_{r,0} = r_0\frac{\Delta u_r}{\Delta r} + u_{r,L} - r_L\frac{\Delta u_r}{\Delta r}, \tag{6.12}$$

which implies

$$r_0 = u_{r,0}\frac{\Delta r}{\Delta u_r} - u_{r,L}\frac{\Delta r}{\Delta u_r} + r_L. \tag{6.13}$$

Eliminating r_0 from Eqn. (6.11) with the help of Eqn. (6.13) gives

$$C = u_{r,0}\frac{\Delta r}{\Delta u_r}e^{-\frac{\Delta u_r}{\Delta r}t_0}. \tag{6.14}$$

Substituting the value of C in Eqn. (6.10), we get the distance travels by the particle in the r-direction for the time increment $\delta t = t - t_0$ as

$$\delta r = u_{r,0}\frac{\Delta r}{\Delta u_r}\left(e^{\frac{\Delta u_r}{\Delta r}\delta t} - 1\right). \qquad (6.15)$$

Similarly, for the azimuthal and axial directions, the distances are

$$\delta\phi = \frac{u_{\phi,0}}{r_0}\frac{\Delta\phi}{\Delta u_\phi}\left(e^{\frac{\Delta u_\phi}{\Delta\phi}\delta t} - 1\right), \qquad (6.16)$$

$$\delta z = u_{z,0}\frac{\Delta z}{\Delta u_z}\left(e^{\frac{\Delta u_z}{\Delta z}\delta t} - 1\right). \qquad (6.17)$$

The equations of the particle trajectories in the Lagrangian frame are

$$r_p(t) = r_p(t_0) + \delta r, \qquad (6.18)$$
$$\phi_p(t) = \phi_p(t_0) + \delta\phi, \qquad (6.19)$$
$$z_p(t) = z_p(t_0) + \delta z. \qquad (6.20)$$

On a staggered grid, the temperature T is stored at the cell center (Figure 2.2). At first, we interpolate T at the vertices of the Eulerian grid and then apply trilinear interpolation to calculate the Lagrangian temperature at a known particle position.

6.2 Results

For the Lagrangian simulations, we have selected cylindrical cells with aspect ratios $\Gamma = 1$ and 3 for $Ra = 10^7$, and $\Gamma = 1$ for $Ra = 10^8$ keeping the Prandtl number constant ($Pr = 0.7$). About 10^5 tracer particles are dispersed in the cell and advected over $200\,t/t_f$ time units. The statistical analysis is conducted over 4000 independent samples, which are separated each other by $\Delta t = 0.05$.

We visualize the time-evolution of the trajectories of particles in Figure 6.2 for a simulation at $Ra = 10^7$ in the Rayleigh-Bénard cell with aspect ratio $\Gamma = 1$. It seems that a particular particle (left panel of Figure 6.2) travels along the large-scale circulation (LSC). Figure 6.3 plots the time signals of various quantities along a particle path for the same simulation. The results are qualitatively in agreement with the Eulerian measurements by Shang *et al.* (2004) and the Lagrangian measurements by Gasteuil *et al.* (2007). Sharp spikes of the temperature signal (Figure 6.3a bottom panel) appear due to plumes close to the hot and cold plates (Figure 6.3a top panel), where intense plume activities occur. The hot and cold plumes in a particular zone counteract with each other and as a result the hot ones lose and the cold ones gain the temperature. Hence, the amplitude of those peaks in $T(t)$ signal is less than the extremum value (0 or 1), eventhough it seems that
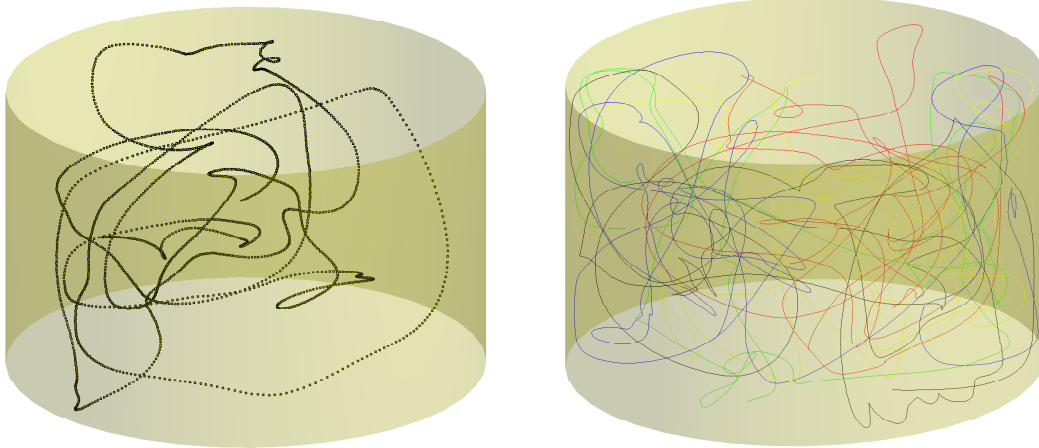
Figure 6.2: Three-dimensional trajectories of particles for the Lagrangian simulation at $Ra = 10^7$ in the cell with aspect ratio $\Gamma = 1$. The left panel represents the path of a single particle and the right panel for five particles, which are distinguished from each other by a separate color.

(a) Signals of z, u_z and T

(b) Signals of fluxes $u_x T$, $u_y T$ and $u_z T$
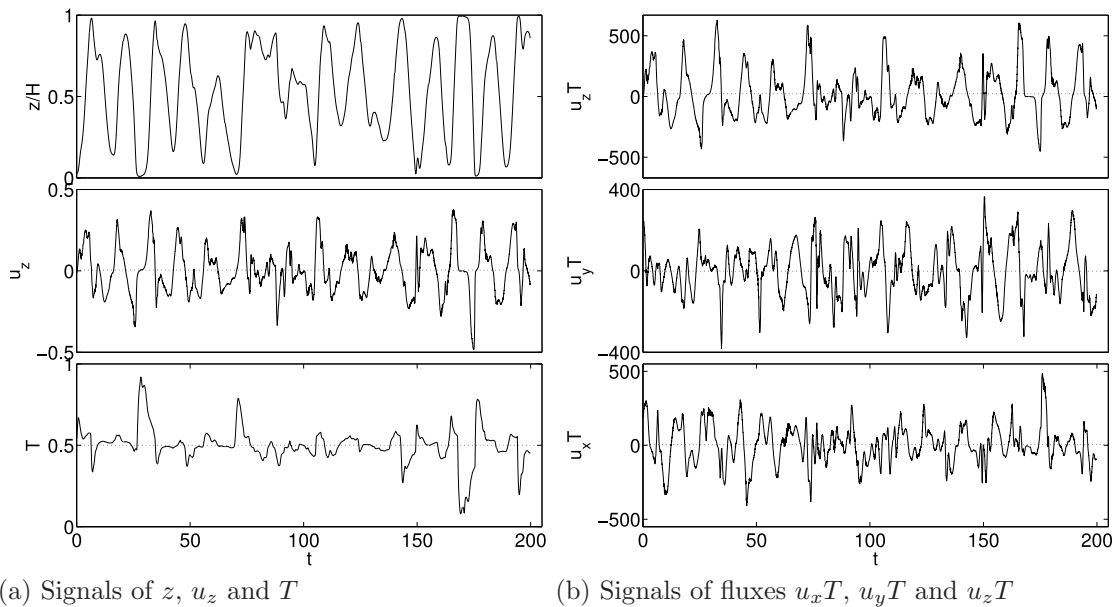
Figure 6.3: Time signals of various quantities along the trajectory of a particle: (a) (top to bottom) the vertical position $z(t)$ normalized by the cell height H, the vertical velocity $u_z(t)$ and the temperature $T(t)$, respectively; (b) (top to bottom) the convective heat fluxes $u_z T$, $u_y T$ and $u_x T$, respectively. The dotted line shows the corresponding mean value.

the particle position is close to the top and bottom plates as indicated in the signal of the vertical position $z(t)$ in the top panel of Figure 6.3a. The vertical velocity

$u_z(t)$ has zero mean (Figure 6.3a mid panel). The signals of the convective fluxes (Figure 6.3b) are highly irregular with sharp peaks as well, which are the signature of intermittency. The factor $\sqrt{RaPr}$ is multiplied with the flux terms u_xT, u_yT and u_zT in order to get the appropriate values. The mean values are 4.8, -1.7 and 23.4 for u_xT, u_yT and u_zT, respectively, which indicate that the vertical flux u_zT is responsible for the net heat transfer in the cell.

6.2.1 Heat transfer in the Lagrangian frame

Similar to Eqn. (2.20), the Nusselt number in the Lagrangian frame, Nu_L, is given by

$$Nu_L = 1 + \frac{H}{\kappa \Delta T} \langle u_z T \rangle_{L,t} , \qquad (6.21)$$

where the symbol $\langle . \rangle_{L,t}$ denotes an averaging over all trajectories and statistically
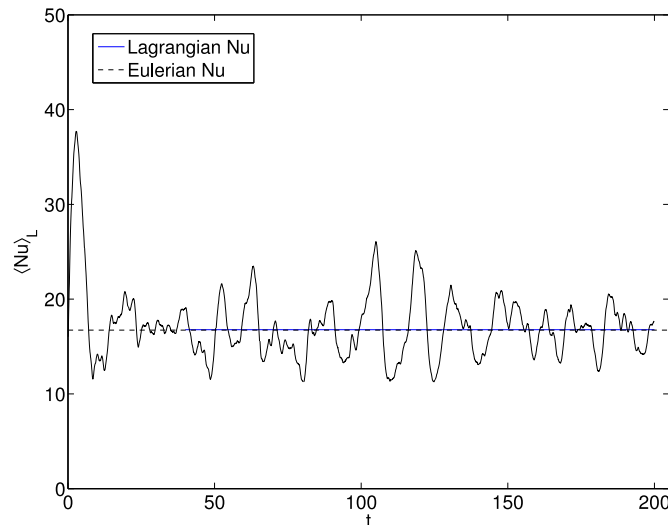
Figure 6.4: Graph of $\langle Nu \rangle_L$ over time, which is averaged over 10^5 tracer paths. The mean value of $\langle Nu \rangle_L (t)$ curve between time $t = 40 - 200$ is $Nu_L = 16.77$, which almost exactly matches the corresponding Eulerian value $Nu = 16.73$ as listed in Table 5.1.

independent realizations of turbulent fields. We compute the heat transfer in the Lagrangian frame and compare with its value in the Eulerian frame in Figure 6.4 for a simulation at $Ra = 10^7$ in the cell with aspect ratio $\Gamma = 1$. About 10^5 tracer particles are seeded in several horizontal planes along the axis of the cylindrical cell and 4000 snapshots, with a separation $\Delta t = 0.05$, are stored for the statistical analysis. The time averaging of $\langle Nu \rangle_L (t)$ curve from $t = 40$ to 200 yields $Nu_L = 16.77$, which almost exactly matches the corresponding value of the Eulerian simulation, which was $Nu = 16.73$ as provided in Table 5.1. Similar result

is achieved for the simulation conducted at $Ra = 10^8$ in the same cell, for which $Nu = 32.21$ and $Nu_L = 31.74$ with a deviation of 1.5%. The results validate our interpolation schemes and the time step sizes for the Lagrangian simulations, which are accurate enough to reproduce flow quantities of the corresponding Eulerian simulations in turbulent convection. In contrast, recent experiment by Gasteuil *et al.* (2007) obtained a value of Nu_L almost twice as large as the Eulerian case. This huge discrepancy in their measured value could be attributed to the fact that the mobile sensor used in their measurements preferentially moved along the large-scale circulation (LSC) path and a significant portion of bulk region was not traversed by the sensor. However, in order to achieve the appropriate value of the global Nusselt number, all regions of the convection cell have to be taken into account. In addition, their sensor dimension was larger than the thickness of the boundary layers. Therefore, the boundary layer contribution was missing there as well.

At the beginning of $\langle Nu \rangle_L (t)$ curve in Figure 6.4, there is a large over-shoot from the mean value, which generally appears when the majority of the particles follow the LSC path or all portions of the flow domain are not seeded uniformly at the same time by the particles. For the same reasons, we see there are spike like jumps from the mean, for example between $t = 100$ and 130. We also conducted a simulation (results are not shown here) for the same Ra and Γ, in which the number of particles was increased by a factor of 2.5 compared to the one shown in Figure 6.4. There, the particles were seeded uniformly in the domain. We observed that the convergence of Nu was achieved within a shorter period in that case. Therefore, we conclude that the number of tracer particles should be sufficiently large and they should be uniformly seeded in the domain for the rapid convergence. Conversely, the convergence is slower for a small number of tracer particles with a non-uniform initial seeding.

6.2.2 Pair dispersion

The pair dispersion, R^2, is a measure of the relative separation of a pair of particles traversing along their trajectories, which is can be written as

$$R^2(t) = \left\langle [\boldsymbol{x}_p(t) - \boldsymbol{x}_p(t_0)]^2 \right\rangle_L . \tag{6.22}$$

We resolve the dispersion vector into two parts – the lateral part $\boldsymbol{R}_{xy}(t)$ and the vertical part $\boldsymbol{R}_z(t)$. Their contributions to the total dispersion are

$$
\begin{aligned}
R_{xy}^2(t) &= \left\langle [x_p(t) - x_p(t_0)]^2 + [y_p(t) - y_p(t_0)]^2 \right\rangle_L , &\tag{6.23}\\
R_z^2(t) &= \left\langle [z_p(t) - z_p(t_0)]^2 \right\rangle_L . &\tag{6.24}
\end{aligned}
$$
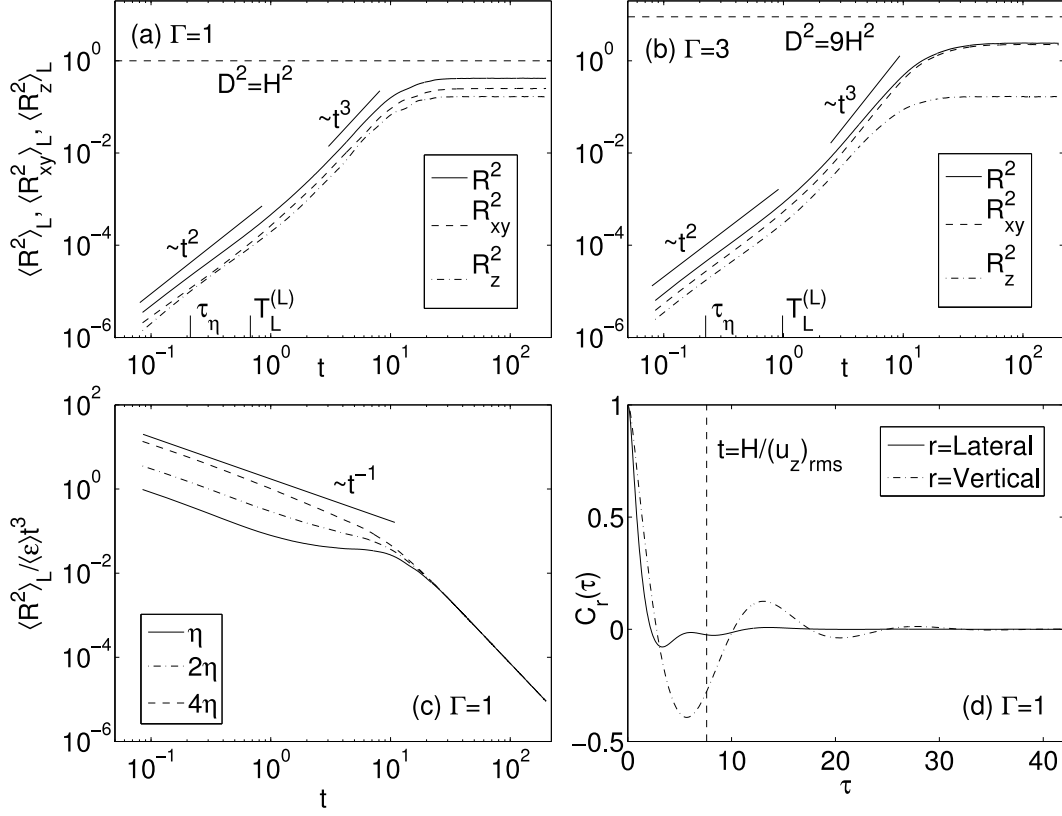
Figure 6.5: Pair dispersion parameters as in Eqns. (6.22)–(6.24): (a) aspect ratio $\Gamma = 1$, (b) $\Gamma = 3$, (c) normalized pair dispersion with respect to three initial separations, namely η, 2η and 4η, with η the Kolmogorov length and (d) the autocorrelation functions of the lateral and vertical velocities for $\Gamma = 1$ as given in Eqns. (6.25) and (6.26), respectively. The Kolmogorov time τ_η (as in Eqn. (6.28)) and the lateral Lagrangian time $T_L^{(L)}$ (given in Eqn. (6.27)) are marked on the time axis in (a) and (b). The horizontal dashed lines in (a) and (b) denote the square of the maximum dimension of the corresponding cell. The vertical dashed line in (d) represents the characteristic time required by a particle to travel the cell of height H. The analysis is conducted at $Ra = 10^7$ with 4.16×10^8 and 3.24×10^8 statistical samples for $\Gamma = 1$ and $\Gamma = 3$, respectively.

We also compute the autocorrelation functions of the velocity components as

$$C_{xy}(t) \quad = \quad \frac{\langle \boldsymbol{u}_{xy}(t + \tau) \cdot \boldsymbol{u}_{xy}(t) \rangle}{\langle |\boldsymbol{u}_{xy}|^2 \rangle} \,, \tag{6.25}$$

$$C_z(t) \quad = \quad \frac{\langle u_z(t + \tau) u_z(t) \rangle}{\langle u_z^2 \rangle} \,. \tag{6.26}$$

Here C_{xy} is the autocorrelation coefficient for the lateral velocities $\boldsymbol{u}_{xy} = u_x \cdot \boldsymbol{e}_x + u_y \cdot \boldsymbol{e}_y$, with $\boldsymbol{e}_x$ and $\boldsymbol{e}_y$ are the identity vectors in x and y directions, respectively and C_z is for the vertical velocity u_z. The symbol τ is the time lag.
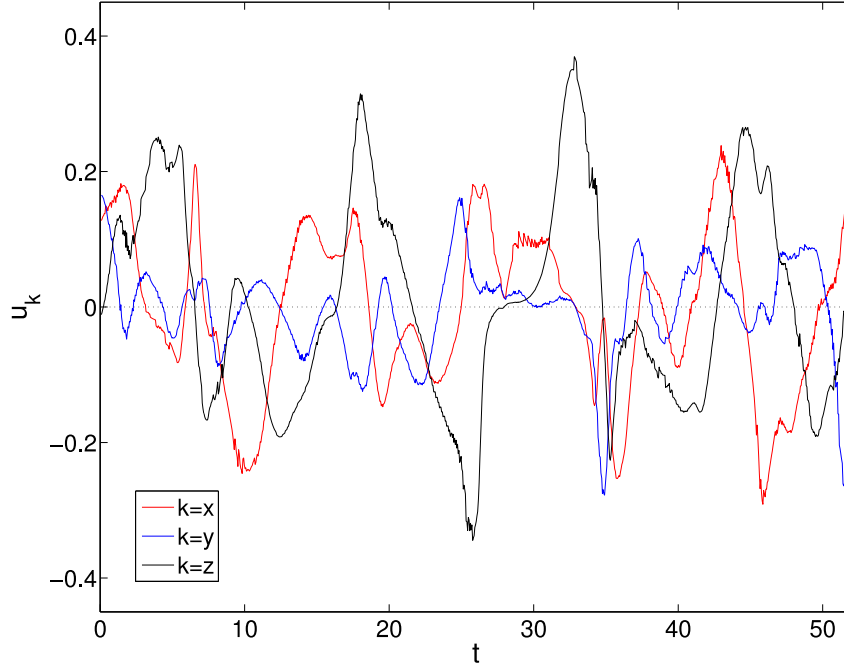
Figure 6.6: Signals of the velocity components u_x, u_y and u_z.

The lateral Lagrangian time $T_L^{(L)}$ is obtained by integrating C_{xy} as

$$T_L^{(L)} = \int_0^\infty C_{xy}(\tau)\,\mathrm{d}\tau\,, \tag{6.27}$$

and the Kolmogorov time τ_η is given by

$$\tau_\eta = \sqrt{\frac{\nu}{\langle\epsilon\rangle}}\,. \tag{6.28}$$

The energy dissipation rate ϵ is calculated from Eqn. (2.23).

Figures 6.5(a,b) plot the total dispersion, R^2, as well as the lateral, R_{xy}^2, and vertical, R_z^2, components. Two aspect ratios are selected, namely $\Gamma = 1$ and 3 for simulations at $Ra = 10^7$. Initially, the quantities grow with $R^2 \sim t^2$, which corresponds to the ballistic dispersion. After the ballistic growth, a transition to the Richardson-like regime ($R^2 \sim t^3$) occurs. Similar observations were made by Boffetta & Sokolov (2002) and Schumacher (2008, 2009). The horizontal dashed lines mark the limit of the pair separation growth, which is the square maximum dimension of the cell. Hence, a plateau is reached without crossing the limit. The finite size of the cell suppresses the dispersion limit, hence a Taylor-like regime ($R^2 \sim t$) is absent here in contrast to the results obtained by Schumacher (2008, 2009) for rectangular domains with free-slip top and bottom boundaries and periodic sidewalls. The Kolmogorov time units τ_η are 0.212 and 0.223, and the lateral Lagrangian time units $T_L^{(L)}$ are 0.675 and 0.982 for $\Gamma = 1$ and 3, respectively. The normalized pair

dispersion with respect to three different initial separations, namely η, 2η and 4η, with η is the Kolmogorov length, are given in Figure 6.5c, which indicates that the pair dispersion is sensitive to the initial separation. The autocorrelation functions of the lateral and vertical velocities are shown in Fig. 6.5d. The results are in agreement with Schumacher (2008). The vertical velocity is strongly anticorrelated to the lateral ones. The strong anticorrelation is in line with the rapid upward and downward motions as indicated by the signals of velocity components along a tracer path in Figure 6.6, in which fluctuations in $u_z(t)$ are stronger than those in $u_x(t)$ or $u_y(t)$. This causes fast separations of the tracer pair.
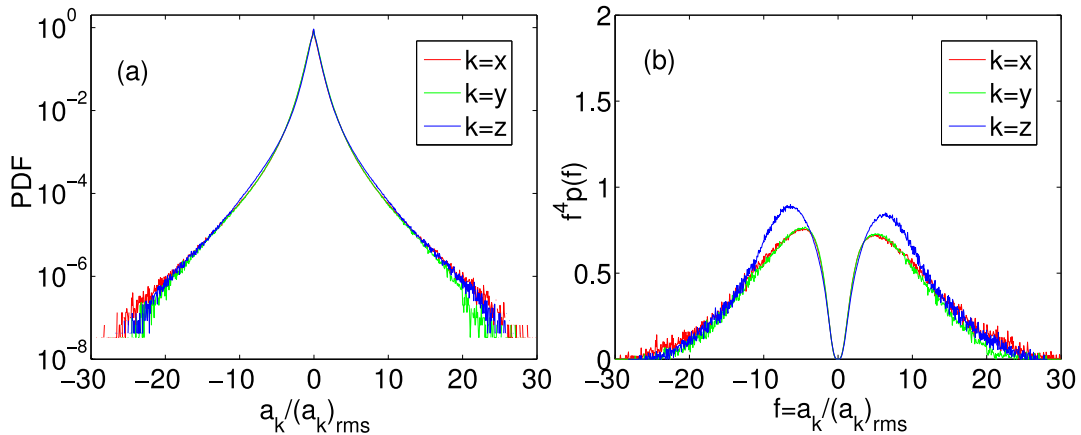
Figure 6.7: The probability density functions of the acceleration components are plotted in (a). The statistical convergence test of the 4th order moment of PDFs are shown in (b). The PDFs are normalized by their rms values. The data set corresponds to $Ra = 10^7$, $\Gamma = 1$ and 4.16×10^8 events are included in the statistical analysis. The normalized 4th order moment is the area below the curve in (b) and is given by $F(a_k) = \int (a_k^4/a_{k,rms}^4)\, \mathrm{p}(a_k/a_{k,rms})\, \mathrm{d}(a_k/a_{k,rms}) = \left\langle a_k^4/a_{k,rms}^4 \right\rangle = \left\langle a_k^4 \right\rangle / \left\langle a_k^2 \right\rangle^2$.

6.2.3 Probability density of the acceleration

We report the probability density of acceleration components along the 3D trajectories in Figure 6.7a for a data set $\Gamma = 1$ and $Ra = 10^7$. The accelerations are obtained by using the 2nd order central difference scheme. The PDF of all components has a stretched exponential shape similar to those reported in the experiment by La Porta *et al.* (2001) and DNS simulations by Schumacher (2008, 2009). The rms values of the accelerations a_k, with $k = x$, y or z, and the corresponding skewness $S(a_k) = \left\langle a_k^3 \right\rangle / \left\langle a_k^2 \right\rangle^{3/2}$ and flatness $F(a_k) = \left\langle a_k^4 \right\rangle / \left\langle a_k^2 \right\rangle^2$ factors are listed in Table 6.1 for two Rayleigh numbers, namely $Ra = 10^7$ and 10^8. The PDFs are almost symmetric with small skewness and have flatness factors that exceed the

Gaussian one by almost an order of magnitude ($F(a_k) \gg 3$). The PDFs of all three components collapse, in contrast to those in a laterally unbounded fluid layer (Schumacher 2008, 2009). Here, extreme events with accelerations larger than one order of magnitude of the rms value are visible. This indicates that the acceleration is highly intermittent. The values of $F(a_k)$ are of the same order of magnitude as those of Voth *et al.* (2002) and Schumacher (2009). Since the tails of the PDF of 4th-order moment in Figure 6.7b are not much scattered, the statistical convergence is established in our study.

Ra	Γ	a_k	$(a_k)_{rms}$	$\frac{\max(a_k)}{(a_k)_{rms}}$	$\frac{\min(a_k)}{(a_k)_{rms}}$	$S(a_k)$	$F(a_k)$
10^7	1	a_x	0.139	32.74	-30.20	0.028	19.10
10^7	1	a_y	0.139	28.13	-27.22	0.004	17.54
10^7	1	a_z	0.177	27.78	-26.67	0.005	20.13
10^8	1	a_x	0.171	38.34	-40.63	-0.015	23.16
10^8	1	a_y	0.170	33.60	-38.84	-0.026	21.00
10^8	1	a_z	0.203	40.00	-41.12	0.010	27.55

Table 6.1: The rms value $(a_k)_{rms} = \sqrt{\langle a_k^2 \rangle}$ of the acceleration components and the skewness $S(a_k) = \langle a_k^3 \rangle / \langle a_k^2 \rangle^{3/2}$ and flatness $F(a_k) = \langle a_k^4 \rangle / \langle a_k^2 \rangle^2$ factors are listed here. The statistics are gathered over 4.16×10^8 and 4.5×10^8 events for $Ra = 10^7$ and $Ra = 10^8$, respectively.

6.2.4 Probability density of the convective heat flux

Figure 6.8 shows the probability distributions of the convective heat fluxes for a simulation at $Ra = 10^8$ in the convection cell of aspect ratio $\Gamma = 1$. The distributions are super-Gaussian with sparse tails. The non-Gaussianity is due to the intermittency. Other studies by Shang *et al.* (2004) and Gasteuil *et al.* (2007) reported stretched exponential shapes, however, their Rayleigh numbers are much higher. The PDF of the vertical flux $u_z T$ is positively skewed, since it is responsible for the net heat transfer in the cell. The PDFs of the lateral components $u_x T$ and $u_y T$ almost collapse except for small deviations in the tails. The distributions are different from those observed by Schumacher (2009).
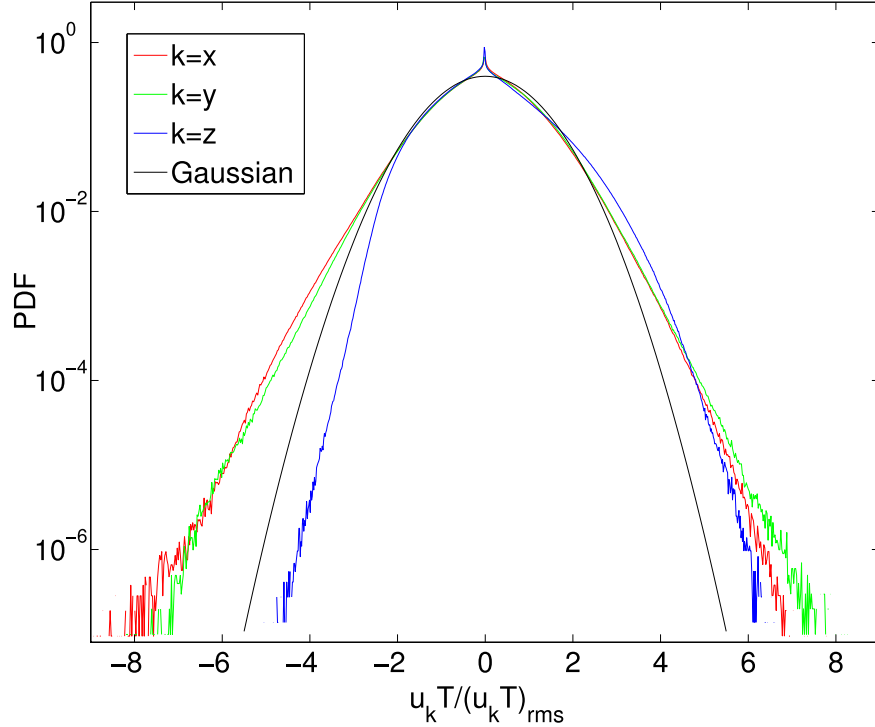
Figure 6.8: Probability density functions of the convective fluxes. The PDF is normalized with the corresponding rms value. The analysis is conducted for 4.5×10^8 events in the convection cell with aspect ratio $\Gamma = 1$ for a simulation at $Ra = 10^8$.

6.2.5 Probability density of the velocity and temperature increments

The vertical velocity increment in the Lagrangian frame is defined as

$$\delta_\tau u_z(t) = u_z(t + \tau) - u_z(t), \tag{6.29}$$

and the temperature increment is

$$\delta_\tau T(t) = T(t + \tau) - T(t). \tag{6.30}$$

The symbol τ denotes the time lag. We plot the PDFs of $\delta_\tau u_z$ and $\delta_\tau T$ with respect to four different time lags in Figure 6.9. The time lags are $\tau \approx \tau_\eta$, $1.33T_L$, $2.66T_L$ and $5.33T_L$, where τ_η and T_L are the Kolmogorov and Lagrangian time units, respectively. The Lagrangian time T_L is obtained by integrating the autocorrelation function of the velocity. In this case $T_L \approx 0.3$ and $\tau_\eta \approx 0.21$. The colors red, green, blue and magenta correspond to $\tau \approx \tau_\eta$, $1.33T_L$, $2.66T_L$ and $5.33T_L$, respectively. The Gaussian distribution (marked by the black curve) is shown as well for the comparison. The PDFs of $\delta_\tau u_z$ (Figure 6.9a) are symmetric and non-Gaussian and similar to those observed by Mordant *et al.* (2002) in fluid turbulence and by Gasteuil *et al.* (2007) in convection. For $\tau \approx \tau_\eta$ and $1.33T_L$, the PDFs have fatter
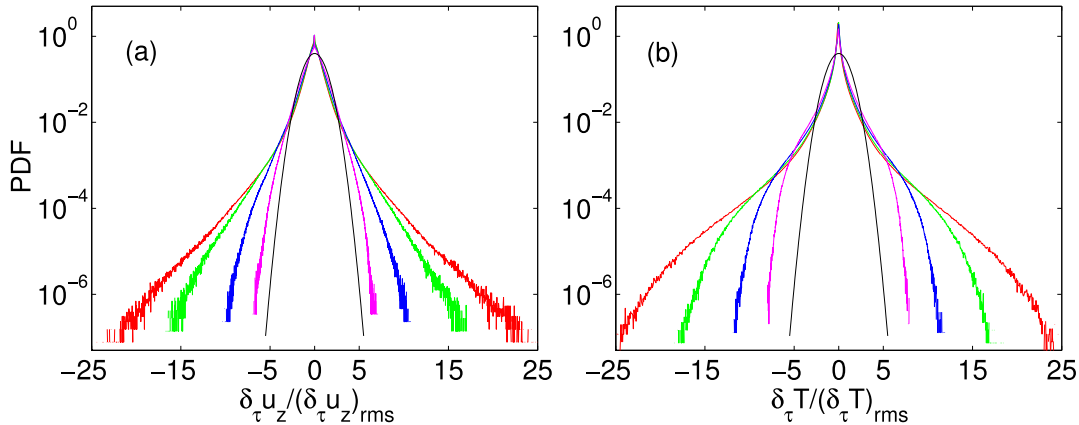
Figure 6.9: The probability density functions of the vertical velocity and temperature increments as a function of four different time lags, namely $\tau \approx \tau_\eta$ (red), $1.33T_L$ (green), $2.66T_L$ (blue) and $5.33T_L$ (magenta) with τ_η and T_L are the Kolmogorov and Lagrangian time units, respectively. The Lagrangian time T_L is obtained by integrating the autocorrelation function of the velocity. In this case $T_L \approx 0.3$ and $\tau_\eta \approx 0.21$. The black curve corresponds to the Gaussian distribution. Each PDF is normalized with the corresponding rms value. The data are taken for the simulation at $Ra = 10^7$ in the cell with aspect ratio $\Gamma = 1$. The statistics are accumulated for 4.16×10^8 statistically independent events.

tails with the stretched exponential shape due to the intermittency. However, they keep their exponential forms for $\tau \gg T_L$. In contrast, Mordant *et al.* (2002) found Gaussian distributions for $\tau > T_L$ in fluid turbulence. The distributions for $\delta_\tau T$ (Figure 6.9b) are non-Gaussian and slightly skewed with sparse tails in contrast to that of $\delta_\tau u_z$. In the Eulerian measurements by Zhou & Xia (2002), it was found that, in the inertial range, the distributions of $\delta_\tau T$ are exponential at the center and stretched exponential close to the sidewall. In addition, stronger intermittency in the temperature increments was observed at the side wall compared to the center. The PDF, which displayed here, is another manifestation of the strong small-scale intermittency. The next step would be to compare the PDFs of the temperature increments for different Rayleigh numbers.

7 Summary and outlook

We have conducted detailed numerical investigations in turbulent Rayleigh-Bénard convection in a cylindrical cell. Our analyses focused on the following areas: the statistics of the temperature, its fluctuations and gradients; the statistics of the thermal dissipation rate and its scaling with respect to the Rayleigh number; the dependence of the heat transfer on the aspect ratio and the corresponding changes in the large-scale circulation (LSC) patterns; and the Lagrangian particle dispersion in turbulent convection. Our simulation parameters vary from $Ra = 10^7 - 10^9$ and $\Gamma = 0.5 - 12$. The Prandtl number $Pr = 0.7$ remains constant throughout the study.

In the first part of this work, we have reported the fine-scale statistics of the temperature, its fluctuations and gradients as well as the statistics of the thermal dissipation rate and its scaling with respect to Ra for the data set $Ra = 10^7 - 10^9$ and $\Gamma = 1$. The constraints on the DNS grid resolution limited the study to the moderate Rayleigh number range. We have compared the fine-scale statistics of the active temperature field to that of the passive scalar field, far away from the boundaries. In contrast to the passive scalar case, the temperature statistics is always non-Gaussian with a probability density function (PDF) close to the exponential shape in the bulk. Non-Gaussianity holds in all regions of the convection cell and for all mentioned Rayleigh numbers. Deviations in temperature fluctuations from the Gaussian distribution have also been confirmed by the V-shaped conditional mean thermal dissipation rate. In case of the passive scalar fluctuations, the statistics depends on the mechanism that sustains the fluctuations and on the particular ratios of outer turbulence length scales. Super-Gaussian, Gaussian or weakly sub-Gaussian distributions have been observed there in the past. While the statistics of the temperature differ from the passive scalar, the statistics of the spatial derivatives and dissipation rates behave qualitatively similarly.

The PDF of the thermal dissipation rate in the bulk fits well with a stretched exponential. The tails are extended to larger amplitudes with increasing Rayleigh number. This is a clear fingerprint of a stronger small-scale intermittency. Thermal dissipation field is always more intermittent in the boundary layers than the bulk region of the convection cell. This is manifested by the extended tail of the PDF. Furthermore, the flow in the sidewall region exhibits stronger intermittency than in the inner bulk. This is caused by the movements of plumes along the large-scale circulation path in the sidewall zone and the presence of unstable temperature gradients close to the sidewalls as demonstrated by Brown & Ahlers (2007). All

distributions showed clear deviations from the log-normality in the whole range of dissipation values. This has consequences for closures that usually rely on log-normal form.

Motivated by similar studies in passive scalar turbulence and by our detection of locally varying mean temperature profiles, the deviations from locally isotropic temperature fluctuations are quantified by the third order vertical derivative moments as a function of the Rayleigh number. Interestingly, we found that the deviations from the local isotropy grow with increasing Ra in the boundary layer. In the bulk, the derivative skewness is found to decrease, which indicates a return to local isotropy (Lumley 1967). This is observed when translating the original Reynolds number dependence of the skewness into a Rayleigh number dependence for the convection case. In contrast, the passive scalar does not display such trend (Warhaft 2000). The observed trend might be due to the small amplitudes that the local mean temperature gradients possess in a convection cell.

The vertical profiles of the plane averaged thermal dissipation rate show that an increasing fraction is concentrated in an ever thinner boundary layer with growing Ra. Furthermore, we have demonstrated that the contribution of the temperature fluctuations to the total thermal dissipation rate, ϵ_T, in the thermal boundary layer is significant, which is about 25% ϵ_T for $Ra = 10^9$. This aspect is usually neglected in the scaling theories and could explain why the trends of $\langle \epsilon_T \rangle \sim Ra^\zeta$ obtained in our analyses differ from those by Grossmann & Lohse (2000). From the balance of the temperature variance, we have obtained a power law scaling for the length of the plume mixing zone, l_m, as $l_m = 0.5 \times Ra^{-0.15}$, which is of the same order of magnitude as the one predicted by Procaccia $et\ al.$ (1991) based on scaling argument and by Zhou & Xia (2002) based on measurements of the temperature derivative skewness.

Motivated by the concept of Grossmann & Lohse (2004), we have refined those analyses and proposed new definitions of the plume and background dominated thermal dissipation rates. Both are conditioned with respect to the quantity $u_z\theta$, which is always positive for the rising or falling plumes in a convection cell. We have presented detailed scaling laws for ϵ_T as a function of Ra, based on our new definitions as well as the usual bulk and boundary layer contributions. The scaling law $\langle \epsilon_T \rangle \sim Ra^\zeta$ always gives a negative exponent, ζ, in the bulk or plume and background dominated regions. This is in contrast to the classical scaling theory of Grossmann & Lohse (2000) and the refined ansatz of Grossmann & Lohse (2004), but in agreement with He $et\ al.$ (2007) and He & Tong (2009). However, our exponent in the boundary layer differs significantly form those of the experiments. This discrepancy could partly be attributed to the fact that in laboratory measurements time series are taken at several points and there are some limitations in resolving the gradients. There is no significant dependence of $\langle \epsilon_T \rangle$ on the aspect ratio for the values studied here.

Two particular aspects will be beneficial in exploring further in this regard in the

future. First, an extension to higher Rayleigh numbers is desirable. Second, the direct link between the observed statistics and the local structures in the boundary layer and its vicinity is necessary. Some progresses have already been made in this regard (Shishkina & Wagner 2007; Zhou *et al.* 2007).

In the second part, the heat transfer and the corresponding changes in LSC patterns have been studied as a function of Γ and Ra for the parameter ranges $\Gamma = 0.5 - 12$ and $Ra = 10^7 - 10^9$. Our DNS results have revealed a dependence of the Nusselt number on the aspect ratio. The variation in $Nu(\Gamma)$ curve is between 11% and 3% for the accessible Rayleigh numbers and aspect ratios. A minimum of $Nu(\Gamma)$ is found at $\Gamma \approx 2.5$ and $\Gamma \approx 2.25$ for $Ra = 10^7$ and $Ra = 10^8$, respectively. This is the point at which the LSC undergoes a transition from a single-roll to a double-roll pattern. The trend in $Nu(\Gamma)$ curve indicates that the heat transfer becomes independent of geometry for sufficiently large aspect ratios, namely for $\Gamma \gtrsim 8$ at $Ra = 10^7$. Our current data for $Ra \geq 10^8$ suggest that the Nusselt number would be aspect ratio independent for $\Gamma > 8$. The observed trend in $Nu(\Gamma)$ as well as the changes in the LSC patterns have been validated by the POD analysis of Bailon-Cuba, Emran & Schumacher (2009). The reorganization of the LSC from roll shape to pentagon or hexagon-like structures with increasing Rayleigh number as well as with increasing aspect ratio is observed.

We provide arguments, which rationalize the non-monotonic graphs $Nu = f(\Gamma)$. Furthermore, we demonstrate that the power law relation $Nu = A(\Gamma) \times Ra^{\beta(\Gamma)}$ gives the coefficient and exponent ranges as $A(\Gamma) = 0.165 - 0.118$ and $\beta(\Gamma) = 0.287 - 0.305$, respectively, which follow the scaling relations $A(\Gamma) = \Gamma^{-\lambda_1}$ and $\beta(\Gamma) = \Gamma^{\lambda_2}$, with $\lambda_1 = 0.18$ and $\lambda_2 = 0.03$ for the aspect ratio range $\Gamma = 0.5 - 4$ and Rayleigh number range $Ra \sim 10^7 - 10^{10}$. We believe that it is important to include this dependence, albeit weak, in future scaling theories. The variations in β seem to bridge the gap between the well-known exponents $\beta = 2/7$ and $1/3$, which have been measured in the past. Further investigations at higher Rayleigh numbers and larger aspect ratios are necessary to draw a firm conclusion on this matter.

We also observe that the LSC patterns in turbulent convection at $Ra \geq 10^7$ are still strikingly similar to those in the weakly nonlinear regime immediately beyond the onset of convection (Bodenschatz *et al.* 2000). The system does not seem to forget these patterns. Large-scale circulation structures are, therefore, always present similar to high-Reynolds number turbulence in von Kármán swirling flows (La Porta *et al.* 2001) or Taylor vortex flows (Lathrop *et al.* 1992).

It is clear that further numerical explorations in the regime of large aspect ratios and high Rayleigh numbers, which are at least one or two orders of magnitude larger than the values provided here, are necessary. One expects that the aspect-ratio-dependence of the turbulent heat transfer would vanish for sufficiently large Γ. To achieve those goals, the efforts are underway and will shed more light on $A(\Gamma)$ and $\beta(\Gamma)$ as reported in Figure 5.5. Another important aspect, in our view, would be to conduct a closer study of the same issues for fixed flux boundary conditions,

which correspond, for example, to a radiative cooling on top of an atmospheric boundary layer. Recently, the first step in this direction has been undertaken by Verzicco & Sreenivasan (2007) and Johnston & Doering (2009).

In the final part, we have presented DNS studies on the Lagrangian particle dispersion in Rayleigh-Bénard convection. Three cases, namely $\Gamma = 1$ and 3 at $Ra = 10^7$, and $\Gamma = 1$ at $Ra = 10^8$, have been selected for this purpose. We have employed linear interpolation scheme for the velocity field and analytical integration for the time marching. This approach simplifies the computations. Our interpolation schemes reproduced accurately the global heat transfer in the Lagrangian frame Nu_L, with deviations 0.2% and 1.5% compared to those of the Eulerian simulations for $Ra = 10^7$ and 10^8, respectively in the cell with aspect ratio $\Gamma = 1$. In order to achieve the appropriate value of the global Nusselt number, all regions of the convection cell have to be sampled for a sufficiently long time. The oscillations in $Nu_L(t)$ curve imply that the majority of the tracer particles follow the LSC path or they are not uniformly seeded in all parts of the domain at the same time. We also observe that for a large number of tracer particles with a uniform initial seeding in the domain, the convergence of $Nu_L(t)$ is rapid. Conversely, the convergence is slower for a small number of particles with a non-uniform initial seeding.

For the pair dispersion parameter analysis, we detect ballistic ($R^2 \sim t^2$) and Richardson-like ($R^2 \sim t^3$) regimes. Similar trends were observed in recent studies for rectangular domains with free-slip top and bottom plates and periodic sidewalls (Schumacher 2008, 2009). The finite size of the cell suppresses the dispersion limit, hence a Taylor-like regime ($R^2 \sim t$) is absent in our studies as oppose to Schumacher (2008, 2009). However, we expect it to be present at larger aspect ratios ($\Gamma > 3$). The pair dispersion is sensitive with respect to the initial septation. The vertical velocity is strongly anti-correlated to the lateral ones due to stronger fluctuations in the signals of $u_z(t)$ compared to those of $u_x(t)$ and $u_y(t)$. This is in line with the results of Schumacher (2009).

The probability density functions of the acceleration components, a_i, in the Lagrangian frame show that the acceleration is highly intermittent with stretched exponential shapes. The PDFs are almost symmetric and have flatness values that exceed the Gaussian flatness by almost an order of magnitude ($F(a_i) \gg 3$). Our results are qualitatively in agreement with that of La Porta $et\ al.$ (2001), Voth $et\ al.$ (2002) and Schumacher (2008, 2009). The acceleration components are almost isotropic here. It remains to be seen whether this isotropy persists at higher Rayleigh numbers ($Ra > 10^8$) and (or) at higher aspect ratios. Furthermore, the PDFs of the convective heat fluxes revealed super-Gaussian distributions, which are the manifestations of intermittency in the flow field. One expects stretched exponential forms in the higher Rayleigh number regime (Shang $et\ al.$ 2004; Gasteuil $et\ al.$ 2007). From the time increment analysis of vertical velocity, we observe that the PDFs of $\delta_\tau u_z$ are symmetric and have stretched exponential shapes with fatter tails for $\tau \approx \tau_\eta$ and $\tau \approx T_L$. However, they keep their exponential forms

for $\tau \gg T_L$. The PDFs of the temperature increment, $\delta_\tau T$, are non-Gaussian and slightly skewed. The next step would be to compare the PDFs of temperature increments for different Rayleigh numbers.

Bibliography

AHLERS, G., GROSSMANN, S. & LOHSE, D. 2009 Heat transfer and large-scale dynamics in turbulent convection. *Rev. Mod. Phys.* **81(2)**, 503-537.

AMATI, G., KOAL, K., MASSAIOLI, F., SREENIVASAN, K. R. & VERZICCO, R. 2005 Turbulent thermal convection at high Rayleigh numbers for a Boussinesq fluid of constant Prandtl number. *Phys. Fluids* **17**, 121701.

BAILON-CUBA, J., **EMRAN, M. S.** & SCHUMACHER, J. 2009 Aspect ratio dependence of heat transfer and large-scale flow in turbulent convection. *J. Fluid Mech.* (under review).

BEAM, R. M. & WARMING, R. F. 1976 An implicit finite-difference algorithm for hyperbolic systems in conservation law form. *J. Comput. Phys.* **22**, 87.

BELMONTE, A. & LIBCHABER, A. 1996 Thermal signature of plumes in turbulent convection: The skewness of the derivative. *Phys. Rev. E* **53**, 4893-4898.

BÉNARD, H. 1900 Les tourbillons cellulaires dans une nappe liquide, Revue genral des sciences pures et appliquees. *Revue genral des sciences pures et appliquees* **11**, 1261-1271 and 1309-1328.

BODENSCHATZ, E., PESCH, W. & AHLERS G. 2000 Recent developments in Rayleigh-Bénard convection. *Annu. Rev. Fluid Mech.* **32**, 709-778.

BOFFETTA, G. & SOKOLOV, I. M. 2002 Relative dispersion in fully developed turbulence: The Richardson's Law and Intermittency Corrections. *Phys. Rev. Lett.* **88**, 094501.

BOUSSINESQ, J. V. 1903 Théorie analytique de la chaleur: Volume 2. *Gauthier-Villars*, Paris.

BRAUN, W., DE LILLO, F. & ECKHARDT, B. 2006 Geometry of particle paths in turbulent flows. *J. Turbul.* **7**, N62.

BROWN, E. & AHLERS, G. 2006 Rotations and cessations of the large-scale circulation in turbulent Rayleigh-Bénard convection. *J. Fluid Mech.* **568**, 351-386.

BROWN, E. & AHLERS, G. 2007 Temperature gradients, and search for non-Boussinesq effects, in the interior of turbulent Rayleigh-Bénard convection. *Europhys. Lett.* **80**, 14001 (6 pages).

Brown, E., Funfschilling, D. & Ahlers, G. 2007 Anomalous Reynolds-number scaling in turbulent Rayleigh-Bénard convection. *J. Stat. Mech.* P10005.

Brown, E. & Ahlers G. 2008 Azimuthal asymmetries of the large-scale circulation in turbulent Rayleigh-Bénard convection. *Phys. Fluids* **20**, 105105 (15 pages).

Bukai, M., Eidelman, A., Elperin, T., Kleeorin, N., Rogachevskii, I. & Sapir-Katiraie, I. 2009 Effect of large-scale coherent structures on turbulent convection. arXiv:0905.2721v1.

Busse, F. H. & Whitehead, J. A. 1971 Instabilities of convection rolls in a high Prandtl number fluid. *J. Fluid Mech.* **47**, 305-320.

Busse, F. H. 1978 Non-linear properties of thermal convection. *Rep. Prog. Phys.* **41**, 1929-1967.

Busse, F. H. 2003 The sequence-of-bifurcations approach towards understanding turbulent fluid flow. *Surveys Geophys.* **24**, 269-288.

Castaing, B., Gunaratne, G., Heslot, F., Kadanoff, L., Libchaber, A., Thomae, S., Wu, X.-Z., Zaleski, S. & Zanetti, G. 1989 Scaling of hard thermal turbulence in Rayleigh-Bénard convection. *J. Fluid Mech.* **204**, 1-30.

Castaing, B., Gagne, Y. & Hopfinger, E. J. 1990 Velocity probability density functions of high Reynolds number turbulence. *Physica D* **46**, 177-200.

Chandrasekhar, S. 1961 Hydrodynamic and Hydromagnetic Stability. *Dover Publications, Inc.*, New York.

Charlson, G. S. & Sani, R. L. 1970 Thermoconvective instability in a bounded cylindrical fluid layer. *Int. J. Heat Mass Transfer* **13**, 1479-1496.

Charlson, G. S. & Sani, R. L. 1971 On the thermoconvective instability in a bounded cylindrical fluid layer. *Int. J. Heat Mass Transfer* **14**, 2157-2160.

Chen, Y.-Y. 1992 Finite-size effects on linear stability of pure-fluid convection. *Phys. Rev. A* **45**, 3727-3731.

Chertkov, M., Falkovich, G. & Kolokolov, I. 1998 Intermittent dissipation of a passive scalar in turbulence. *Phys. Rev. Lett.* **80**, 2121-2124.

Chevillard, L., Castaing, B., Lévêque & Arneodo, A. 2006 Unified multifractal description of velocity increments statistics in turbulence: Intermittency and skewness. *Physica D* **218**, 77-82.

Ching, E. S. C. 1991 Probabilities for temperature differences in Rayleigh-Bénard convection. *Phys. Rev. A* **44**, 3622-3628.

CHING, E. S. C. 1993 Probability densities of turbulent temperature fluctuations. *Phys. Rev. Lett.* **70**, 283-286.

CHING, E. S. C. & TAM, W. S. 2006 Aspect-ratio dependence of heat transport by turbulent Rayleigh-Bénard convection. *J. Turb.* **7**, 72 (11 pages).

CLEVER, R. M. & BUSSE, F. H. 1989 Three-dimensional knot convection in a layer heated from below. *J. Fluid Mech.* **198**, 345-363.

CROQUETTE, V. 1989 Convective pattern dynamics at low Prandtl number: Part II. *Contemporary Physics* **30**, 153-171.

CROSS, M. 2003 Pattern Formation in Rayleigh-Bénard Convection - Lecture 1. *Benasque PHYSBIO*, `http://www.szfki.hu/~physbio/activities/lectures.htm`.

DIMOTAKIS, P. E. 2005 Turbulent mixing. *Annu. Rev. Fluid Mech.* **37** 329-356.

DONZIS, D. A., SREENIVASAN, K. R. & YEUNG, P. K. 2005 Scalar dissipation rate and dissipative anomaly in isotropic turbulence. *J. Fluid Mech.* **532**, 199-216.

DONZIS, D. A., YEUNG, P. K. & SREENIVASAN, K. R. 2008 Energy dissipation rate and enstrophy in isotropic turbulence: resolution effects and scaling in direct numerical simulations. *Phys. Fluids* **20**, 045108.

DRAZIN, P. G. 2002 Introduction to Hydrodynamic Stability. *Cambridge University Press*.

DU PUITS, R., RESAGK, C. & THESS, A. 2007 Breakdown of wind in turbulent thermal convection. *Phys. Rev. E* **75**, 016302 (4 pages).

EMRAN, M. S. & SCHUMACHER, J. 2008 Fine-scale statistics of temperature and its derivatives in convective turbulence. *J. Fluid Mech.* **611**, 13-34.

EMRAN, M. S., BAILON-CUBA, J. & SCHUMACHER, J. 2009 Turbulent heat transfer and large-scale flow in convection cells with aspect ratio $\Gamma > 1$. *Springer Proceedings in Physics* **132**, 517-520. EUROMECH conference 2009, Marburg.

FERCHICHI, M. & TAVOULARIS, S. 2002 Scalar probability density function and fine structure in uniformly sheared turbulence. *J. Fluid Mech.* **461**, 155-182.

FERZIGER, J. H., PERIĆ, M. 2001 Computational Methods for Fluid Dynamics. *Springer Verlag*, 3rd edition.

FONTENELE ARAUJO, F., GROSSMANN, S. & LOHSE, D. 2005 Wind reversals in turbulent Rayleigh-Bénard convection. *Phys. Rev. Lett.* **95**, 084502 (4 pages).

Funfschilling, D., Brown, E., Nikolaenko, A. & Ahlers, G. 2005 Heat transport by turbulent Rayleigh-Bénard convection in cylindrical samples with aspect ratio one and larger. *J. Fluid Mech.* **536**, 145-154.

Gamba A. & Kolokolov, I. 1999 Dissipation statistics of a passive scalar in a multi-dimensional smooth flow. *J. Stat. Phys.* **94**, 759-777.

Gao, H., Metcalfe, G., Jung, T. & Behringer, R. P. 1987 Heat-flow experiments in liquid ^{4}He with variable cylindrical geometry. *J. Fluid Mech.* **174**, 209-231.

Gasteuil, Y., Shew, W. L., Gibert, M., Chillá, F., Castaing, B. & Pinton, J. F. 2007 Lagrangian Temperature, Velocity, and Local Heat Flux Measurement in Rayleigh-Bénard Convection. *Phys. Rev. Lett.* **99**, 234302(4 pages).

Gollub, J. P., Clarke, J., Gharib, M., Lane, B. & Mesquita, O. N. 1991 Fluctuations and transport in a stirred fluid with a mean gradient. *Phys. Rev. Lett.* **67**, 3507-3510.

Grossmann, S. & Lohse, D. 2000 Scaling in thermal convection: a unifying theory. *J. Fluid Mech.* **407**, 27-56.

Grossmann, S. & Lohse, D. 2002 Prandtl and Rayleigh number dependences of the Reynolds number in turbulent thermal convection. *Phys. Rev. E* **66**, 016305.

Grossmann, S. & Lohse, D. 2003 On geometry effects in Rayleigh-Bénard convection. *J. Fluid Mech.* **486**, 105-114.

Grossmann, S. & Lohse, D. 2004 Fluctuations in turbulent Rayleigh-Bénard convection: The role of plumes. *Phys. Fluids* **16**, 4462.

Grötzbach, G. 1983 Spatial resolution requirements for direct numerical simulation of the Rayleigh-Bénard convection. *J. Comput. Phys.* **49**, 241-269.

Gylfason, A. & Warhaft, Z. 2004 On higher order passive scalar structure functions in grid turbulence. *Phys. Fluids* **16**, 4012-4019.

Harlow, F. H. & Welch, J. E.1965 Numerical calculation of time-Dependent viscous incompressible flow of fluid with free surface. *Phys. Fluids* **8**, 2182-2189.

Hartlep, T., Tilgner, A. & Busse, F. H. 2003 Large scale stuctures in Rayleigh-Bénard convection at high Rayleigh numbers. *Phys. Rev. Lett.* **91**, 064501 (4 pages).

Hartlep, T., Tilgner, A. & Busse, F. H. 2005 Transition to turbulent convection in a fluid layer heated from below at moderate aspect ratio. *J. Fluid Mech.* **544**, 309-322.

He, X., Tong, P. & Xia, K.-Q. 2007 Measured thermal dissipation field in turbulent Rayleigh-Bénard convection. *Phys. Rev. Lett.* **98**, 144501 (4 pages).

He, X. & Tong, P. 2009 Measurement of the thermal dissipation field in turbulent Rayleigh-Bénard convection. *Phys. Rev. E* **79**, 026306.

Heslot, F., Castaing, B. & Libchaber, A. 1987 Transitions to turbulence in helium gas. *Phys. Rev. A* **36**, 5870-5873.

Jayesh & Warhaft, Z. 1991 Probability distribution of a passive scalar in grid-generated turbulence. *Phys. Rev. Lett.* **67**, 3503-3506.

Jayesh & Warhaft, Z. 1992 Probability distribution, conditional dissipation and transport of passive temperature fluctuations in grid-generated turbulence. *Phys. Fluids A* **4**, 2292-2307.

Johnston, H. & Doering, C. R. 2009 A comparison of turbulent thermal convection between conditions of constant temperature and constant flux. *Phys. Rev. Lett.* **102** 064501 (4 pages).

Kaczorowski, M. & Wagner, C. 2007 Direct numerical simulation of turbulent convection in a rectangular Rayleigh-Bénard cell. *Proceedings of Fifth International Symposium on Turbulence and Shear Flow Phenomena*, Garching, 2007, Vol.2, 499-504.

Kaczorowski, M. & Wagner, C 2009 Analysis of the thermal plumes in turbulent Rayleigh-Bénard convection based on well-resolved numerical simulations. *J. Fluid Mech.* **618**, 89-112.

Kadanoff, L. P. 2001 Turbulent heat flow: Structures and scaling. *Phys. Today* **54**, 34-99.

Kaneda, Y., Ishihara, T., Yokokawa, M., Itakura, K. & Uno, A. 2003 Energy dissipation rate and energy spectrum in high resolution direct numerical simulations of turbulence in a periodic box. *Phys. Fluids* **15**, L21.

Kerr, R. M. 1996 Rayleigh number scaling in numerical convection. *J. Fluid Mech.* **310**, 139-179.

Kim, J. & Moin, P. 1985 Application of a fractional-step method to incompressible Navier-Stokes equations. *J. Comput. Phys.* **59**, 308-323.

Koschmieder, E. L. 1969 On the wavelength of convective motions. *J. Fluid Mech.* **35**, 527-530.

Koschmieder, E. L. 1993 Bénard Cells and Taylor Vortices. *Cambridge University Press*, New York.

KRAICHNAN, R. H. 1962 Turbulent Thermal Convection at Arbitrary Prandtl Number. *Phys. Fluids* **5**, 1374.

KRISHNAMURTI, R. 1970 On the transition to turbulent convection. Part 2. The transition to time-dependent flow. *J. Fluid Mech.* **42**, 309-320.

KRISHNAMURTI, R. AND HOWARD, L. N. 1981 Large-scale flow generation in turbulent convection. *Proc. Natl. Acad. Sci.* **78**, 1981-1985.

KUSHNIR, D., SCHUMACHER, J. & BRANDT, A. 2006 Geometry of intensive scalar dissipation events in turbulence. *Phys. Rev. Lett.* **97**, 124502.

LA PORTA, A., VOTH, G. A., CRAWFORD, A. M., ALEXANDER, J. & BODENSCHATZ, E. 2001 Fluid particle accelerations in fully developed turbulence. *Nature* **409**, 1017.

LATHROP, D. P., FINEBERG, J. & SWINNEY, H. L. 1992 Turbulent flow between concentric rotating cylinders at large Reynolds numbers. *Phys. Rev. Lett.* **68**, 1515-1518.

LOBUTOVA, E., RESAGK, C., RANK, R. & MÜLLER, D. 2009 Extended three dimensional particle tracking velocimetry for large enclosures. *Springer-Verlag Berlin Heidelberg*, ISBN 978-3-642-01105-4.

LUMLEY, J. L. 1967 Similarity and the turbulent energy spectrum. *Phys. Fluids* **10**, 855-858.

MALKUS, W. V. R. & VERONIS, G. 1958 Finite amplitude cellular convection. *J. Fluid Mech.* **4**, 225-260.

MORDANT, N., DELOUR, J., LÉVEQUE, E., ARNÉODO, A. & PINTON, J.-F. (2002) Long time correlations in Lagrangian dynamics: A key to intermittency in turbulence. *Phys. Rev. Lett.* **89**, 254502 (4 pages).

MYDLARSKI, L. & WARHAFT, Z. 1998 Passive scalar statistics in high-Péclet-number grid turbulence. *J. Fluid Mech.* **358**, 135-175.

NIEMELA, J. J., SKRBEK, L., SREENIVASAN, K. R. & DONELLY, R. J. 2000 Turbulent convection at very high Rayleigh numbers. *Nature* **404**, 837-840.

NIEMELA, J. J. & SREENIVASAN, K. R. 2003 Turbulent confined convection. *J. Fluid Mech.* **481**, 355-384.

NIEMELA, J. J. & SREENIVASAN, K. R. 2006 Turbulent convection at high Rayleigh numbers and aspect ratio 4. *J. Fluid Mech.* **557**, 411-422.

ORESTA, P., STRINGANO, G. & VERZICCO, R. 2007 Transitional regimes and rotation effects in Rayleigh-Bénard convection in a slender cylindrical cell. *Eur. J. Mech. B/Fluids* **26**, 1-14.

OH, K.-J. & KANG, S.-H. 1992 Full scale Reynolds number effects for the viscous flow around the ship stern. *Computational Mechanics* **9**, 85-94.

ORSZAG, S. A. 1971 Numerical simulation of incompressible flows within simple boundaries. I: Galerkin (spectral) representations. *Stud. Appl. Math.* **50**, 293-327.

OVERHOLT, M. R. & POPE, S. B. 1996 Direct numerical simulation of a passive scalar with imposed mean gradient in isotropic turbulence. *Phys. Fluids* **8**, 3128-3148.

POPE, S. B. 2000 *Turbulent flows.* Cambridge University Press.

PROCACCIA, I., CHING, E. S. C., CONSTANTIN, P., KADANOFF, L. P., LIBCH-ABER, A., & WU, X.-Z. 1991 Transitions in convective turbulence: The role of thermal plumes. *Phys. Rev. A* **44**, 8091 - 8102.

PUMIR, A., SHRAIMAN, B. & SIGGIA, E. D. 1991 Exponential tails and random advection. *Phys. Rev. Lett.* **23**, 2984-2987.

PUMIR, A. 1996 Turbulence in homogeneous shear flows. *Phys. Fluids* **8**, 3112-3127.

RAYLEIGH, L. 1916 On convection currents in a horizontal layer of fluid when the higher temperature is on the under side. *Philos. Mag.* **32**, 529.

SCHÖNFELD, W. 1995 Numerical simulation of the dispersion of artificial radionu-clides in the english channel and the North Sea. *Journal of Marine Systems* **6**, 529-544.

SCHLÜTER, A., LORTZ, D. & BUSSE, F. 1965 On the stability of steady finite amplitude convection. *J. Fluid Mech.* **23**, 129-144.

SCHUMACHER, J. & SREENIVASAN, K. R. 2003 Geometric features of the mixing of passive scalars at high Schmidt numbers. *Phys. Rev. Lett.* **91**, 174501 (4 pages).

SCHUMACHER, J., SREENIVASAN, K. R. & YEUNG, P. K. 2005 Very fine struc-tures in scalar mixing. *J. Fluid Mech.* **531**, 113-122.

SCHUMACHER, J. & SREENIVASAN, K. R. 2005 Statistics and geometry of passive scalars in turbulence. *Phys. Fluids* **17**, 125107 (9 pages).

SCHUMACHER, J. 2008 Lagrangian dispersion and heat transport in convective turbulence. *Phys. Rev. Lett.* **100**, 134502 (4 pages).

SCHUMACHER, J., **EMRAN, M. S.** & ECKHARDT, B. 2008 The fine-scale struc-ture of turbulence. *NIC Series* **39**, 341-348. NIC Symposium 2008, Jülich.

SCHUMACHER, J. 2009 Lagrangian studies in convective turbulence. *Phys. Rev. E* **79**, 056301 (13 pages).

SCHUMACHER, J. & **EMRAN, M. S.** 2009 Lagrangian analysis of turbulent convection. *Springer Proceedings in Physics* **132**, 43-46. EUROMECH conference 2009, Marburg.

SCHWARZTRAUBER, P. N. 1974 A direct method for the discrete solution of separable elliptic equations. *SIAM J. Numerical Analysis* **11**, 1136-1150.

SHANG, X.-D., QIU, X.-L., TONG, P., & XIA, K.-Q. 2004 Measurements of the local convective heat flux in turbulent Rayleigh-Bénard convection. *Phys. Rev. E* **70**, 026308.

SHISHKINA, O. & WAGNER C. 2006 Analysis of thermal dissipation rates in turbulent Rayleigh-Bénard convection. *J. Fluid Mech.* **546**, 51-60.

SHISHKINA, O. & WAGNER C. 2007 Local heat flux in turbulent Rayleigh-Bénard convection. *Phys. Fluids* **19**, 085107 (13 pages).

SHISHKINA, O. & WAGNER C. 2008 Analysis of sheet-like thermal plumes in turbulent Rayleigh-Bénard convection. *J. Fluid Mech.* **599**, 383.

SHRAIMAN, B. I. & SIGGIA E. D. 1990 Heat transport in high-Rayleigh-number convection. *Phys. Rev. A* **42**, 3650 - 3653.

SHRAIMAN, B. I. & SIGGIA E. D. 2000 Scalar turbulence. *Nature* **405**, 639-646.

SIGGIA E. D. 1994 High Rayleigh number convection. *Annu. Rev. Fluid Mech.* **26**, 137-68.

STEIN, R. F. & NORDLUND, A 2006 Solar small-scale magnetoconvection. *Astrophys. J.* **642**, 1246-1255.

STEVENS, R. J. A. M., VERZICCO, R. & LOHSE, D 2009 Radial boundary layer structure and Nusselt number in Rayleigh-Bénard convection. *J. Fluid Mech.*, (in press).

SUN, C., REN, L.-Y., SONG, H. & XIA, K.-Q. 2005 Heat transport by turbulent Rayleigh-Bénard convection in 1 m diameter cylindrical cells of widely varying aspect ratio. *J. Fluid Mech.* **542**, 165-174.

VAN REEUWIJK, M., JONKER, H. J. J. & HANJALIĆ, K. 2008 Wind and boundary layers in Rayleigh-Bénard convection. I. Analysis and modeling. *Phys. Rev. E* **77**, 036311 (15 pages).

VERZICCO, R. & ORLANDI, P. 1996 A finite-difference scheme for three-dimensional incompressible flows in cylindrical coordinates. *J. Comp. Phys.* **123**, 402-414.

VERZICCO, R. & CAMUSSI, R. 1997 Transitional regimes of low-Prandtl thermal convection in a cylindrical cell. *Phys. Fluids* **9**, 1287-1295.

VERZICCO, R. & CAMUSSI, R. 2003 Numerical experiments on strongly turbulent thermal convection in a slender cylindrical cell. *J. Fluid Mech.* **477**, 19-49.

VERZICCO, R. & SREENIVASAN, K. R. 2007 A comparison of turbulent thermal convection between conditions of constant temperature and constant heat flux. *J. Fluid Mech.* **595**, 203-219.

VON HARDENBERG, J., PARODI, A., PASSONI, G., PROVENZALE, A. & SPIEGEL, E. A. 2008 Large-scale patterns in Rayleigh-Bénard convection. *Phys. Lett. A* **372**, 2223-2229.

VOTH, G. A., LA PORTA, A., CRAWFORD, A. M., ALEXANDER, J. & BODENSCHATZ, E. 2002 Measurement of particle accelerations in fully developed turbulence. *J. Fluid Mech.* **469**, 121-160.

WARHAFT, Z. 2000 Passive scalars in turbulent flows. *Annu. Rev. Fluid Mech.* **32**, 203-240.

WARHAFT, Z. 2002 Turbulence in nature and laboratory. *Proc. Nat. Acad. Sci.* **99**, 2481-2486.

WATANABE, T. & GOTOH, T. 2004 Statistics of a passive scalar in homogeneous turbulence. *New J. Phys.* **6**, 40 (36 pages).

WOLK, F. 2003 Three-dimensional Lagrangian Tracer Modelling in Wadden Sea Areas. *Carl von Ossietzky University Oldenburg*, Diploma thesis.

WU, X.-Z. & LIBCHABER, A. 1992 Scaling relation in thermal turbulence: The aspect-ratio dependence. *Phys. Rev. A* **45**, 842-845.

XI, H.-D., LAM, S. & XIA, K.-Q. 2004 From laminar plumes to organized flows: the onset of large-scale circulation in turbulent thermal convection. *J. Fluid Mech.* **503**, 47-56.

XI, H.-D. & XIA, K.-Q. 2008 Azimuthal motion, reorientation, cessation, and reversal of the large-scale circulation in turbulent thermal convection: A comparative study in aspect ratio one and one-half geometries. *Phys. Rev. E* **78**, 036326 (11 pages).

YAKHOT, V. 1989 Probability distributions in high-Rayleigh-number Bénard convection. *Phys. Rev. Lett.* **63** 1965-1967.

YEUNG, P.K. & POPE, S.B. 1989 Lagrangian statistics from direct numerical simulations of isotropic turbulence. *J. Fluid Mech.* **207**, 531-586.

YEUNG, P. K., DONZIS, D. A. & SREENIVASAN, K. R. 2005 High-Reynolds-number simulation of turbulent mixing. *Phys. Fluids* **17** 081703 (4 pages).

ZERIHUN DESTA, T., VAN BRECHT, A., QUANTEN, S., VAN BUGGENHOUT, S., MEYERS, J., BAELMANS, M. & BERCKMANS, D. 2005 Modelling and control of heat transfer phenomena inside a ventilated air space. *Energy and Buildings* **37**, 777-786.

ZHOU S.-Q. & XIA, K.-Q. 2002 Plume statistics in thermal turbulence: Mixing of an active scalar. *Phys. Rev. Lett.* **89**, 184502 (4 pages).

ZHOU Q., SUN, C. & XIA, K.-Q. 2007 Morphological evolution of thermal plumes in turbulent Rayleigh-Bénard convection. *Phys. Rev. Lett.* **98**, 074501 (4 pages).